

Imaging Beam-Sensitive Materials by Electron Microscopy

Qiaoli Chen, Christian Dwyer, Guan Sheng, Chongzhi Zhu, Xiaonian Li, Changlin Zheng,* and Yihan Zhu*

Electron microscopy allows the extraction of multidimensional spatiotemporally correlated structural information of diverse materials down to atomic resolution, which is essential for figuring out their structure–property relationships. Unfortunately, the high-energy electrons that carry this important information can cause damage by modulating the structures of the materials. This has become a significant problem concerning the recent boost in materials science applications of a wide range of beam-sensitive materials, including metal–organic frameworks, covalent–organic frameworks, organic–inorganic hybrid materials, 2D materials, and zeolites. To this end, developing electron microscopy techniques that minimize the electron beam damage for the extraction of intrinsic structural information turns out to be a compelling but challenging need. This article provides a comprehensive review on the revolutionary strategies toward the electron microscopic imaging of beam-sensitive materials and associated materials science discoveries, based on the principles of electron–matter interaction and mechanisms of electron beam damage. Finally, perspectives and future trends in this field are put forward.

materials science and associated research fields. A major challenge in these fields lies in the direct observation of the intrinsic and dynamic properties of diverse materials in multidimensions and at the atomic scale, including their structures, chemical compositions, electronic states, and spins. Accordingly, the roadmap of TEM technological and methodological innovations has involved great efforts devoted to the pursuit of higher spatial resolution, more correlated structural information and less electron beam damage. In the aspect of pushing the spatial resolution limits of electron microscopy, advanced aberration correction techniques^[1] or ptychographic diffractive imaging methods^[2] nowadays allow the imaging of nanoscale objects down to atomic- or even deep sub-Ångström resolution. In addition, modern TEM instruments unite various spectroscopic and in situ (operando) techniques and provide multidimensional correlated

1. Introduction

Developments in transmission electron microscopy (TEM) are largely motivated by the quest for essential information in

structural, chemical and electronic information spanning the spatial,^[3] time,^[4–8] energy,^[9] and momentum dimensions.^[10] Such high-resolution and correlated information is important in providing a solid basis for the determination of structure–property relationships in materials. Notwithstanding this, electrons interact very strongly with materials, which might inevitably introduce temporary or permanent structural changes, typically through atomic displacements or electronic excitations. Thus, the development of TEM techniques and methods for imaging materials that are highly vulnerable to electron beam irradiation becomes crucial. In fact, while successful applications of low-dose cryogenic-TEM techniques^[11–14] and single-particle tomography (SPT) methods^[15,16] have boosted developments in structural biology in the past decades,^[17] knowledge of electron beam damage in a wider range of materials science specimens remains fragmentary by comparison, and corresponding TEM imaging technologies and methodologies are much less explored until recently.


Actually, many aspects of the latest advances in materials science research are exactly pioneered by the synthesis and application of materials which happen to be beam-sensitive. Such materials include i) inorganic materials containing light metals,^[18,19] zeolites,^[20–24] and low-dimensional materials (e.g., graphene, carbon nanotubes, and molybdenum disulfide);^[25–27] ii) organic materials like covalent–organic frameworks (COFs),^[28,29] macromolecules,^[30–32] and polymers;^[33] and iii) organic–inorganic hybrid materials like metal–organic

Prof. Q. Chen, C. Zhu, Prof. X. Li, Prof. Y. Zhu
Center for Electron Microscopy
State Key Laboratory Breeding Base of Green Chemistry Synthesis
Technology and College of Chemical Engineering
Zhejiang University of Technology
Hangzhou 310014, China
E-mail: yihanzhu@zjut.edu.cn

Prof. C. Dwyer
Department of Physics
Arizona State University
Tempe, AZ 85287-1504, USA

G. Sheng
Advanced Membranes and Porous Materials Center
Physical Science and Engineering
King Abdullah University of Science and Technology
Thuwal 23955-6900, Kingdom of Saudi Arabia

Prof. C. Zheng
State Key Laboratory of Surface Physics and Department of Physics
Fudan University
Shanghai 200438, China
E-mail: zcl@fudan.edu.cn

 The ORCID identification number(s) for the author(s) of this article can be found under <https://doi.org/10.1002/adma.201907619>.

DOI: 10.1002/adma.201907619

frameworks (MOFs)^[34–36] and organic–inorganic hybrid perovskites.^[34,37] These materials have intriguing physicochemical properties and promising applications,^[38–44] and direct imaging in the TEM provides a powerful tool to correlate, not only bulk structure, but also local structure with their properties at the atomic scale. This is, however, constrained by the fact that their structures degrade rapidly during TEM imaging upon the exposure to electrons above a certain kinetic energy, dose rate or accumulated dose.^[24,45] For example, MOFs comprise a large family of porous crystalline materials featuring highly designable and flexible pore architectures, framework topologies and structural functionalities, and they hold great promise for a wide range of applications, such as gas separation and storage, sensing, and catalysis.^[46–48] However, an unambiguous structure determination of MOFs through TEM imaging is unfortunately very challenging because most MOFs typically collapse after exposure to only a few electrons \AA^{-2} .^[34,35,49] As another example, graphene, well known for its 2D structure, unprecedented mechanical strength and high charge carrier mobility, is susceptible to degradation for electron beam energies exceeding 80 keV.^[45] As yet another example, a major barrier to the next-generation lithium-ion batteries (LIB) involves the growth of dendrites on the anodes (e.g., lithium-metal anode), which also falls beyond the capability of conventional TEM characterization due to the high electron vulnerability of lithium and its related phases.^[50] Such examples highlight the severe restrictions that must be imposed on TEM imaging of beam-sensitive materials. These restrictions largely limit the accessible image resolution and signal-to-noise ratio (SNR) for the reasonable identification and interpretation of the intrinsic materials structures. To this end, the development of revolutionary TEM technologies and methodologies for imaging irradiation-vulnerable materials is at the cutting edge of many emerging fields in materials science, and will dramatically accelerate the pace of groundbreaking discoveries in these fields.

In this review, we systematically summarize the recently developed strategies to overcome electron beam damage in TEM imaging, including both instrumental and methodological innovations, with an emphasis on the basic principles of electron–matter interactions and mechanisms of electron beam damage. Applications of these strategies and associated fundamental discoveries in materials science are presented. Finally, a short discussion on the perspectives and future trends is given.

2. Physical Origin and Behavior of Electron Beam Damage

2.1. Basic Principles of Electron–Matter Interaction

As probing particles, electrons interact much more strongly with condensed matter compared to X-ray photons and neutrons. Owing to Coulomb interactions, the cross-section for electrons to scatter from atoms is typically about 10^5 times greater than for X-ray photons,^[51] which means electrons can be routinely used to probe nanoscale objects and even single atoms. Moreover, as charged particles, electrons can be easily focused by magnetic or electrostatic lenses, which enables diverse optical modalities, like scanning transmission electron microscopy (STEM), TEM



Qiaoli Chen is an associate professor in the College of Chemical Engineering at Zhejiang University of Technology (China). She received her Ph.D. degree in physical chemistry from Xiamen University (China) in 2018 and was a visiting scholar at Emory University during 2016–2017. Her research interests include

chemical synthesis and structural elucidation of nanostructured materials using combined electron microscopy and diffraction techniques.



Changlin Zheng is a professor in the Department of Physics at Fudan University (China). He received his Ph.D. degree in physics from the Humboldt University of Berlin (Germany) in 2009 and worked as a research fellow at Monash Centre for Electron Microscopy, Monash University (Australia) from 2010–2017. His research

interests focus on the development of advanced electron microscopy techniques (diffraction, imaging, and spectroscopy) and their applications in condensed matter physics and materials science.



Yihan Zhu works as a professor in the Center for Electron Microscopy and the College of Chemical Engineering at Zhejiang University of Technology (China). He received his Ph.D. degree in chemistry at Zhejiang University (China) in 2010. During 2010–2017, he worked as a postdoctoral fellow and research scientist

at King Abdullah University of Science and Technology. His research interests now focus on low-dose electron microscopy and structural elucidation of beam-sensitive materials for applications such as catalysis, gas separation, and energy conversion/storage.

and diffraction, all in a single instrument, simply by cooperatively changing the strength of appropriate lenses.

In a TEM, electrons are emitted from an electron source via either thermal or field emission, and then accelerated to multi-kilovolts before reaching the thin specimen. The majority

of electrons penetrate the specimen and are scattered forward through relatively small angles.^[52] The scattered electrons carry structural and chemical information about the specimen, which is based on the modulation of the amplitude, phase, momentum and energy of the incident electrons. The electron scattering can be classified into two broad categories, elastic scattering and inelastic scattering, according to whether or not the energetic state of the specimen is maintained.^[52] The amount of energy imparted to the specimen critically depends on the electron dose or dose rate, which are defined as the number of incident electrons per unit area of the specimen and the number of incident electrons per unit area per unit time, respectively.

Elastic scattering mainly arises from the Coulomb interaction between the incident electrons and the screened nuclei of atoms in the specimen.^[53,54] Elastic scattering alters the trajectory (momentum) of incoming electrons while maintaining their kinetic energy. Additionally, considering the wave nature of electrons, the scattering can be classified as coherent or incoherent, depending on whether or not the scattered electrons maintain a constant phase relation to the incident electrons. Electrons that interact with the nuclei are elastically scattered, and those collected at higher angles tend to be incoherent due to the combined effects from the modulation by the uncorrelated thermal vibrations of crystal lattice (thermal diffuse

scattering, TDS) and the potential detector filtering effects of localized 1s-type Bloch states.^[55] The fraction of high-angle scattered electrons approach “Rutherford scattering” and gives rise to “Z-contrast” imaging.^[52,55] In general, the elastic scattering cross-section increases with atomic number Z , and it decreases with increasing beam energy.^[51,56]

Inelastic scattering changes both the trajectory and kinetic energy of the incident electrons, which usually results in the excitation of phonons, excitation of conduction or valence electrons or ionization of inner atomic shells of the specimen.^[54,57] Inelastic scattering includes many distinct physical events that arise from direct ionization, individual electronic excitations and collective plasmon/phonon excitations, which give rise to secondary/Auger electrons, X-rays, cathodoluminescence, and heat.^[52–54,57,58] Besides, the energy imparted by the initial interaction is often much higher than the work function of the material, causing immediate ejection of the electron and leaving behind free radicals, broken bonds, etc.^[52]

2.2. Mechanisms of Electron Beam Damage

From a mechanism perspective, as summarized in **Figure 1**, the electron beam damage usually includes knock-on damage,

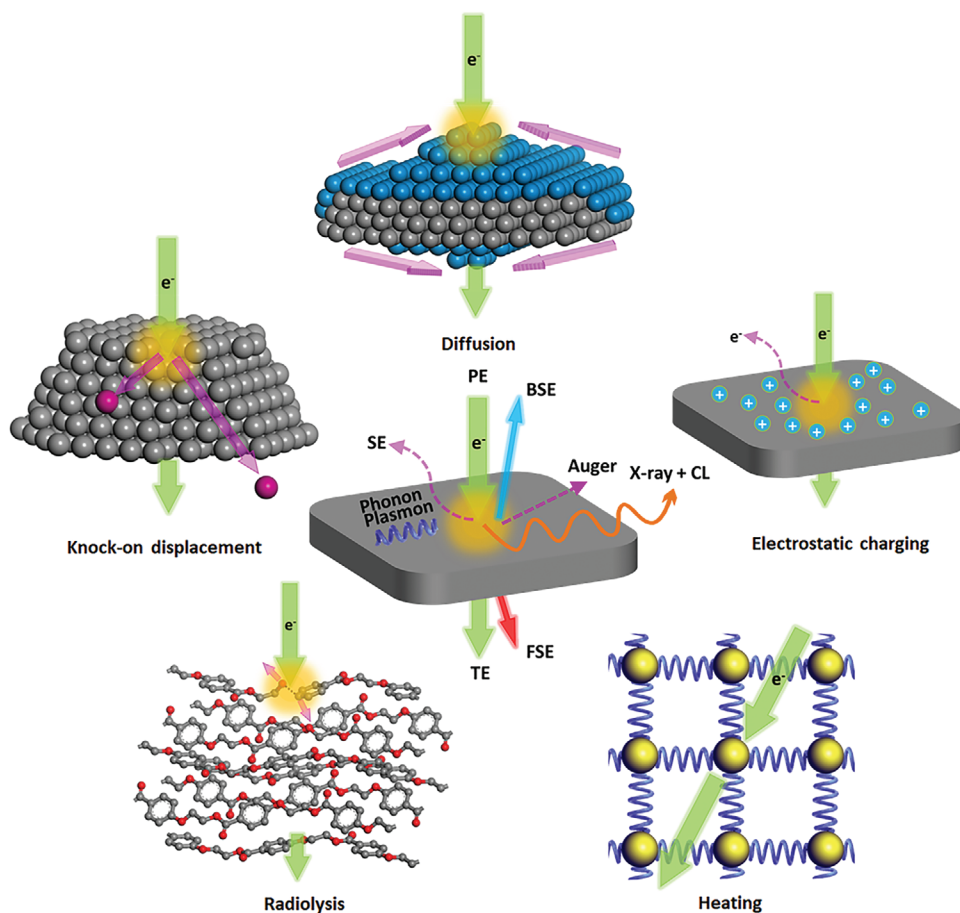


Figure 1. Schematic illustration of the interaction between a high-energy electron beam and a thin specimen and associated mechanisms of electron beam damage. PE, SE, TE, FSE, BSE, and CL refer to primary, secondary, transmitted, forward scattered, back scattered electrons and cathodoluminescence respectively.

radiolysis, charging, heating. An important symptom of electron beam damage is atomic displacements.^[59] Individual atomic displacements may give rise to defects (e.g., Frenkel pairs) in the bulk, while they result in atomic sputtering on the surface.^[59] Cooperative atomic displacements, on the other hand, can induce amorphization,^[60] phase transformation,^[61] and diffusion and segregation.^[62]

A direct interaction between an electron and a nucleus generally introduces knock-on atomic displacements and surface sputtering, which can occur for beam energies beyond a certain threshold energy.^[56] The knock-on damage depends on the threshold energy for the displacement of a particular atom, which is determined by the displacement energy (displacement energy is termed as “ E_d ” or “ E_s ” for the surface binding energy) and the atomic weight (A) of specific atoms. The threshold energy could be as low as 100 keV, especially for surface displacement as E_s is usually much smaller than E_d . If the incident electron energy is below the threshold energy for the displacement of a particular atom, the knock-on damage can be completely eased. Notably, this is true for pure and infinitely large materials. In reality, however, such thresholds may not exist because of the finite sample sizes and the existence of defects, where binding energies are significantly lowered. The electron beam damage for the inorganic materials could be quite substantial in the form of knock-on damage. However, the knock-on damage is not the main damage for insulators. Inelastic electron–electron or electron–phonon scattering can cause radiolysis (ionization), heating, electrostatic charging, and diffusion (contamination) and segregation.^[59] Among them, radiolysis is often considerable and it originates from long-lived electronic excitations (e.g., >1 ps, for insulators^[56]) that drive atomic displacements^[63] through energy–momentum transfer assisted by either thermal vibrations^[64] or Coulomb interactions.^[65] Radiolysis damage also has a cross-section that is closely related with the energy–momentum conversion efficiency from inelastic scattering.^[56,57] For energy–momentum conversion assisted by thermal vibration, Arrhenius law will hold for the atomic jump rate. As a result, radiolysis is often temperature dependent.^[56,59,66,67]

From a materials perspective, depending on their different structures and damage mechanisms, a considerable fraction of beam-sensitive materials belong to either of the two types: dose-sensitive or dose-rate sensitive.^[68] The former type of materials is sensitive to the accumulated electron dose and there is an associated threshold value (i.e., critical dose) before structural degradation becomes considerable.^[59] The overall dose normalized damage effect does not rely on the dose-rate, i.e., the “dose-rate effect,”^[69] defined as dose-rate dependent damage produced per unit dose,^[57] appears to be linear. Regarding the underlying beam damage mechanisms, both knock-on displacement and radiolysis are dose dependent.^[56] A large number of organic, inorganic and organic–inorganic hybrid materials are dose-sensitive, such as most molecular crystals,^[70] polymers,^[71] zeolites,^[72] COFs,^[73] and MOFs.^[34,74] In these cases, the rate of beam damage likely overwhelms any structural recovery that occurs. Materials of the latter type usually include some ionic materials,^[75–78] such as transition metal oxides (TMOs)^[75] and fluorides,^[76,77] of which the beam damage effects are strongly dependent on the dose rate. For materials with increased

radiation sensitivity upon elevated dose rate, a “direct” dose-rate effect is attributed, which in some cases arises from the poor electrical conductivity and accumulated charging.^[57] Damages may be largely eased under a critical value of the dose rate (i.e., dose-rate threshold). On the contrary, an “inverse” dose-rate effect refers to decreased radiation sensitivity upon increased dose rate, which mainly originates from slower beam damage events such as diffusion-limited mass loss, precipitation and segregation.^[57] The underlying dose-rate dependent damage mechanisms, such as heating, charging (or damage that fits the “damage by the induced electric field, DIEF” model^[56]) and diffusion allow the recovery of structures against beam damage,^[75,79] possibly through heat and charge dissipations,^[56] as well as back-diffusion processes.^[69,80,81] Notably, under certain circumstances, the beam damages are affected by multiple mechanisms while the dominant mechanism as well as the overall dose-rate effect may vary depending on the illumination conditions and material properties.^[21,56] As an example, the radiolysis, charging or DIEF mechanism strongly depends on the electric conductivity of the materials, which would however change significantly upon beam irradiation. For silicates, the beam-induced amorphization increases the band gap and thus decreases the conductivity.^[56,82] While the beam-induced oxygen desorption in TMOs, such as TiO_2 ,^[83,84] V_2O_5 ,^[83–85] Nb_2O_5 ,^[83,84] CuO ,^[86] MnO_2 ,^[87] WO_3 ,^[84,88,89] and MoO_3 ,^[90] leads to the surface reduction through either Knotek and Feibelman mechanism^[65,91] or direct sublimation of O_2 , which usually increases the conductivity.

2.3. Measurement of Electron Beam Damage

A TEM tool that is capable of quantitatively measuring the degree of structural change of materials provides a solid basis to experimentally determine the behavior and mechanisms of beam damage. Depending on the type of structural change, there are generally three strategies for the quantitative measurement of beam damage: i) measure the evolution of structural order,^[92] ii) measure the chemical composition variation,^[93] and iii) measure the changes in local and collective structural features.^[74]

The first strategy only applies for crystalline materials and actually measures the gradual loss of crystallinity upon electron beam irradiation, which is very sensitive to atomic displacements and associated structural degradation/amorphization.^[94] In this case, electron diffraction is most frequently used as the probing tool because it is very dose efficient and sensitive to even minor changes in structural order.^[95] Electron diffraction can be carried out under extremely low electron dose rates, say 10^{-3} to 10^{-1} e \AA^{-2} s $^{-1}$, and high-quality time- or dose-series diffraction patterns are acquired at relatively short exposures and small cumulative doses (0.1–0.5 e \AA^{-2}).^[94,96] This allows a sensitive monitoring of tiny structural evolutions arising from the electron beam irradiation through the fading of diffraction spots.^[94] The fading dynamics should be quantitative on thin specimens where kinematical diffraction dominates. Another advantage of electron diffraction as a tool for measuring beam damage over imaging lies in the fact that it is less affected by beam-induced sample motion.^[97,98] Such

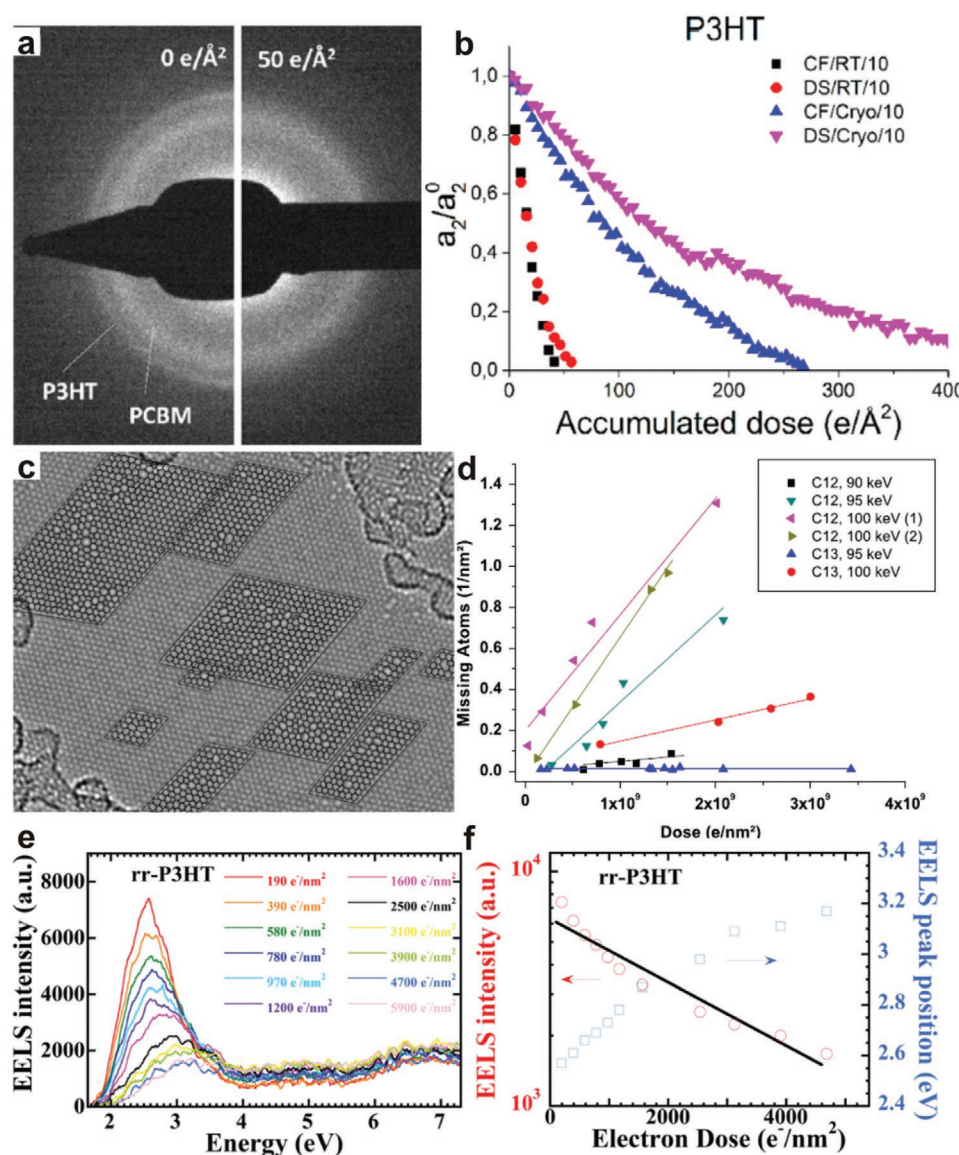


Figure 2. Measurement of electron beam damage. a) Electron diffraction patterns of a P3HT:PCBM bulk heterojunction before and after electron irradiation. b) Fading of relative diffraction intensity versus the accumulated dose for P3HT prepared by conventional method (CF), at room temperature (RT), direct spin-coating (DS) and at 80 K (Cryo) at a dose rate of $10 \text{ e } \text{\AA}^{-2} \text{ s}^{-1}$, respectively. Reproduced with permission.^[79] Copyright 2017, American Chemical Society. c) TEM image of single layer graphene. d) Number of displaced atoms versus dose and electron energy. For the 100 keV case, sample 2 has a ca. three-time higher dose rate than sample 1. Reproduced with permission.^[45] Copyright 2012, American Physical Society. e) EELS of poly(3-hexylthiophene-2,5-diyl) (rr-P3HT) at various electron doses. f) Integrated EELS intensities in low energy-loss regions as a function of electron doses. Reproduced with permission.^[99] Copyright 2015, Wiley-VCH.

motion would however blur the real-space images and interfere with structural damage information. In addition, the fading of different diffraction spots refers to varying degrees of structural order, and those diffraction spots at higher spatial frequencies generally fade first because they are more sensitive to structural order.^[57] A representative example is shown in **Figure 2a**, the fading dynamics of electron diffraction rings of the poly(3-hexylthiophene) (P3HT) and phenyl-C61-butyric acid methyl ester (PCBM) bulk heterojunction can be monitored, which allow the unambiguous determination of their respective critical doses under different synthetic and imaging conditions (**Figure 2b**).

The second strategy allows the direct quantitative measurement of mass loss arising from the surface sputtering and other beam damage mechanisms (e.g., ion emission or hole drilling). Because various chemical species exhibit quite different mass loss rate,^[99] the overall chemical composition may change upon beam irradiation. Energy-dispersive X-ray spectroscopy (EDS) and electron energy loss spectroscopy (EELS) core-loss spectroscopy provide ideal tools for (semi)quantitative measurement of element-specific mass loss associated with various beam damage behaviors.^[99–101] EDS generally has an accepted accuracy of around 5% relative error for major elements,^[101] while the relative accuracy of EELS quantification strongly

depends on many factors such as thickness, chemical composition and energies of the ionization edges.^[102,103] In some special systems, such as single-layer graphene, the mass loss can be quantified by counting the knockout atoms as a function of electron dose applied using high-resolution transmission electron microscopy (HRTEM) (Figure 2c,d).^[45]

The third strategy quantitatively measures the local and collective structural evolutions associated with chemical bonding, coordination environment and electronic structure upon electron beam irradiation,^[56,99,100,104–108] via either the fine structures of the ionization edge or the low-loss regime in EELS spectroscopy.^[99,100,104–106] The former feature allows the monitoring of beam-induced local structural destruction associated with chemical states,^[106] bond hybridizations^[108] and coordination environment,^[107] while the latter is related with the loss of collective structural properties such as plasmons and phonons.^[99] For example, to monitor the beam damage behaviors in a π -conjugated sp^2 carbon network, the destruction of sp^2 carbon species can be tracked by the intensity evolutions of either the $\sigma \rightarrow \pi^*$ peak in the carbon K-edge fine structure or the π -plasmon peak in the low-loss regime of EELS spectroscopy.^[109] As another example, the characteristic $\pi-\pi^*$ electronic transition features are used to discriminate different components in organic polymer films and quantify their respective dose-dependent structural damages (Figure 2e,f).^[99] To monitor the beam damage behaviors in SiO_2 , O–O peroxy species have been reported as a good indicator for EELS through the O K-edge fine structures.^[56]

The quantitative measurement of beam damage through the above-mentioned three strategies can be carried out by monitoring the decay curves of certain features (i.e., either intensities of diffraction spots or peaks in the core- or low-loss regimes of EELS spectroscopy). The dose-rate threshold and dose-rate effects of materials can be directly monitored from the intensity decay versus dose rate, while the critical dose can be extracted from the decay curves versus accumulated dose by taking into consideration of the beam damage kinetics. Both of the two primary beam damage mechanisms, radiolysis and knock-on displacement, are dose-dependent and thus have their respective critical doses. For the radiolysis mechanism, despite a few exceptions,^[7,69,110–117] the beam damage rate in most cases follows the first-order decay kinetics as below

$$I_D = I_0 e^{-\frac{D}{D_c}} \quad (1)$$

where the “ I_0 ” and “ I_D ” refer to initial and remnant intensities of monitored feature at an accumulated electron dose of “ D ”. An accumulated critical dose of “ D_c ” at an I_D/I_0 ratio of $1/e$ is widely used as a benchmark for evaluating the beam sensitivity of materials.^[59] Notably, the critical dose measured via different strategies are usually quite different because the loss of structural order is usually prior to the loss of mass due to the extra dose required to displace the chemical species over large distance toward surface sputtering.^[57] While the damage of electronic structures is even earlier for most specimens.^[99] As an example, the critical dose of polymer P3HT measured from the low-loss EELS regime for $\pi-\pi^*$ transitions is an order of magnitude smaller than that measured from the fading dynamics of diffraction peaks.^[99] Similar phenomenon is observed on Cu-phthalocyanine as a molecular crystal with a critical dose determined

from EELS fine structures decreased by a factor of five compared with that determined by electron diffraction.^[57,59,118]

On the other hand, the beam damages associated with knock-on displacement can be quantitatively measured by means of the mass loss through surface sputtering, which follows a zero-order beam damage kinetics as below^[57]

$$I_D = I_0 (1 - \sigma_d D) \quad (2)$$

where the remnant intensity of monitored feature decays linearly with the accumulated dose. Instead of a critical dose, a displacement cross-section “ σ_d ” is usually used as a benchmark for evaluating the knock-on damage.^[57]

2.4. Structural Sensitivity against Electron Beam Damage

2.4.1. Structural Aspects for Beam Damage Studies

The beam damage mechanisms have been widely studied and documented, with an emphasis on the electron beam conditions and electron–matter interactions.^[59] Actually, the beam sensitivity of materials are essentially determined by their structures, including effects arising from chemical bonding, coordination environment, valence state, porosity, defect, crystal size, and shape. In this section, these structural aspects for beam damage behaviors have been systematically summarized, which are classified into categories including crystal structures, microstructures and morphologies.

2.4.2. Crystal Structural Effects

The two important structural parameters associated with the crystal structure of materials are chemical bonding and coordination geometry. They both play a decisive role in the structural damage against either beam-induced ionization or knock-on displacement, which has been extensively investigated over a wide range of materials.

As an important category of beam-sensitive materials, MOFs are composed of metal ions or clusters coordinated with organic linkers, which form a porous crystalline framework.^[119] Although there lacks a systematic study on the beam damage behaviors of MOFs, their distinct crystal structures usually lead to quite different sensitivity against electron beam irradiation. For example, UiO-66(Zr) adopts a quite rigid framework with 12-coordinated Zr ions and quite covalent Zr–O bonds.^[120] Accordingly, the high-frequency diffraction peak at $\approx 5 \text{ nm}^{-1}$ starts to fade when the cumulative dose reaches about $17 \text{ e } \text{\AA}^{-2}$.^[34] In contrast, ZIF-8(Zn) composed of 4-coordinated Zn ions with quite ionic Zn–N bonds has its diffraction peaks at a much lower spatial frequency faded under a similar dose of $\approx 25 \text{ e } \text{\AA}^{-2}$ and completely loses its crystallinity at only $\approx 75 \text{ e } \text{\AA}^{-2}$.^[35,49] The chemical bonding also determines the critical doses of organic compounds. The PCBM polymer exhibits a critical dose that is over an order of magnitude greater than that of P3HT polymer, which is attributed to the presence of conjugated π -electron system in fullerenes and lack of C–H bonds.^[99] Similarly, aliphatic compounds are usually more

beam-sensitive than aromatic ones,^[57] the latter of which are also stabilized by π -electrons.

The chemical bonding strength is also closely associated with the chemical composition.^[57,99,121] It is observed that the substitution of hydrogen atoms in aliphatic and aromatic compounds by different halide functional groups remarkably enhances their beam durability, arising from the increased steric hindrance against atomic displacement.^[57,59,122,123] On the other side, it is widely reported that organic–inorganic hybrid perovskite (MPbX₃ with X: Cl, Br, I and M: HC(NH₂)₂, CH₃NH₃) are much more beam sensitive than its inorganic counterpart with organic ions replaced by Cs⁺ ions.^[34,37] Specifically, inorganic perovskite can withstand a dose rate of $\approx 100 \text{ e } \text{\AA}^{-2} \text{ s}^{-1}$ and a cumulative dose of a few thousands electrons \AA^{-2} ^[37] while the organic–inorganic hybrid perovskite may tolerate a dose rate of $\approx 4 \text{ e } \text{\AA}^{-2} \text{ s}^{-1}$ and a cumulative dose of only a few electrons \AA^{-2} .^[34] The possible reasons for the beam sensitivity of these perovskites lie in the fact that the Pb–X bonds in their crystal structures are less covalent and moreover the Pb²⁺ ions are easily subject to reduction by the electron beam.^[124,125]

The crystal structural effect on the beam damage can be further extended to a “zone-axis effect” due to the different structural projections along diverse zone axes. As an example, the orientation-dependent beam damage behaviors of rutile TiO₂ have been systematically studied.^[61] When TiO₂ is viewed along the [001] orientation, a continuous phase transition from TiO₂ to α -Ti₂O₃ and to γ -TiO occurs. When [101] or [110] orientation is aligned, there are defects and surface roughness generated on TiO₂ respectively, which finally lead to the formation of voids. In addition, a threefold superstructure appears upon beam irradiation along the [100] zone axis, while α -Ti₂O₃ would form once imaged along the [111] direction.

2.4.3. Microstructural Effects

The microstructural effects, arising from porosity or defect, are also important for beam damage behaviors.^[126,127] Actually, many porous materials, such as zeolites, COFs and MOFs, are highly beam-sensitive.^[21,24,29,34,35,128] Their beam damage mechanisms are usually dominated by radiolysis.^[128] The typical critical doses for aluminosilicate zeolites are within a few hundreds of electrons \AA^{-2} .^[129] While the typical critical doses for MOFs and COFs are even lower, ranging from a few to a few tens of electrons \AA^{-2} .^[29,34,35] The introduction of porosity into materials usually decreases their mechanical strength. Xu et al. observed a strong tradeoff between porosity and elastic modulus for amorphous porous silicas^[130,131] For zeolites as crystalline porous silicas, such as MFI, FER, BEA, MEL, and CHA types, their measured elastic modulus are usually within the range of 10–50 GPa, which fall far below those of dense oxides like SiO₂ (>100 GPa).^[131,132] Accordingly, zeolites of almost all types are much more irradiation-vulnerable than their dense phase counterparts (silicates). Similarly, for MOFs and COFs as hybrid or organic porous materials, including TAPB-TPOC₆-COF, MOF-5, HKUST-1, and majority of ZIFs, their elastic modulus are usually less than 10 GPa,^[133,134] which fall well below those of dense hybrids like zinc or copper phosphonoacetate polymorphs, lanthanum

pyridinedicarboxylate and cerium oxalate formate.^[133] The decreased framework stiffness of porous materials compared with dense materials tends to introduce large structural deformations upon bond breakage and atomic displacement as a result of beam damage, which might result in more rapid loss of crystallinity.

The defects, in terms of either point defects, cluster defects, dislocations, stacking faults, or grain boundaries, are usually associated with locally modulated coordination environment,^[135] dangling bonds,^[136,137] and largely weakened framework stiffness,^[138] and account for the drastically increased beam sensitivity of materials.^[25,139] Susi et al. observed that the nitrogen doping into graphene and single-wall carbon nanotube (SWCNT) introduces noticeable knock-on damage under 80 kV, which should have not existed in corresponding pristine structures.^[25] Such damage is triggered by the sputtering of carbon atoms neighboring the substitutional nitrogen dopants rather than the dopants themselves, which leads to the formation of pyridinic sites.^[25] Moreover, the displacement thresholds and cross-sections are closely related with the exact dopant configurations in graphene as shown in **Figure 3a–d**. In another study (**Figure 3e**), the beam damage behaviors of pristine SWCNT and defective SWCNT can be directly monitored and compared.^[140] It is observed that the defective SWCNT exhibits noticeable structural damage while the pristine SWCNT only exhibits small distortions under electron beam irradiation. With prolonged irradiation, the whole defective SWCNT is completely destroyed while the pristine SWCNT still maintains the original morphology with slightly more remarkable distortions. These results indicate that the possibly low-coordinated defective sites are much more easily ionized by electron beam compared with perfect structures. The defects also play a considerable role in beam damage behaviors over metallic nanostructures. Zhu et al. observed the beam-induced structural evolution of an ultrathin helical Au nanowire with a Boerdijk–Coxeter–Bernal (BCB) structure, which is constructed by face-sharing face-centered cubic (fcc) packed tetrahedra through nanotwinning.^[139] Without the protection from surface ligands, the beam irradiation easily drives the phase transformation from the helical BCB structure to the more stable fcc structure accompanied by the disappearance of twin boundaries (**Figure 3f**), which are well reproduced by the corresponding phase transformation simulations (**Figure 3g**).

2.4.4. Morphological Effects

Morphological effects on electron beam damage, especially the size effects, are remarkable at the nanometer scale where marked changes in physicochemical properties and electronic structures take place.^[141] For example, the size effect on beam damage is usually not significant for metallic nanostructures large than 5 nm, but could be prominent when approaching nanometer-scale,^[142] which refer to materials with reduced dimensionality.^[139,143,144] For 1D nanostructure systems, Lacroix observed the degradation process of 1D ultrathin Au nanowires.^[144] It is found the degradation of Au nanowires is extremely fast at 80 kV under a very low electron dose rate ($0.0145 \text{ e } \text{\AA}^{-2} \text{ s}^{-1}$) because of the radiolytic damage. In contrast,

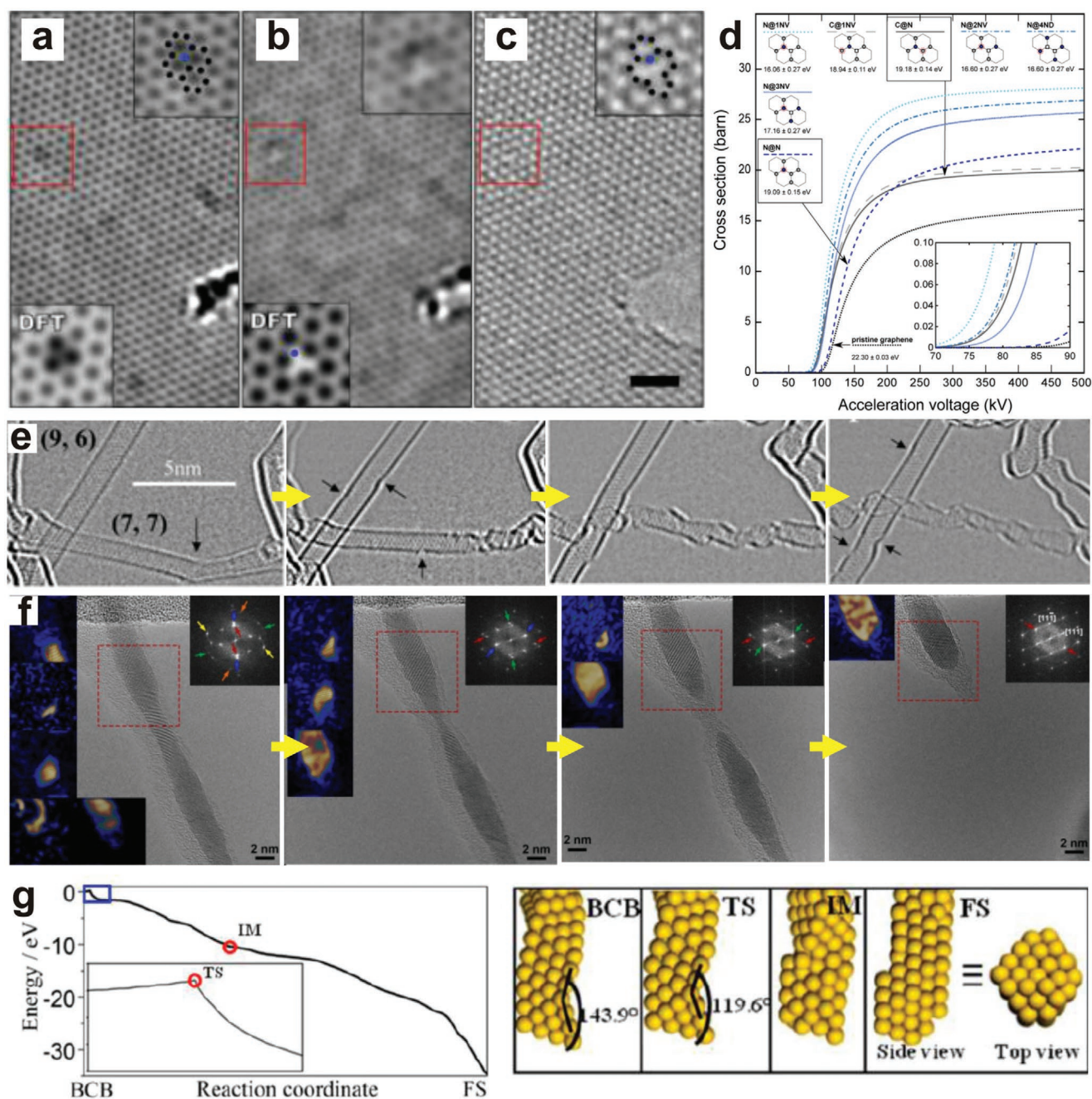


Figure 3. The microstructural effects on electron beam damage. a–c) TEM images of N-graphene recorded at 80 kV. The upper right insets are magnified images of the areas in red squares. d) The plot showing the cross-sections versus the calculated displacement thresholds for different dopant configurations in graphene. Reproduced with permission.^[25] Copyright 2012, American Chemical Society. e) HRTEM images of SWCNTs structural dynamics against beam irradiation. Reproduced with permission.^[140] Copyright 2009, American Chemical Society. f) HRTEM images of structural transformation from BCB tetrahelix to fcc Au nanowire under beam irradiation (insets are: left, Bragg-filtered images; right, FFTs). g) Simulated energy profile and models showing structural dynamics without the ligand protection. Reproduced with permission.^[139] Copyright 2014, American Chemical Society.

the degradation at 300 kV with a dose rate of $1.1 \text{ e } \text{\AA}^{-2} \text{ s}^{-1}$ is relatively slow, arising from the high threshold of knock-on damage for Au nanostructures. Similar phenomenon is observed on a ultrathin helical Au nanowire.^[139] An important beam-induced morphological evolution for such 1D metallic nanostructures arises from the Rayleigh instability effect, which would transform the cylindrical nanowires into spherical

particles in order to minimize the surface energy.^[145] This effect is directly monitored on an ultrathin Au nanowire via electron beam heating, which leads to a locally “distributed” Rayleigh instability behavior as shown in Figure 4a,b. The breakup dynamics of an ultrathin [111] grown Au nanowire due to Rayleigh instability can also be simulated using Kinetic Monte Carlo simulations under an elevated temperature, which

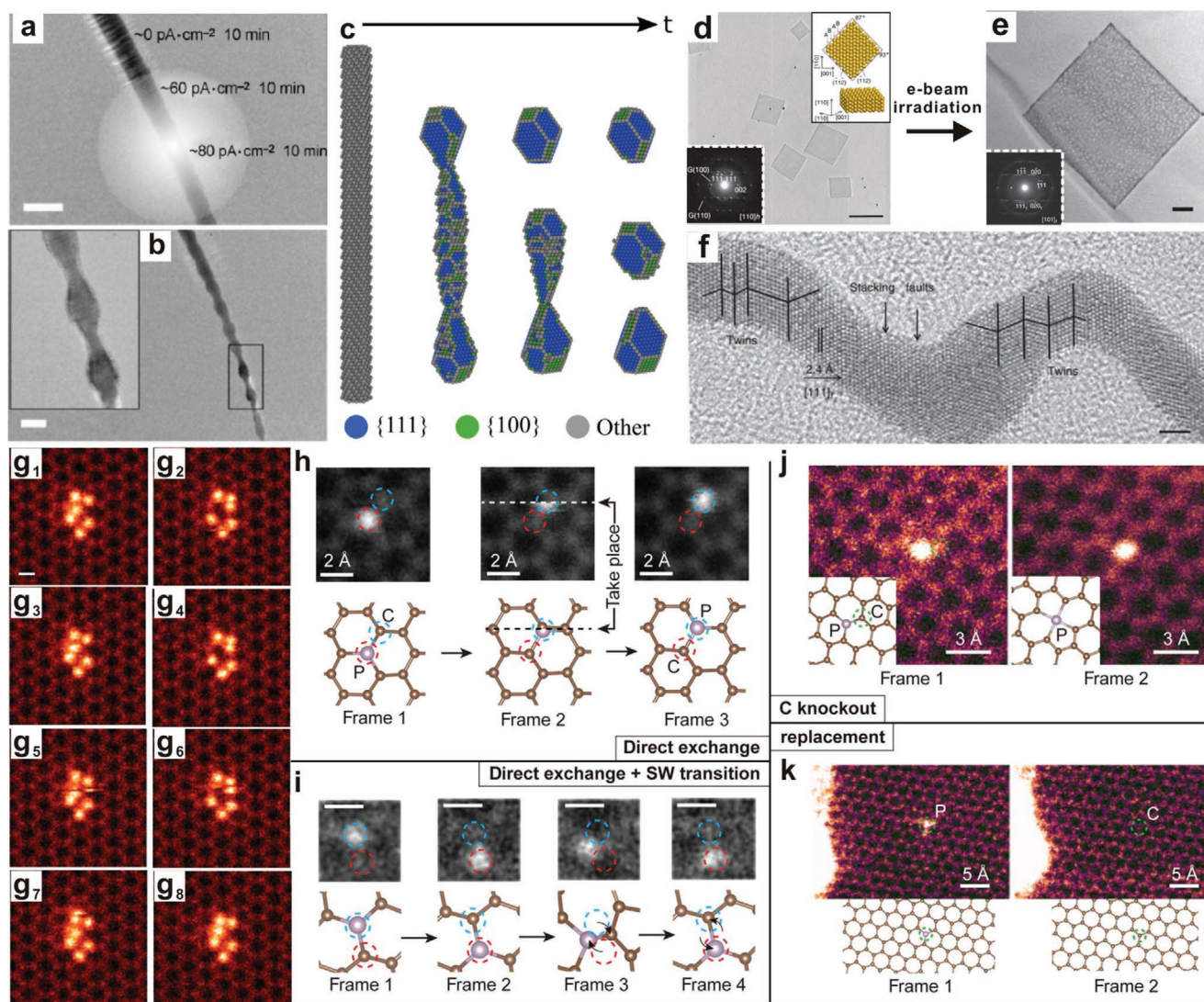


Figure 4. The morphological effects on electron beam damage. a,b) TEM image and c) atomic model from simulations showing Rayleigh instability behavior of Au nanowire. a,b) Reproduced with permission.^[145] Copyright 2017, Springer. c) Reproduced with permission.^[146] Copyright 2018 IOP Publishing. TEM image (insets are SAED pattern and model) of the hcp Au nanosheets before d–f) after electron beam irradiation. Reproduced with permission.^[147] Copyright 2011, Springer Nature. g) Sequential STEM-ADF Z-contrast images of the Si₆ cluster embedded in a graphene pore. Reproduced with permission.^[149] Copyright 2013, Springer Nature. h) Medium-angle ADF images and models showing h) direct exchange, i) both direct exchange and SW transition between P atom and a C neighbor (scale bars, 2 Å), j) the knocking out of C atom by electron beam and k) the replacement of P dopant by a C atom. Reproduced with permission.^[148] Copyright 2019, American Association for the Advancement of Science (AAAS).

results in more stable nanoclusters bounded by {111} facets through surface diffusion (Figure 4c).^[146] On the other hand, as a typical 2D nanostructure system, ultrathin Au nanosheets with hexagonal close packing (hcp) structure are also subject to remarkable electron beam damage,^[147] which quickly lose their ultrathin nanosheet morphology and generate abundant pores with thicker pore walls (Figure 4d). Combining selected area electron diffraction (SAED) and HRTEM of individual pore walls (Figure 4e,f), this morphological evolution is accompanied with the hcp to fcc phase transformation and the formation of nanotwins and stacking faults.^[147] For 0D nanostructure systems, especially those with ultrasizes down to clusters or even single atoms, the knock-on damage becomes significant.^[148–150] Such damage scheme would introduce

considerable structural evolutions and dynamics through atomic displacements or even knockout, which in most cases are irreversible.^[150–152] Lee et al. observed the reversible structural dynamics of a Si₆ cluster trapped in a graphene nanopore.^[149] As is shown in Figure 4g, the reversible dynamics feature the back-and-forth displacement of a single Si atom within the whole cluster, which is driven by the kinetic energy transferred from the 60 keV electron beam below the knock-out threshold energy for Si atoms. Su et al. further classified those elementary steps for beam-induced dynamics of single-atom dopants in graphene into two categories (Figure 4h–k): i) atom-conserving steps, including direct exchange and Stone–Wales (SW) transition; ii) atom-nonconserving steps, including knockout and replacement.^[148]

Curvature is another important morphological feature that usually applies to tubular nanostructures and is associated with the atomic displacement threshold energies and electronic excitations.^[25,153] The diameter-dependent stability of SWCNT has been studied at 80 kV, which is below its knock-on damage threshold of pristine graphene.^[140] It is observed that the SWCNTs with a size below 1 nm suffer significant structural damages under electron beam irradiation while those with a size of 2.3 nm remain stable. The physical origin has been well reviewed and summarized,^[25] which is attributed to the curvature-dependent displacement thresholds of SWCNTs. For SWCNTs with a diameter of ≈ 2 nm, the displacement thresholds approach those of pristine graphene. These values remarkably decrease with increased curvature for SWCNTs with smaller diameters.

3. Technological and Methodological Innovations

3.1. General Implications

As mentioned above, beam-sensitive materials exhibit different beam damage mechanisms and thus distinct responses to the beam energy and dose rate. For example, materials dominated by ionization damage are more vulnerable to electron beams of lower energy.^[21,59] On the other hand, materials with an inverse dose rate effect prefer a higher dose rate within a given cumulative dose, while those with a direct dose rate effect tend to withstand a characteristic dose rate before their structure quickly degrades.^[57] According to Egerton,^[154] the critical dose for most dose-sensitive materials is so low that under such a dose the image resolution is no longer determined by the instrument but the electron dose used for imaging, due to the poor SNR. The dose-limited resolution (δ) can be defined by the following equation^[154]

$$\delta = \text{SNR DQE}^{-\frac{1}{2}} C^{-1} F^{-\frac{1}{2}} (D_c/e)^{-\frac{1}{2}} \quad (3)$$

where i) “SNR” refers to an SNR to measure signals with a target degree of uncertainty and a “Rose criterion” states an SNR of at least 5 to distinguish features with 100% certainty;^[155,156] ii) “DQE” refers to the quantum detection efficiency of the electron detectors; iii) “C” refers to the contrast between resolution elements (related with peak-to-background ratio, PBR);^[154] iv) “F” refers to the signal efficiency (i.e., fraction of primary electrons reaching the detector and used for image formation); and v) “ D_c ” is the critical electron dose.

Actually, the dose-limited resolution equation itself also provides general problem-solving strategies. Specifically, for the DQE term, an electron detector with high detection efficiency, for example coupled with direct-detection and electron counting techniques will benefit for enhanced image SNR and resolution as reviewed in Section 3.4; The contrast term, is strongly related with imaging mode and detectors. For example, diverse phase contrast imaging modes would result in different contrast transfer forms and can be further modulated by either prespecimen or postspecimen phase plate.^[157] These points will be mainly introduced in Sections 3.3 and 3.4.

The signal efficiency term F is usually higher for bright-field imaging than dark-field imaging modes due to the difference in number of electrons collected by their respective detectors.^[154] The critical dose D_c term, as can be experimentally measured (Section 2.3), is a resolution-limiting factor. It is mainly determined by a combination of effects arising from the crystal structural, microstructural and morphological properties of materials, as clearly demonstrated in Section 2.4, based on the principles of electron–matter interaction and mechanisms of electron beam damage as reviewed in Sections 2.1 and 2.2. There are many technological and methodological strategies to overcome the D_c barrier and improve the image resolution limited by dose. Through the electron optics system (Sections 3.2), the D_c values of materials can be modulated by beam energy, beam current density, and imaging modes due to their different beam damage mechanisms and dose-rate effects.^[75,158] Even with the same D_c values, the beam damages can be effectively minimized or retarded by employing either a sparsely sampled, a pulsed or an aloof electron probe.^[7,159,160] Similar idea can be extended to high-fidelity 3D reconstruction by low-dose orientation sampling. Moreover, as described in Section 3.3, the D_c values can also be enhanced by diverse specimen treatment methods, including specimen coating or freezing.^[49,57] These cutting-edge dose-efficient EM technologies and methodologies have led to groundbreaking scientific discoveries associated with diverse beam-sensitive materials, as reviewed in Section 4.

3.2. Strategies Associated with Electron Optics System

3.2.1. Electron Energy Modulation

Low-kV Imaging Assisted by Monochromator or Cold-FEG: The knock-on damage may be greatly eased below a threshold voltage because of its dependence on the threshold energy of atomic displacement.^[161] Accordingly, low-kV imaging significantly reduces the knock-on damage and also enhances the image contrast,^[154,162] but at the expenses of increased radiolytic damage as well as compromised image resolution and penetration depth.^[139,163] In principle, the focal spread that determines the information limit of an HRTEM image is basically limited by chromatic aberration of the objective lens and energy spread of the beam.^[164,165] To improve the image resolution under low-kV, two simple strategies are straightforward: i) to decrease the specimen thickness for minimized chromatic aberration effects on the resolution degradation and ii) to minimize the energy spread of electron beam by using a monochromator^[158,166–169] or cold-FEG.^[170]

There are different types of monochromator architectures,^[171] while a key design lies in the generation of an achromatic and stigmatic illumination by employing an energy-dispersive deflector that allows the utilization of electron beam within a specific energy range upon an energy selection slit (Figure 5a).^[169] Morishita imaged the gold nanoparticles under low-kV with a monochromator and a Delta-type Cs corrector.^[158] As shown in Figure 5b–e, compared with the TEM image taken with a non-monochromated source, the one taken with a monochromated source has largely improved image resolution. Moreover, the monochromated and Cs-corrected HRTEM

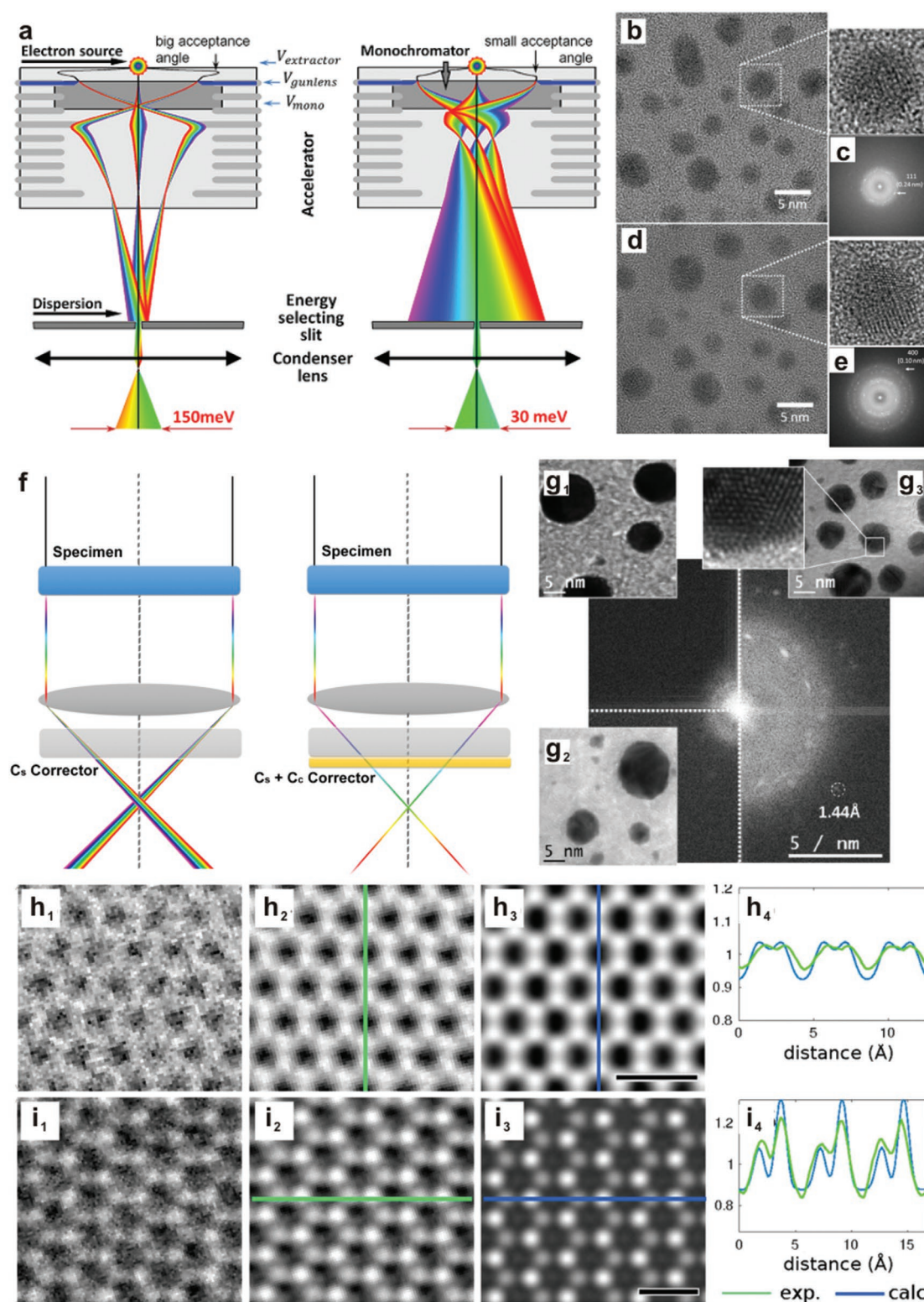


Figure 5. a) The ray diagrams without or with monochromator. Reproduced with permission.^[169] Copyright 2018, Elsevier. b,d) TEM images and c,e) corresponding FFT patterns of Au nano-particles measured at voltage of 60 kV with b) non-monochromated source and d) monochromated source. Reproduced with permission.^[158] Copyright 2015 IOP Publishing. f) Simplified sketch of ray diagrams for Cs corrected and Cs + Cc corrected configurations. g) TEM images of gold clusters obtained by g₁) an uncorrected TEM, g₂) a Cs-only corrected TEM, and g₃) the Cc + Cs corrected SALVE instrument. Experimental and calculated Cc/Cs-corrected 30-kV HRTEM images of graphene ($2.5 \times 10^6 \text{ e nm}^{-2}$) h) and MoS₂ ($3.0 \times 10^5 \text{ e nm}^{-2}$) i). h₁,i₁) The magnified images. h₂,i₂) The averaged experimental images. h₃,i₃) The simulated images. h₄,i₄) The corresponding line profiles. Reproduced with permission.^[174] Copyright 2016, APS Physics.

image shows the lattice transfer up to 213 pm for a single-layer graphene at 20 kV with high image contrast.^[172] Nowadays, the best achievable resolution of low-kV TEM imaging is even well beyond 0.5 Å once a monochromator is equipped.^[173]

Low-kV Imaging Combined with Cs + Cc Correction: Typically, chromatic aberration restricts the focal spread and image information limit below 100 kV, while spherical aberration (Cs) becomes the dominant resolution-limiting factor beyond 100 kV.^[175] The decrease of the voltage could reduce the knock-on damage, but increase the radiolysis. Thus, the final choice of voltage might depend on a compromise between radiolysis and knock-on damage for a specific specimen, when both chromatic and spherical aberrations may play a comparable role determine the image resolution. An ultimate approach that combines both the spherical and chromatic aberration corrections allows the atomic-resolution TEM observations on beam-sensitive materials at low voltage in range of 20–80 kV.^[174,176] A representative microscope that has both Cc and Cs correctors is constructed in three phases of the SALVE (sub-Ångström low-voltage electron microscopy) project in Ulm University.^[172] The corrector is consisted of

eight multipoles.^[174] The superposition of electrostatic and magnetostatic quadrupole fields are used to correct the chromatic aberration while a certain combination of magnetostatic octupole fields is applied to correct the spherical aberration.^[174] A simplified ray diagram containing Cs corrector and Cs/Cc correctors are compared in Figure 5f. Figure 5g compares the TEM images of Au clusters obtained by an uncorrected TEM, a Cs-only corrected TEM and the Cc/Cs-corrected SALVE TEM.^[158] Only the image obtained by Cc/Cs-corrected TEM shows the Au clusters atomically. Besides, Figure 5h,i shows both the experimental and calculated Cc/Cs-corrected 30 kV HRTEM images of graphene and MoS₂. Moreover, the resolution of HRTEM images collected from a Cc/Cs-corrected electron microscope could be better than 0.14 nm at a voltage as low as 20 kV.^[174]

3.2.2. Imaging Mode Selection

TEM versus STEM Imaging: There are two fundamental operation modes of TEM (Figure 6): parallel beam illumination

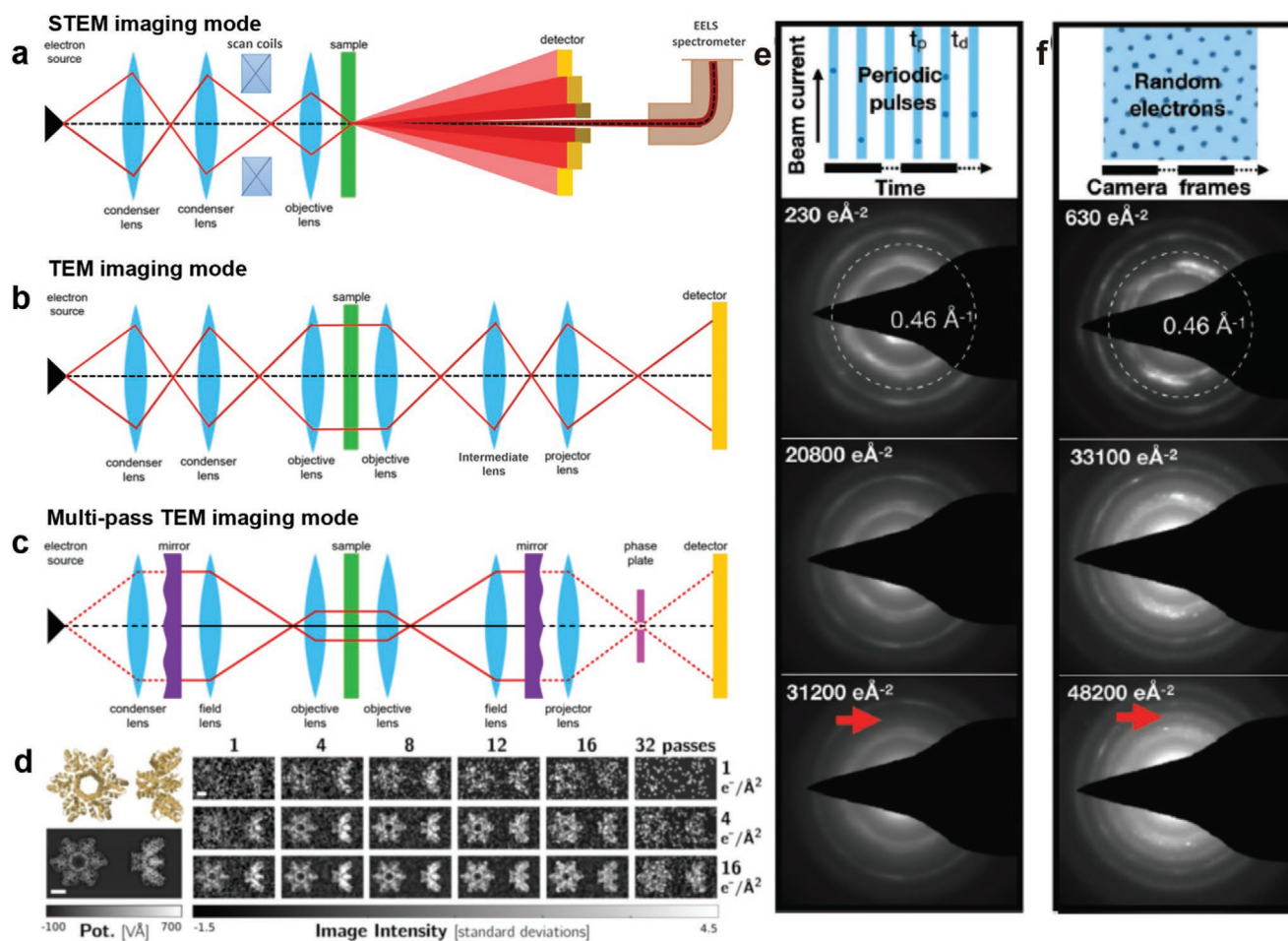


Figure 6. The ray diagrams of a) STEM imaging mode, b) TEM imaging mode, and c) Multipass TEM imaging mode. d) Model and the simulated TEM images of HIV-1 Gag protein at different electron doses for different numbers of passes. Reproduced with permission.^[177] Copyright 2017, Cambridge University Press. e) Schematics of pulsed beam (dose rate: 52 e⁻ Å⁻² s⁻¹) and f) continuous wave illumination (dose rate: 630 e⁻ Å⁻² s⁻¹) together with recorded diffraction patterns. Red arrows indicate the position of the $g = 0.46 \text{ Å}^{-1}$ scattering vector that is unique to $\beta\text{-MgCl}_2$. Reproduced with permission.^[7] Copyright 2019, Wiley-VCH.

(TEM) and scanning beam illumination with a highly focused probe (STEM). The configuration of STEM mode closely resembles that of TEM mode, but with the optics reversed.^[52] A significant difference between the two imaging modes lies in the beam condition, which is crucial for imaging beam-sensitive materials.^[57] Generally, TEM mode has a uniform and continuous illumination onto the specimen while STEM mode has a much more intensive instantaneous illumination together with an accumulated dose 10^4 – 10^5 times higher.^[75] Although advanced electron detection technology, such as direct-detection and pixelated cameras, has drastically brought down the typical dose used for imaging several orders of magnitude for both imaging modes,^[34,35,49,135] their distinct beam conditions are suited for imaging beam-sensitive materials with different dose-rate effects. For materials with a direct dose-rate effect (e.g., damage dominant by heating or charging^[57]), which have elevated damage per unit dose with increased dose rate, TEM mode usually leads to less structural damage. For those with an inverse dose-rate effect (e.g., damage dominant by slow diffusion-limited mass loss or precipitation^[57]), which have decreased damage per unit dose with increased dose-rate, STEM mode may provide a better choice.

Multipass TEM Imaging: For any EM imaging techniques that use uncorrelated electrons as the probe, there is a finite SNR associated the electron counting statistics (shot noise or Poisson noise) and arising from the discrete nature of electrons.^[178] The SNR is proportional to the square root of the number of electrons detected.^[93] In other words, for applications that restrict the cumulative electron dose (e.g., imaging beam-sensitive materials), the shot noise would be a limiting factor for the image SNR and resolution.^[154] This limit can actually be overcome by introducing correlated electrons as the probe, which reduces the counting error down to the Heisenberg limit^[179] and results in a squared SNR of shot noise. There have been many proposals to create correlated probing particles, most of which are however practically unrealistic. Kasevich and co-workers proposed a design of multipass TEM that allows the creation of correlated electrons by passing the phase object multiple times, which could be used to enhance the resolution of TEM images limited by dose.^[180] Compared with the typical TEM, multipass TEM add two more electron mirrors and a pulsed electron source (Figure 6c). The two mirrors allow the pulsed electron beam to pass through the sample multiple times,^[177] the total dose can thus be reduced to obtain an image with the same SNR. After a specific number of passes, the electron could be collected by the detectors. Figure 6d shows the simulated TEM images of HIV-1 Gag protein at different electron doses for different numbers of passes.^[177] It is observed that the SNR of the image reaches maximum at neither too many passes nor too few passes. It is straightforward that few passes lead to low SNR, while the low SNR at a high number of passes is possibly ascribed to the phase wrapping or inelastic losses.^[177]

Ultrafast TEM Imaging: Inspired by the successful applications of high-intensity X-ray free-electron lasers (XFELs) in resolving structures of biological macromolecules through “diffract-and-destroy” scheme,^[181–184] the possibility of using short electron pulses to probe electron beam-sensitive materials have also been explored.^[7,51,185] The timescales and

mechanisms for outrunning the radiation damage with either XFELs or pulsed electrons have been compared.^[51,185] XFELs employ repetitive femtosecond X-ray pulses (<100 fs) that outrun primary ionization damage,^[51,185–187] while pulsed electrons can hardly achieve very short period with sufficiently high brightness due to the Coulomb repulsion between the electrons in each bunch.^[185] Longer electron pulses allow the elimination of relatively slow secondary or tertiary damage processes (e.g., diffusion-limited processes^[57]) rather than the primary ionization damage,^[57,185] which would also be important for materials adopting inverse dose-rate effects^[57,69,188] or retarded damage upon dose fractionation.^[159,189–191] Moreover, pulsed electrons enable ultrafast electron microscopy (UEM) that provides structural dynamics in both reciprocal and real spaces with high temporal resolution,^[192,193] which is able to precisely track the phase transitions,^[6] Moiré fringe dynamics,^[194] crystallization phenomena^[195] and materials surface dynamics.^[196–198] As an excellent example for the application of pulsed electrons, a picosecond temporal electron illumination is used to track the beam damage dynamics of MgCl_2 at atomic resolution.^[7] Figure 6e,f compares the electron diffraction patterns obtained by pulsed beam irradiation and randomly delivered electrons irradiation at the same beam current of 0.5 nA, respectively.^[7] Under the electron beam irradiation, $\alpha\text{-MgCl}_2$ would transformed to $\beta\text{-MgCl}_2$, which can be identified by electron diffraction. The characteristic 0.46 \AA^{-1} scattering vector of $\beta\text{-MgCl}_2$ is absent when irradiated by pulsed beam while is present by random electron irradiation. Similar phenomenon was observed over a model linear saturated hydrocarbon (*n*-hexatriacontane, $\text{C}_{36}\text{H}_{74}$), where a repeatable reduction in beam damage was observed with femtosecond-timed single-electron packets.^[199] These results indicate the ultrafast pulsed beam could largely ease the electron beam damage perhaps through the phonon dissipation among individual electron packet.^[7]

3.2.3. Electron Beam Control

Nondestructive EELS through Aloof Mode: Knock-on damages are considerable once the threshold energy of the specimen is quite low. Moreover, radiolysis in many cases overwhelms the knock-on effects and is usually unavoidable, because radiolysis almost has no threshold energy.^[57] Ideally, a “nontouching” electron probe avoids these damage effects and allows the non-destructive investigation of structural and physicochemical properties of the specimens. To this end, the “aloof” beam EELS technique has been proposed by Warmack dating back to 1984^[200] and systematically reviewed by Crozier recently.^[160] This technique allows the off-site sensing of valence and vibrational signals from the near-surface regions of the specimen when the electron probe is placed away from the specimen. The mechanisms of aloof beam EELS technique are closely related with the delocalization nature of valence and phonon losses, which are based on the long-range electromagnetic interactions between electrons as near-field source and the specimen.^[160] Because of the “off-site” feature of aloof beam EELS, the knock-on damage is eliminated and the radiolysis is also largely minimized.^[160]

Specifically, the valence loss signals collected by aloof beam EELS mode are associated with those composition and dielectric response predominantly from the surface region. While the phonon loss signals are often attributed to those vibrational fingerprints of surface adsorbates and surface phonon modes of materials.^[160] Crozier reported the aloof beam vibrational EELS spectra of the beam-sensitive carbon nitride ($g\text{-CN}_x\text{H}_y$), from which the corresponding N–H stretching modes together with C–N and s-triazine ring modes are explicitly identified and match well with the FTIR spectrum.^[160] Rez applied this technique to analyze the biological materials.^[201] On the other hand, the nondestructive aloof beam EELS is even able to discriminate the ultrathin surface hydrate layers on the MgO nanocubes from hydroxide layers based on their distinct characteristic vibrational energy-loss peaks.^[202] An encouraging perspective on the applications of the aloof beam EELS technique lies in the in situ EM, where this technique is able to unravel the surface chemistry, reactions and dynamics for catalysts and functional materials under working conditions.

Low-Dose Imaging through Compressive Sensing: There are traditionally two strategies to achieve low-dose STEM imaging, by reducing either the pixel dwell time or the probe current. However, these methods significantly reduce the electron dose per pixel scanned by the electron probe and thus result in low image SNR and poor resolution. Moreover, the scanning coil will become unstable at extremely short pixel dwell time, and the optics needs to be realigned once the probe current is tuned with beam crossover moved.^[203] More recently, another low-dose STEM imaging strategy, compressive sensing (CS) STEM, has drawn a lot of attentions.^[204,205] Instead of reducing the pixel dwell time, the total number of scanned pixels are dramatically reduced but the information are well recovered from the far undersampled images. In this way, the overall accumulated electron dose within the field of view is significantly reduced while the effective dose impinged on those scanned pixels where information reside remains high.

The general sketch workflow of the CS based low-dose STEM image acquisition is shown in **Figure 7a**.^[206] A special form of low-dose CS-STEM imaging method, inpainting, is proposed to recover the undersampled STEM images without compromising the image resolution (Figure 7b).^[207] In contrast to the Bernoulli sampling method, the line-hopping method features the sparse sampling in lateral scans (Figure 7c), which allows the simultaneous achievements of high SNR, accurate reconstruction and fast acquisition.^[207] As shown in Figure 7d–g, CS-STEM with inpainting sampling method successfully recovers with high SNR the undersampled atomic-resolution STEM image of SrTiO_3 with 20% or 10% pixels sampled.^[159] Further undersampling with 5% pixels leads to considerable artefacts and information loss.

The CS method can be extended to in situ TEM imaging for image stack or video acquisition, in order to mitigate the slow readout problem for conventional electron detectors.^[208] Under a similar workflow, a series of coded images are compressed and assembled into one single frame, which is then recovered through diverse algorithms (e.g., the nonlocal means algorithm or generalized alternating projection). Accordingly, the frame rate and temporal resolution of most electron detectors can be improved, with reduced effective electron dose rate.^[208]

3.3. Strategies Associated with Specimen and Stage System

3.3.1. Specimen Freezing

The development of cryo-EM allows the unambiguous high-resolution structural elucidation of a wide range of biomolecules like proteins with typical critical doses in the range of 20–30 $\text{e}^- \text{\AA}^{-2}$.^[209] Such a technique promotes significant advances in structural biology and has been recently honored the Nobel prize, for the contributions from Jacques Dubochet, Joachim Frank, and Richard Henderson on sample preparations, single particle reconstruction and image processing, and electron crystallography, respectively.^[12,210]

In the first aspect, the utilization of cryogenic freezing, either in the microscope or holder, prepares the specimen in its frozen hydrated state, which allows the direct imaging of its native structures. This is particularly important for the structural analysis of noncrystalline biological materials. In a similar way, cryo-EM has been recently employed to characterize nanomaterials and their solid–liquid interfaces at high resolution.^[211] These solid–liquid hybrid nanomaterial systems are frozen first and then put onto the holder for EM imaging (**Figure 8a,b**).

In the second aspect, low-temperature imaging minimizes the radiolytic and heating damage for beam-sensitive materials, so as to increase their critical doses.^[212] Typically, the thermal vibrations required to achieve the energy–momentum conversion for electronic excitations are quenched by low temperature.^[64,65] This effect is significant for insulating materials such as MOFs, molecular crystals or polymers due to their more severe ionization damage.^[52] For example, MOFs are very beam-sensitive porous materials and would be completely amorphized through ionization under a typical dose for conventional HRTEM imaging.^[35] Using cryo-EM at liquid-nitrogen temperature, the pores of MOF-5 can be clearly resolved, as shown in Figure 8c–g.^[213] Cui and co-workers used the cryo-holder to image ZIF-8 nanocrystals and observed an elevated critical dose compared with conventional imaging conditions.^[49] The liquid nitrogen temperature also stabilizes the ZIF-8- CO_2 heterostructure and allows the identification of two distinct CO_2 binding sites and considerable lattice expansions within the framework of ZIF-8 (Figure 8h–j).^[49] As another example, the morphological evolution of beam-sensitive macromolecules can be directly monitored with subsecond time resolution using cryo-EM. The macromolecular self-assembly, nucleation, and growth processes can be clearly observed without considerable structural damage, which have been reported and summarized by Patterson et al.^[32] Leijten et al. quantitatively evaluate the beam damage effects on crystalline organic polymers and observe a significantly enhanced irradiation durability under cryogenic conditions, which increases the critical dose up to ≈ 7 times higher.^[79]

A considerable issue for cryo-EM is beam-induced specimen motion that degrades the image resolution,^[214] which is more severe for frozen hydrated biological samples.^[214] The development of ultrafast cameras allows the shorter exposures and acquisition of time-series EM images for motion tracking, which enable the recovery of high-frequency information through diverse “motion-correction” algorithms as discussed in the Section 3.4.2.

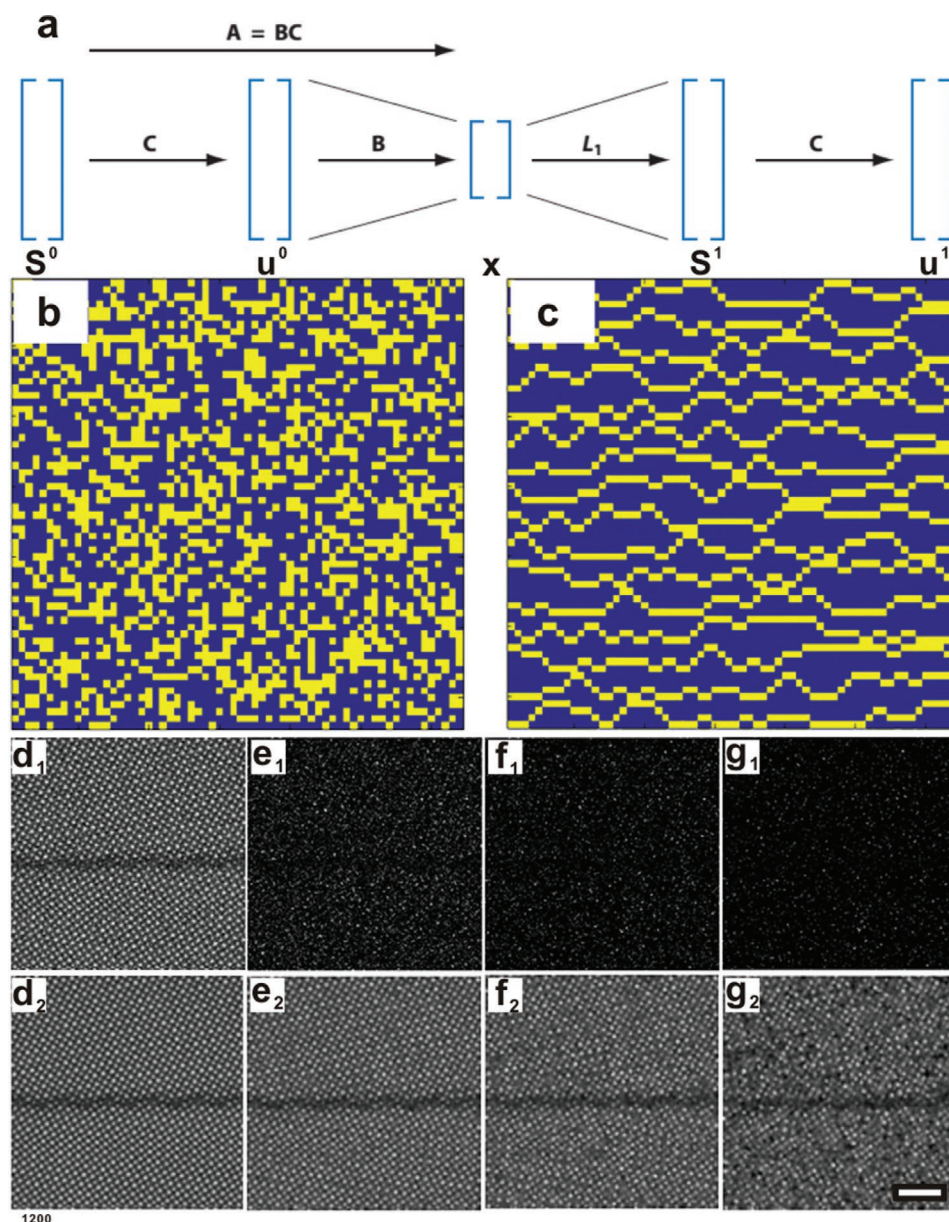


Figure 7. a) Schematic illustration of the CS framework with b) Bernoulli sparse sampling and c) line-hopping sparse sampling. The whole process includes: i) the transmission of high-dimensional signal u^0 derived by the matrix C and a sparse coefficient vector S^0 ; ii) then u^0 is compressed with measurements of B and recorded with a low-dimensional signal x ; iii) In the recovery process of the signal x , a sparse coefficient S^1 is estimated with method L^1 and then recover to u^1 with matrix C . a) Reproduced with permission.^[206] Copyright 2012, Annual Reviews. b,c) Reproduced with permission.^[207] Copyright 2016, AIP Publishing. d–g) The (under)sampled and reconstructed images: d₁–g₁) 100%, 20%, 10%, and 5% (under)sampled images, respectively. d₂–g₂) The corresponding reconstructed images. The 100% sampled image is denoised only (scale bar: 2 nm). Reproduced with permission.^[159] Copyright 2014, Oxford University Press.

3.3.2. Specimen Coating

Specimen coating is another effective method to decrease various types of electron beam damage and increase the critical dose. Through specimen coating, surface sputtering can be effectively minimized or even avoided when a thin film of either carbon, metal or metal oxide is applied as the protecting layer.^[215] Such a protecting layer itself should also fulfill several prerequisites, such as appropriate thickness and sputtering threshold.^[215] Thinness is needed because a thick protection layer would induce additional electron scattering and reduce

the image contrast. Similarly, a coating layer with a small sputtering threshold only delays the damage rather than avoiding it.^[215] An appropriate specimen coating could effectively reduce the mass loss and crystallinity degradation,^[57,59] because it provides a diffusion barrier for the light gaseous species, easing those damage effects associated with their emission from the surface. Regarding charging effects, coating the specimen with a conducting film (e.g., carbon) provides an effective solution.^[162] Such a conductive coating layer works especially well for cryo-EM samples that are nonconductive and suffer from strong charging effects. Furthermore, an ultrathin coating of

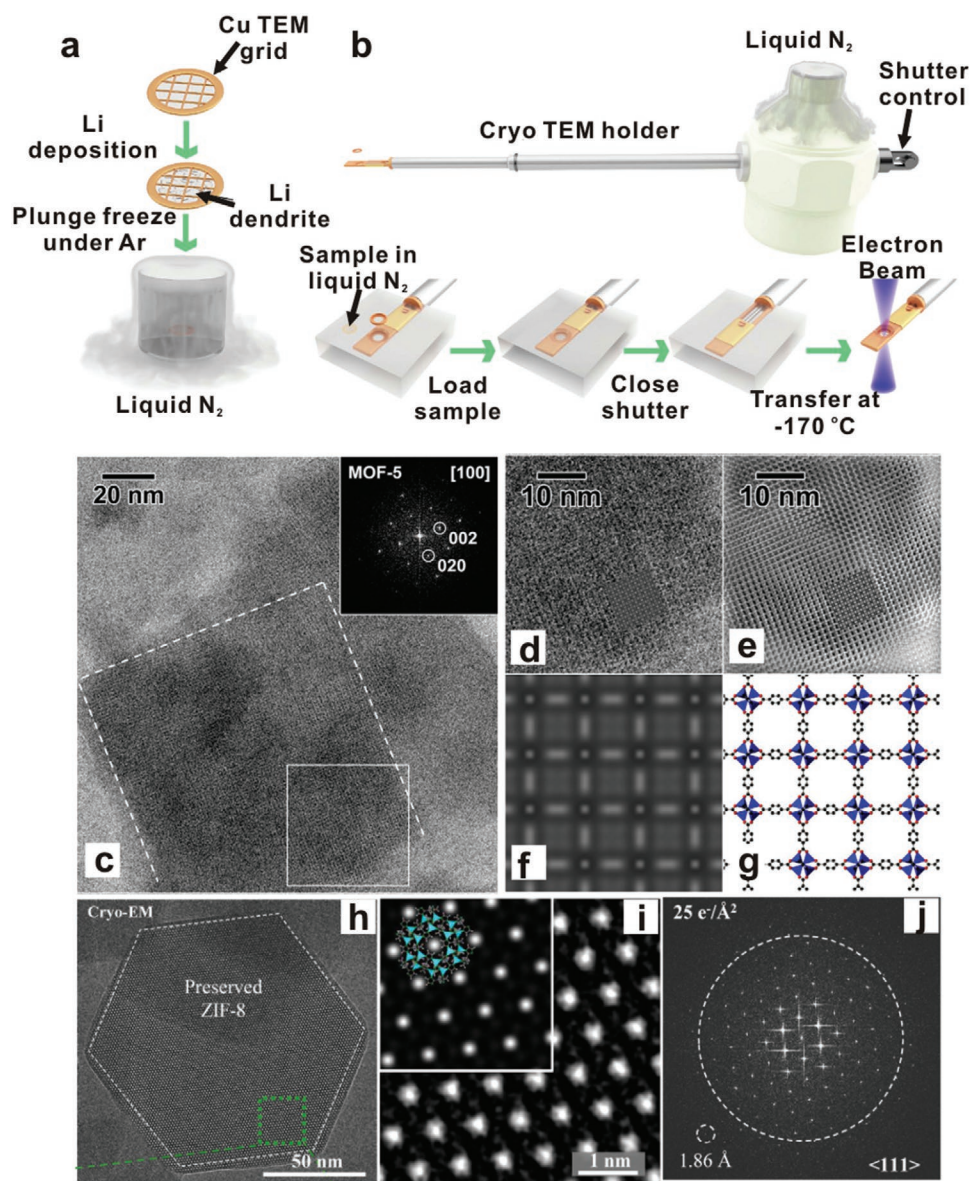


Figure 8. a,b) Schematic illustration of the “Cryo-transfer” process for transferring Li dendrite sample to the cryogenic TEM holder. Reproduced with permission.^[19] Copyright 2017, AAAS. c) HRTEM image of MOF-5 crystals with FFT as the inset. d) Experimental, e) filtered, and f) simulated HRTEM images of a local region indicated by the white box in (c). g) Structure of MOF-5. Reproduced with permission.^[213] Copyright 2012, Elsevier. h) Cryo-EM image of ZIF-8 (outlined by dashed white line) taken along the <111> direction at -170 °C with electron dose rate of $\approx 4.5 \text{ e}^- \text{Å}^{-2} \text{ s}^{-1}$ for 1.5 s. i) Magnified images of green boxed region from (g). j) Corresponding FFT pattern. Reproduced with permission.^[49] Copyright 2019, Elsevier.

continuous metal or dielectric layer on the specimen surfaces has also been reported to reduce radiolysis.^[57] An excellent specimen coating strategy utilize graphene as the protecting layer, as proposed by Ute Kaiser’s group and Novoselov’s group respectively.^[26,216] The ultrasmall thickness and high conductivity of graphene provide a promising solution to beam damage without compromising image contrast and resolution. It has been found that a protective graphene layer leads to an obvious improvement in the radiation tolerance of monolayer MoS₂.^[216] Additionally, graphene–MoS₂–graphene sandwich structures exhibit higher stability and lower defect formation rates, in contrast to either bare MoS₂ or an MoS₂–graphene bilayer configuration.^[26] In addition to the specimen coating, there are also

other specimen treatments that may effectively enhance their electron beam irradiation durability. For example, dehydration and chemical doping of the zeolites have been observed to remarkably stabilize their structures against electron beam irradiation.^[217,218] The dehydration and dioxygen treatment of organic thin films have also been proved to remarkably extend their critical doses under cryogenic conditions.^[79]

3.3.3. Low Dose (Rate) Orientation Sampling

Low-Dose Zone-Axis Alignment: According to the dose-limited resolution scheme,^[57] the image resolution is actually

determined by the maximum allowed electrons used for imaging before structural degradation. A complete workflow of low-dose TEM imaging for crystalline materials usually includes the following steps: i) specimen searching and tracking, ii) zone-axis alignment, iii) imaging mode switching and imaging condition tuning, iv) image acquisition, and v) image processing and analysis. Accordingly, within the electron dose upper limit, one should always maximize the dose used for image acquisition (step iv) and minimize the dose for pre-imaging operations (steps i–iii).

To achieve this, the specimen searching should be carried out under extremely low dose rates in the range of 10^{-3} to 10^{-2} e \AA^{-2} s $^{-1}$, with visibility enhanced by applying a large defocus or switching to diffraction mode.^[219] Then, a zone-axis alignment becomes a dose-limiting preimaging step for crystalline materials. Unlike conventional high-dose zone-axis alignment procedures that involve repetitive orientation sampling, an one-step Laue-circle-based zone-axis alignment procedure allows “tilting in the dark” with negligible dose consumption, i.e., far less than 1 e \AA^{-2} .^[34] The detailed procedure is demonstrated in **Figure 9**, which evaluates the off-axis deviation angle by fitting the Laue circle formed by the intersection of Ewald sphere with zero-order-Laue-zone. The deviation angle is then partitioned into the α - and β -tilt axes based on precalibrated stage tilts, which facilitates the one-step zone-axis alignment with an accuracy of 0.02° (Figure 9g).^[34] With such a protocol, accurate zone-axis alignment can be achieved on a wide range of beam-sensitive materials.^[34,135,137]

Low-Dose Electron Tomography: Conventional electron tomography (ET) as a high-dose technique, requires the sampling of a few tens to more than one hundred projections for the 3D reconstructions, which usually results in an accumulated dose

of $\approx 10^3$ e \AA^{-2} for low magnification^[220] or $\approx 10^6$ e \AA^{-2} for high magnification^[221] reconstructions, respectively. Hence, the application of conventional ET on beam-sensitive materials is very challenging. An effective strategy to markedly reduce the cumulative dose for ET is to reconstruct through undersampled tilt series. CS algorithms can be implemented in such low-dose ET scheme for constructing 3D tomograms through a greatly reduced number of stage tilts.^[222] Generally, CS requires the reconstructed object to be compressible, or sparse, in a certain domain. In other words, CS-ET aims to find a sparse representation of the reconstruction (solution) based on a set of ill-posed linear equations.^[223] There are two common sparse representations used for various objects: gradient and wavelet. For the tomographic reconstruction of most nanomaterials, it is usually reasonable to assume that the gradient of the object is sparse.^[224] Hence an reconstruction algorithm that simultaneously minimizes the difference between i) the data and the model and ii) the norm of discrete gradient (i.e., the total variation minimization, TVM) is often employed.^[225,226] CS-ET allows the reconstruction of biological specimens with a much higher SNR than the weighted back-projection (WBP) algorithm (Figure 10a).^[227] Saghi et al. use gradient-based CS-ET to reconstruct the 3D structure of a concave iron oxide from nine projections, which could not be achieved with the conventionally adopted simultaneous iterative reconstruction technique (SIRT).^[228] Moreover, based on only four zone axis projections along with extra restrictions from vacuum voxels, Goris et al. could reconstruct the 3D structure of Au nanorods at atomic resolution using gradient-based CS-ET for the explicit identification of surface termination and microfacets (Figure 10b).^[225]

Apart from CS algorithm, discrete tomography is another vital construction technique that utilizes undersampled tilt

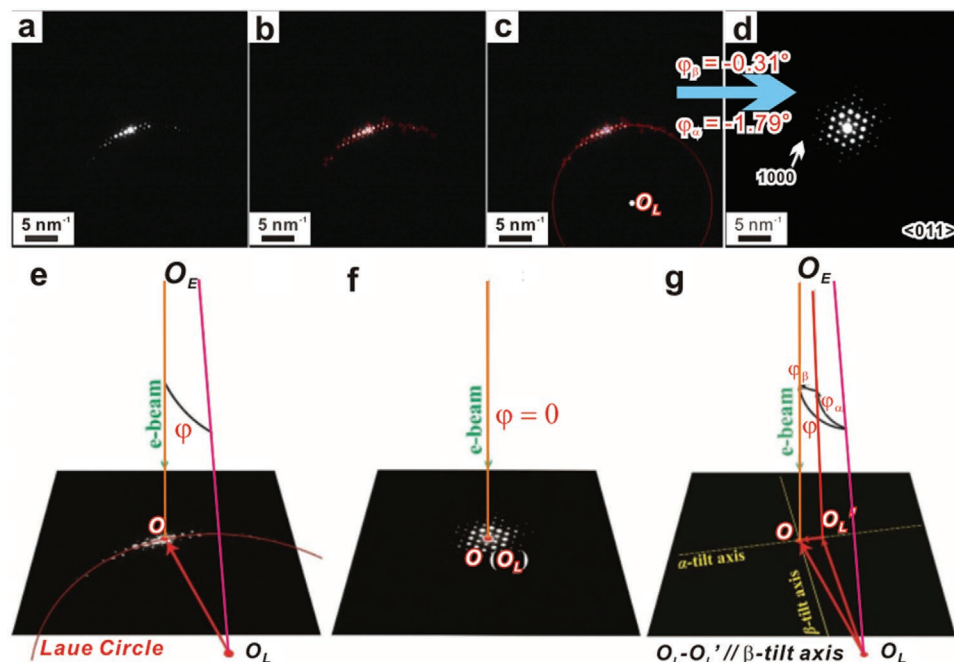


Figure 9. Schematic illustration of the “Laue-circle”-based zone-axis alignment procedure. SAED patterns with a) a slightly off-axis condition, b) peak labeled, c) the Laue circle delineated, and d) an on-axis condition after a single stage tilt. Illustration of e) the off-axis condition, f) the on-axis condition, and g) the alignment procedure. Reproduced with permission.^[34] Copyright 2018, AAAS.

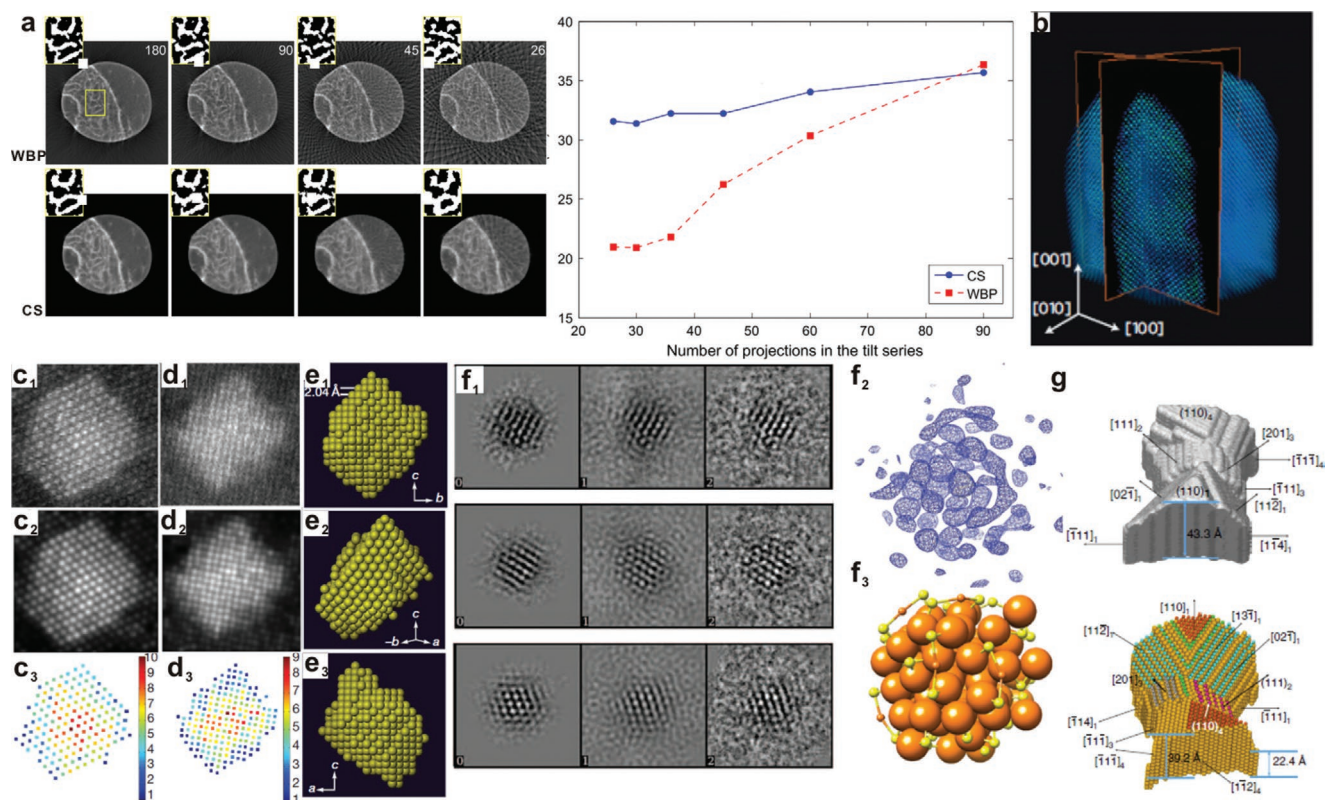


Figure 10. a) Comparison the SNR of tomograms for biological materials reconstructed by CS and WBP algorithms. Reproduced with permission.^[227] Copyright 2016, Elsevier. b) An orthogonal slice view of the atomic-resolution 3D tomogram reconstructed for a gold nanorod by CS-ET. Reproduced with permission.^[225] Copyright 2012, Springer Nature. STEM image, refined model of Ag clusters and number of Ag atoms per column along the c) [101] direction and d) [100] direction, respectively. e) The computed 3D reconstruction of the Ag nanocluster by discrete tomography viewed along three different directions. Reproduced with permission.^[233] Copyright 2011, Springer Nature. f) 3D reconstruction of Au₆₈NP structure by SPT: f₁) left: back projection from the reconstruction; middle: class average of the EM images; right: EM images. f₂) Electron density map. f₃) Au₆₈(SH)₃₂ model. Reproduced with permission.^[238] Copyright 2014 AAAS. g) Surface shape and atomic structure views of the Au[110] sample derived by in-line holography. Reproduced with permission.^[239] Copyright 2016, Springer Nature.

series.^[229–232] It increases the reconstruction fidelity with fewer projections by imposing “discreteness” of an object, which can be a discrete component like atoms or a discrete phase.^[231] A successful example for discrete tomography allows the high-fidelity reconstruction of a gold decahedral nanoparticle from only 15 projections.^[231] Based on aberration-corrected STEM, discrete tomography and statistical parameter estimation theory, the 3D atomic structure of nanosized Ag clusters have been reconstructed from only two HAADF-STEM images (Figure 10c–e).^[233]

Single-Particle Tomography: Apart from those low-dose ET strategies that have all electrons impacting on the same particle, single-particle tomography (SPT) provides another solution for dose-efficient 3D reconstruction by fractionating the required overall electron dose over different particles.^[234] This technique is particularly important for particles with identical structures but projected along diverse directions, from which the low-dose 2D TEM images are collected, aligned, classified, averaged and oriented in 3D space to reconstruct a high-resolution tomogram of the specimen.^[235] SPT serves as an important and widely used low-dose imaging technique in resolving 3D structures of beam-sensitive biological macromolecules, especially united with cryo-EM.^[235–237] Its applications in materials sciences have

recently been explored, particularly in determine the atomic structures of ligand-protected metal clusters.^[238] Figure 10f₁ shows the aberration-corrected TEM images for Au₆₈ particles collected at low dose along different orientations.^[238] The SPT reconstruction provides an atomic-resolution 3D structural elucidation of the Au₆₈ cluster (Figure 10f₂). According to the reconstruction, Au₆₈ cluster is composed of three parts, namely a Au₁₃ cuboctahedron core, an Au₂₄ fcc-like shell and outer Au₃₁ atoms deviated from an fcc packing (Figure 10f₃).^[238]

Low Dose Rate In-Line Holography: The 3D reconstruction can be achieved even from a single projection by in-line holography, which is based on the quantitative interpretation of the electron exit wave reconstructed from focal series of HRTEM images.^[239] The electron exit wave reconstruction has long been adopted to eliminate the impact of point spread functions on phase contrast imaging.^[240] Actually, a single zone-axis projected exit wave of a crystalline particle also contains entire field information and offers the possibility to determine the distance of each atomic column with respect to a common reference plane, which allows the reconstruction of its 3D structure as reported before (e.g., the 3D layered structure and beam-induced structural dynamics of graphene^[241,242]). In particular, this technique is compatible with a wide range of dose rate,

facilitating the application of low-dose-rate in-line holography in beam-sensitive materials.^[243] As an example, the low-dose-rate in-line holography successfully reconstructs the 3D structures of germanium, gold and magnesium oxide particles.^[239] Figure 10g shows the 3D tomogram in surface shape and atomic structure views of dome shaped Au nanocrystal, where diverse nanometer-sized facets, including both high energy and low energy ones, can be clearly observed.

3.4. Strategies Associated with Electron Detection System

3.4.1. Essential Challenges of Electron Detection

The overall performance of an electron detector strongly influences the TEM image quality in terms of both SNR and resolution, and is critically determined by many factors, such as electron dose, signal integration method, beam intensity distribution, and beam exposure mode.^[154] The essential challenges for high-performance electron detection lie in the achievements of high sensitivity, good resolution, good linearity, large dynamic range, and high speed. In general, the sensitivity of the detector depends on its DQE, which may be dose-rate-dependent, and determined by the electron detection mechanism and the detector architecture.^[244] The detector performance is also determined by its point-spread function (PSF), which should be as narrow as possible to ensure the highest modulation transfer function (MTF) near the resolution limit.^[245,246] On the other hand, detector linearity and dynamic range should be optimized to guarantee a linear electron-signal relationship over a wide range of beam current densities.^[247] The detector speed relies on the capabilities of its data handling and transfer architecture, which becomes crucial for accurate specimen-motion correction,^[248] as introduced in Section 3.4.2.

Traditional image recording systems include photographic film, image plates and scintillator-based CCD cameras. Both films and image plates have small pixels (film) or the good linearity (image plates).^[54] However, they require extensive post-processing procedures and do not allow real-time imaging. Since the 1980s, CCD-based cameras have been introduced into electron microscopy, offering the possibility of real-time readout.^[249,250] To avoid damage from direct exposure to high-energy electrons, CCD-based cameras usually incorporate a scintillator, which entails a signal conversion from electrons to photons that are transmitted through fiber optics or lens coupling, and then to electronic signals for readout (Figure 11a,b).^[244] Both the scintillator and the fiber optics (or lens) scatter the electrons and photons, which contributes to the PSF and degrades the detector performance.^[244] The SNR of low-dose TEM images rendered by CCD cameras is actually restricted by PSF effects and the relatively high readout noise. In addition, the charges in slow-scan CCD cameras have to be transferred row by row into a serial register and readout pixel by pixel. This limits the readout speed of slow-scan CCD cameras and restricts their applications in accurate specimen motion correction. In general, advances in the low-dose imaging of beam-sensitive materials lie in the revolutionary electron detection technologies.

3.4.2. Direct-Detection Cameras

Recently, the invention of direct detection cameras (DDC) has led to a significant breakthrough in the field of low-dose electron microscopy. Such cameras use a simple direct electron detection method instead of the complex electron-to-photon-to-signal detection mechanism.^[244] This effectively eliminates the noises arising from the signal conversion and transmission, and greatly enhances the DQE as shown in Figure 11e.^[214,244] The DDC uses an imaging sensor (Si) to receive the electrons that are deposited onto the top-layer and then directly convert to an electronic signal for readout (Figure 11c,d).^[244] The use of silicon reduces the PSF, which is larger in the conventional CCD detector with phosphor scintillators, and thus improves the resolution.^[244] The new-generation DDC is a back-thinned CMOS detector, enabling a dramatic decrease of electron back-scattering from the sensor to the active layer (Figure 11d), and therefore further improving the PSF.^[244] Moreover, the electron counting mode in DDCs further minimizes the electron scattering noise in the Si sensor and the readout noise, and thus offer improved DQE for low-dose applications.^[244] Figure 11f,g compares core-loss EFTEM images collected on CCD and DDC and the latter exhibits a much higher SNR.^[251]

An important low-dose application enabled by DDC is the accurate correction of beam-induced specimen motion through fast exposure and diverse motion-correction algorithms. Such motion is often unavoidable during image acquisition, which severely damps the high-frequency spatial information. Notably, for low-dose imaging, each image frame with an exposure time short enough to capture specimen motion suffers from an extremely low SNR under a frame dose in the range of 0.01–0.025 electrons per pixel.^[246] This fact hinders the direct utilization of traditional motion-correction algorithms, such as cross-correlation (CC) or phase-correlation (PC) algorithms.^[252] Taking the CC algorithm as an example, an accurate motion correction requires the precise determination of the CC peak between neighboring image frames. This algorithm is however compromised by the largely weakened and broadened CC peak caused by the insufficient frame dose. Practically, a lower limit of frame dose for a successful motion correction via CC has been reported to be around ≈ 0.8 counts per pixel^[248] (approximately $\approx 2 \text{ e}^- \text{Å}^{-2}$ for an average detector conversion efficiency of 80% and a pixel size of 0.71 Å at a 44 000 \times magnification), which is far beyond the typical frame dose used for imaging very beam-sensitive materials.^[34,35] By employing a recently developed “amplitude filter” that filters out weak pixels of the FT amplitude components,^[34] motion correction of highly noisy image frames is readily accessible.

Another important application for DDC is low-dose EM imaging, beginning from biological specimens. Cheng and Juliu successfully determined the 3D structure of 700 kDa archaeal 20S proteasome with D7 symmetry at a resolution of 3.3 Å using cryo-EM and a DDC operated in electron counting mode.^[214] In addition, they also successfully determined the structure of a mammalian transient receptor potential channel TRPV1 at a resolution of 3.4 Å, which plays an important role in pain physiology.^[253] Recent advances in structural biology that combine cryo-EM and DDC even breaks the 1.8 Å resolution barrier.^[17]

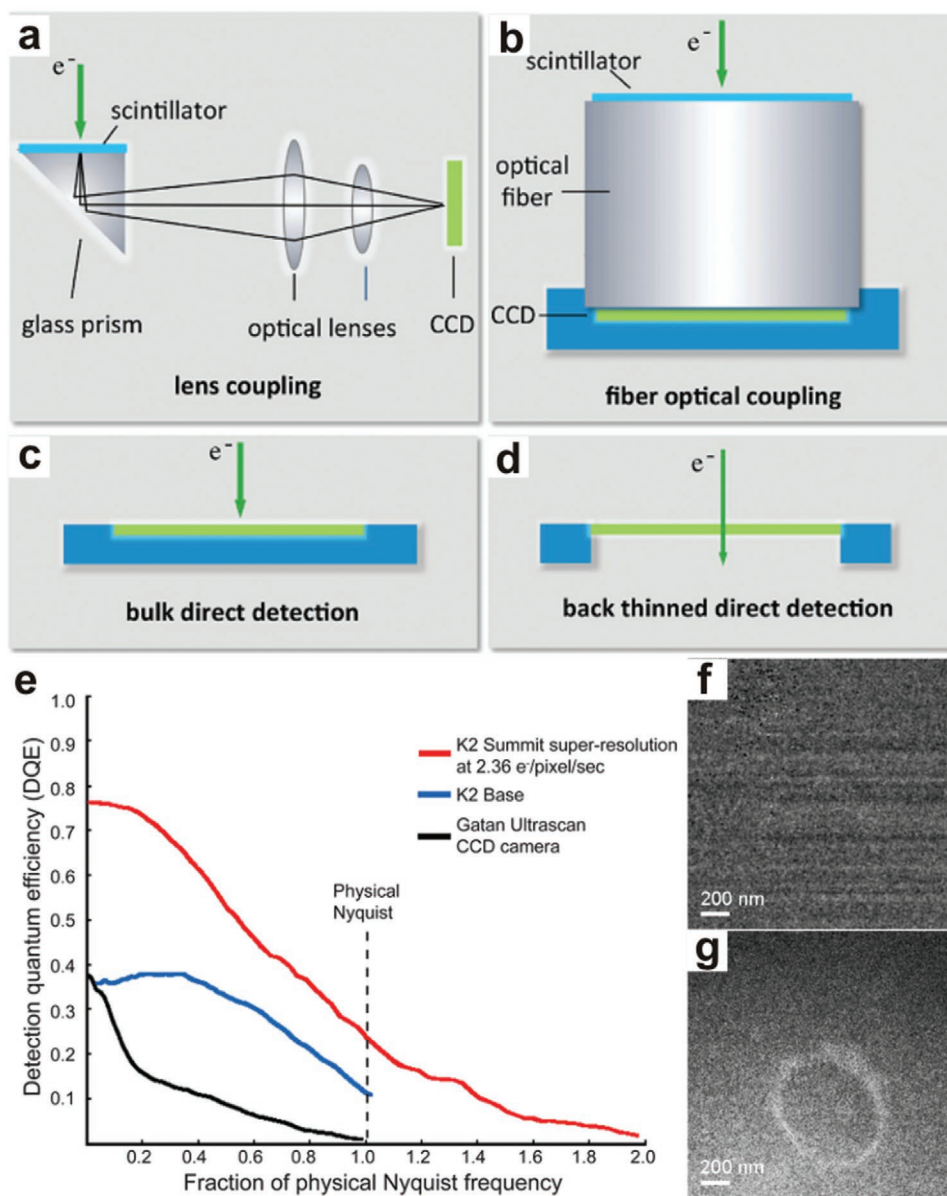


Figure 11. A comparison of detector architectures among CCD cameras and DDCs. a) Lens coupled CCD. b) Fiber optical coupled CCD. c) First generation bulk DDC. d) Second generation back-thinned DDC. Reproduced with permission.^[244] Copyright 2013, Cambridge University Press. e) The comparison of DQE curves of a typical CCD camera versus DDC. Reproduced with permission.^[214] Copyright 2013, Springer Nature. The comparison of the Ce elemental map based on the two cerium pre-edges and a cerium postedge acquired on the f) Ultrascan 4000 and g) DE-12, respectively. Reproduced with permission.^[251] Copyright 2014, Cambridge University Press.

The DDC was applied in the field of low-dose EM imaging of materials science samples only recently. Diverse nanostructures have been revealed with high-resolution, such as $\text{g-CN}_x\text{H}_y$,^[254] CeO_2 cubes with oxygen surface dynamics,^[255] and short-range ordered materials (allophane).^[256] MOFs belong to a representative category of beam-sensitive materials that can only be imaged at high resolution using a DDC rather than a conventional CCD/CMOS camera. Most MOFs structures are extremely vulnerable to electron beam irradiation and usually have a very small cumulative critical dose of $15\text{--}30\text{ e}^- \text{ \AA}^{-2}$ or even lower.^[35,213] Most structural studies on MOFs are traditionally based on X-ray crystallography, which resolve the

periodically averaged structural information but lose the local structural information. By employing a DDC, one can retrieve both long-range ordered and local structural information (e.g., surfaces, interfaces, defects, and disorder) at atomic resolution, even under low electron doses.^[34,35] Detailed examples are introduced in Section 4.

3.4.3. Segmented Detectors

Recent developments in STEM detectors also strongly benefit the low dose imaging of beam sensitive materials. In STEM,

a highly focused probe is raster-scanned across the specimen. The scattered electrons are collected in diffraction plane by STEM detector.^[52] In order to complete millions of scanning points within a few seconds, scintillator/photomultiplier tubes (PMTs) are used for fast readout.^[257] The electrons strike the scintillator and the resulting photons are transferred into the PMT and output as an electronic pulse.^[258]

Disk-shaped bright-field (BF) detectors are used to collect low-angle scattered electrons to form phase-contrast images.^[52] Annular dark-field (ADF) STEM detectors collect the high-angle scattered electrons to form Z-contrast images.^[259] As shown in the green area of **Figure 12a**, the position of the ADF detector is outside the illumination cone of the focused electron beam. The ADF can be further categorized into high-angle ADF (HAADF), medium-angle ADF (MAADF) and low-angle ADF (LAADF).^[260] HAADF signals are dominated by Rutherford scattering and thermal diffuse scattering, which are sensitive to heavy elements.^[261] Annular bright-field (ABF) detectors with a solid disc shape, on the other hand, is located inside the illumination cone of the focused electron beam (Figure 12a). An effective ABF detector, which can be achieved by adjusting the camera length so the center diffraction disk just falls on a conventional ADF detector, hybridizes phase-contrast and allows the imaging of light elements, even the H and Li atomic columns.^[262–264]

For the STEM imaging with either a BF, ABF, or ADF detector, the signal consists of scattered electrons integrated over a rotationally symmetric portion of the diffraction plane. In such cases, only a fraction of the scattered electrons is utilized to form the image. Moreover, some useful information about the specimen, which is encoded in the azimuthal distribution of scattered electrons, is lost. Thus, the overall dose efficiency of BF-, ABF-, or ADF-STEM can be low. In addition to those STEM detectors with rotation symmetry, segmented detectors have been developed. Shibata et al. developed such a segmented STEM detector that has the same size as a conventional detector and consists of 16 annular quadrants (Figure 12b), each coupled to a dedicated PMT.^[266] The segmented detector collects almost full range of the scattered electrons and records their spatial distributions. Segmented detectors can realize different imaging modes via a combination of images acquired from different segmented channels, which thus offer dose efficiency and versatility.^[266]

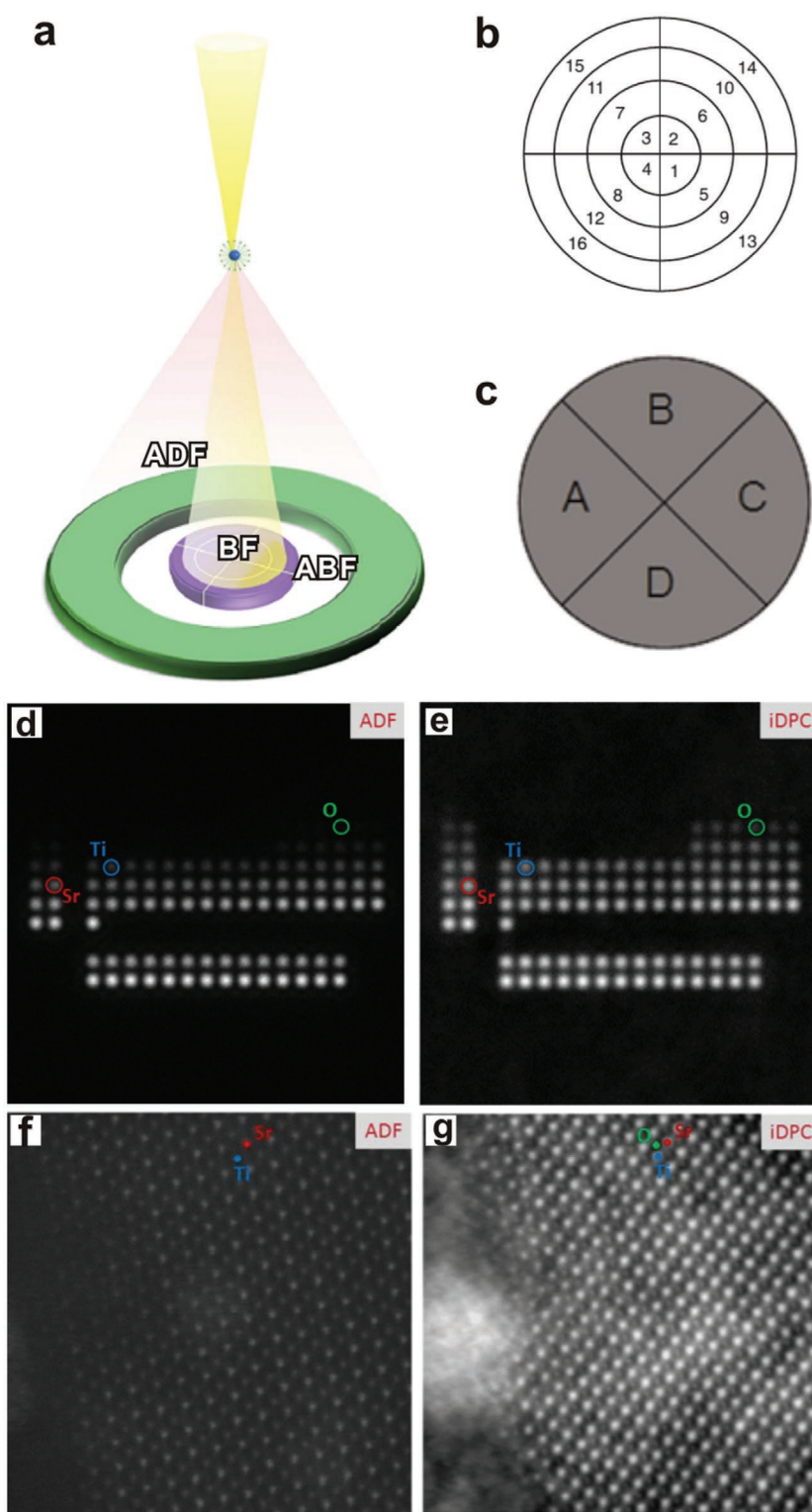


Figure 12. Schematic illustration of a) ADF, BF, and ABF. Reproduced with permission.^[265] Copyright 2017, Springer Nature. b) Four-ring 16-segmented DPC and c) full quadrant DPC configurations for STEM imaging. b) Reproduced with permission.^[266] Copyright 2010, Oxford University Press. c) Reproduced with permission.^[267] Copyright 2015, Elsevier. Simulated ADF d) and iDPC contrast e) of elements in the periodic table. ADF-STEM image f) and iDPC-STEM image g) of SrTiO₃ recorded under the same imaging conditions. Reproduced with permission.^[268] Copyright 2016, Cambridge University Press.

A recently developed dose-efficient STEM imaging technique based on segmented detectors is called integrated differential phase-contrast (iDPC)-STEM. It makes use of the electron scattering distribution within the detector pattern and enables the simultaneous imaging of both light and heavy elements across the periodic table with relatively low total dose (Figure 12d,e).^[268,269] By combining the four quadrant signals with differential operations (Figure 12c), iDPC enables the possibility on a thin specimen to reconstruct the phase image which is representative of the (projected) electrostatic potential and thus directly interpretable.^[267] Figure 12f–g shows the STEM images of SrTiO₃ obtained by conventional ADF-STEM technique and iDPC-STEM technique, respectively.^[268] The oxygen columns and carbon contamination are clearly observed from iDPC-STEM images rather than ADF-STEM image, indicating the advantage of imaging low-Z elements in the iDPC-STEM mode. Moreover, iDPC-STEM is also widely used for low-dose (rate) imaging. Carlsson et al. successfully imaged Li in LiTi₂O₄ and LiNi_{0.5}Mn_{1.5}O₄ using iDPC-STEM with an electron beam current as low as a few pA.^[269] iDPC-STEM has also been shown to decrease the dose rate for atomic-resolution imaging of a zeolite by a factor of five.^[270] Additionally, iDPC-STEM technique is quite sensitive and can be used to map the strain fields,^[271] electric fields,^[265] and electromagnetic fields.^[257]

3.4.4. Pixelated detector

As a special type of segmented detectors, pixelated detectors provide an ultimate detector form for STEM imaging that incorporates the full range of reciprocal space information. Such detectors enable a versatile 4D-STEM imaging mode, which is comprised of full diffraction (i.e., CBED) patterns, containing important information on the crystal structure,^[272] chemical composition,^[273] electric fields,^[274] defects/disorder,^[275] and strains,^[276–278] etc., for each probe position (Figure 13).^[267,279,280]

As a representative 4D-STEM technique using a pixelated detector, electron ptychography or ptychographic diffractive imaging records a full set of diffraction patterns from multiple probe positions, which allows post-acquisition aberration-correction and quantitative phase retrieval of the exit wavefunction from the overlap regions of diffraction disks (colored area in Figure 13a) where the diffracted beams interferes coherently.^[281] This process does not require a priori knowledge about the probe function and overcomes the drawbacks of electron coherent diffractive imaging (CDI),^[282] by eliminating the problems of nonunique solutions and a limited field of view. As proposed by Rodenburg et al.,^[2] electron ptychography is usually conducted with large sampling redundancy in the probe positions, followed a phase retrieval algorithm such as the extend ptychographic iterative engine (ePIE),^[283] difference map (DM),^[282,284] hybrid input–output (HIO)^[285] or Fourier-based direct algorithms.^[157,286] Electron ptychography enables the recovery of structural information for both heavy and light elements in three-dimensions and at atomic resolution.^[272,281,287–289] Typical pixelated detectors, including monolithic active pixel sensors (MAPS) and hybrid pixel array detectors (PADs),^[290] are both high throughput and suitable for ptychographic applications.

The MAPS is made up by sensor and readout electronics in a single layer.^[290] While the PADs have a thick diode sensor layer and silicon readout electronics chip layer as schematically illustrated in Figure 13b.^[290] The PADs can achieve a 1.1 kHz frame rate and single electron sensitivity, which enables rapid and sensitive signal collection and specimen drift minimization.^[290] The ptychographically reconstructed image has improved contrast transfer and better overall SNR than DPC or ABF/ADF,^[267] even under low dose conditions.^[291] This point can be further improved once a pixelated detector has higher sensitivity and dynamic range, because those weak signals at high scattering angles that contain high-resolution information are collected with higher SNR.^[292] Sagawa et al. developed a pixelated STEM detector coupled with a direct electron CCD image sensor under the ADF detector, allowing the simultaneous collection of ADF-STEM images and 4D datasets under low-dose conditions.^[293] Figure 13c,d compares the ADF-STEM image and the ptychographically reconstructed phase image of an SWCNT, showing the advantages of the ptychographically reconstructed phase image with much higher image contrast and SNR.^[293] Muller and co-workers reported a new type of electron microscopy pixel-array detector (EMPAD) that allows deep sub-Ångström resolution and significantly improved contrast for imaging point defects in 2D materials.^[294] An alternative low-dose ptychography strategy is to use a defocused scanning probe, which allows post-acquisition focusing and effectively overcomes the problems associated with long acquisition, high dose, specimen drift and unmanageable volume of data via only a few tens of highly overlapped probe positions, to achieve atomic-resolution ptychographic reconstruction.^[292,295] Wang and co-workers carried out low-dose ptychography on MoS₂ using a direct detection camera and such a defocused probe.^[296] In addition, a new design of hollow pixelated detector that allows simultaneous ptychographic phase-retrieval and electron-energy-loss spectroscopy (EELS) analysis has recently been proposed.^[297]

Another dose-efficient imaging technique involving a pixelated detector is STEM imaging with “matched-illumination-and-detector-interferometry” (MIDI-STEM).^[298] It integrates prespecimen phase gratings, aberration correction, a direct detection pixelated detector, and postacquisition phase retrieval to reconstruct phase-contrast images with almost ideal linear contrast transfer over a wide range of spatial frequencies (Figure 13f).^[298] Specifically, a phase plate fabricated with alternating concentric trenches is placed at the probe-forming aperture position to introduce a 0 or $\pi/2$ phase modulation of the incident electron beam.^[298] The transmitted central beam at each probe position is then recorded via a direct detection pixelated camera, which is further fitted to a virtual detector according to the geometry of the phase plate to produce a linear phase contrast image.^[298] MIDI-STEM provides a dose-efficient imaging solution with much enhanced contrast transfer at low spatial frequencies compared to ABF-STEM, DPC-STEM and even ptychographic 4D-STEM, and thus is an ideal tool for imaging low and high atomic numbers simultaneously (Figure 13g–i).^[298] The suppressed low-frequency contrast transfer of ptychographic 4D-STEM originates from the completely destructive interference of diffracted beam in the “triple-overlap” regions that generally have no phase information and appear at low spatial frequency along with zero aberrations. At

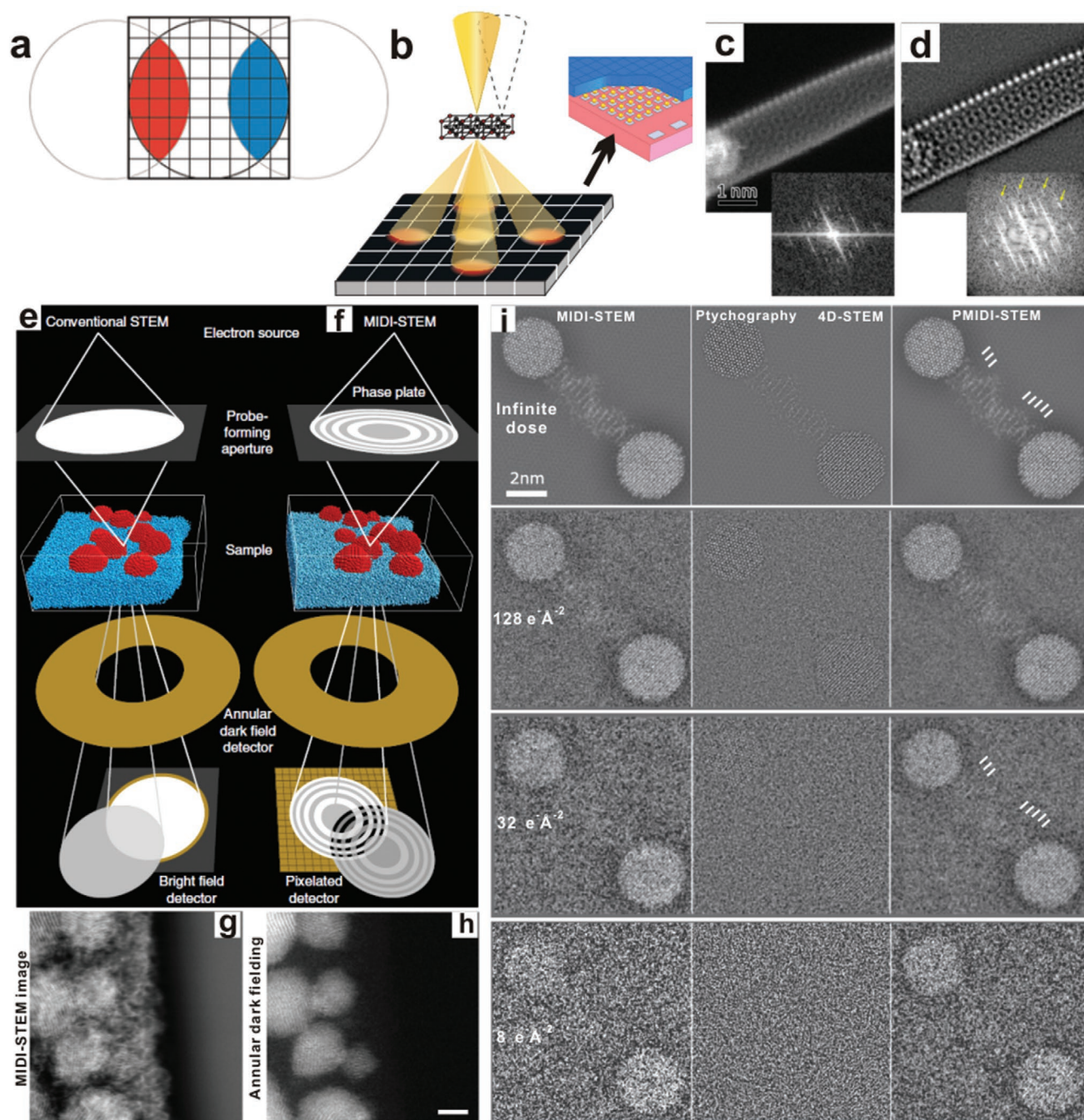


Figure 13. a) The interference between the scattered and unscattered discs and the selective signal recording over detector pixels. Reproduced with permission.^[267] Copyright 2015, Elsevier. b) Schematic illustration of STEM imaging using a pixelated detector. Reproduced with permission.^[290] Copyright 2016, Cambridge University Press. Comparison between c) an ADF-STEM image and d) a ptychographically reconstructed phase image of an SWCNT. Reproduced with permission.^[293] Copyright 2018, Cambridge University Press. e) Conventional STEM setup, with a round probe-forming aperture and monolithic, single-pixel ADF and BF detectors below the sample. f) MIDI-STEM setup, with a patterned phase plate placed in the probe-forming aperture and a pixelated detector below the sample. STEM image obtained using g) MIDI-STEM and h) ADF-STEM setups. Reproduced with permission.^[298] Copyright 2016, Springer Nature. i) STEM images obtained by MIDI-STEM, ptychography, and PMIDI-STEM imaging modes under different doses. Reproduced with permission.^[157] Copyright 2016, Elsevier.

higher spatial frequency, however, only “double-overlap” regions appear, from which the phase information could readily be extracted to ensure the phase contrast transfer function (pCTF) for ptychographic 4D-STEM approximately twice as high as

MIDI-STEM.^[267] There are two strategies to further enhance the low-frequency contrast transfer of ptychographic 4D-STEM so as to enhance the interference in the “triple-overlap” regions: i) to introduce a phase ramp by aberrations (e.g., defocus)

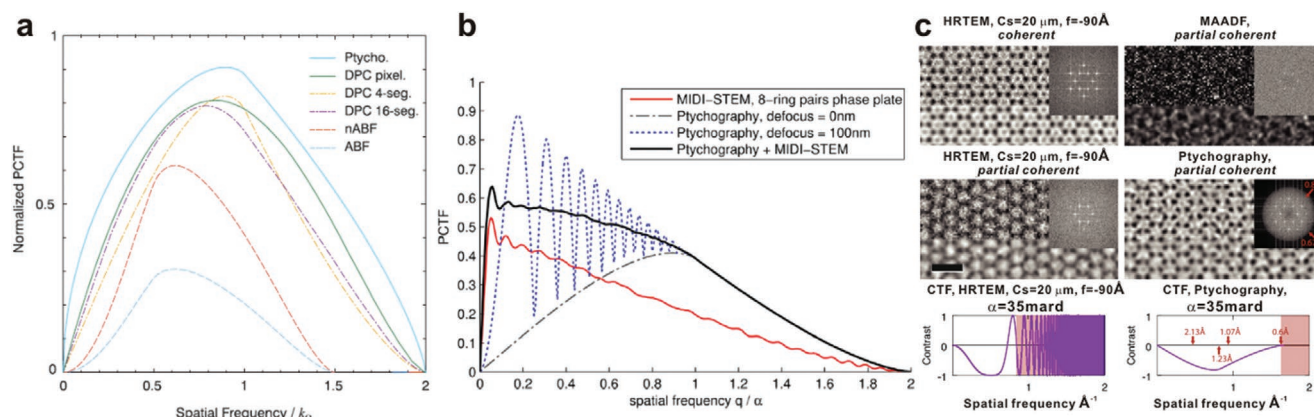


Figure 14. a) Plot of pCTFs curves normalized by the noise level versus spatial frequency for ptychography (Ptycho), DPC by a pixelated detector (DPC pixel), DPC by a quadrant detector (DPC 4-seg), DPC by the 16-segment detector (DPC 16-seg), normalized ABF (nABF) and non-normalized ABF (ABF). Reproduced with permission.^[299] Copyright 2018, Elsevier. b) The pCTF curves of PMIDI-STEM with an eight-ring pairs phase plate (black solid line), MIDI-STEM with the same phase plate (red solid line), in-focus (dash-dot line) and defocus (dotted line) ptychography respectively. Reproduced with permission.^[157] Copyright 2016, Elsevier. c) Simulated HRTEM, MAADF and ptychography images of graphene at 80 kV under coherent and partial coherent conditions along with a dose of 20 000 e \AA^{-2} . Reproduced with permission.^[300] Copyright 2019, Elsevier.

and ii) to introduce a phase shift by the prespecimen phase plate. The former strategy, termed as defocused ptychographic 4D-STEM, greatly enhances the low-frequency contrast transfer but results in large oscillations in the pCTF due to the defocus effects.^[296] The latter strategy, termed as ptychographic MIDI-STEM (PMIDI-STEM), combines the advantages of both electron ptychography and MIDI-STEM toward an enhanced and linear pCTF, which provides a more robust solution for a wide range of low-dose STEM applications.^[157]

An immediate question arises regarding to the dose efficiency among the diverse EM imaging techniques discussed above. Seki et al. systematically compared the dose efficiency among multiple STEM-based low-dose imaging techniques via pCTF by including the noise effects.^[299] As shown in Figure 14a, the results indicate that the maximized pCTF of ABF by introducing aberrations can be further enhanced by normalizing the total electron counts.^[299] DPC imaging modes with various detectors generally have more efficient contrast transfer than ABF, and their pCTF increases in the order of quadrant, 16-segmented and pixelated detectors.^[267] Ptychography has overall best dose efficiency among these techniques.^[299] Yang et al. proposed that the ptychographic reconstruction of signals from DPC detectors provides better image SNR than the difference DPC signals, while the dose efficiency critically depends on the detector geometries (i.e., a 4-ring/16-segment geometry is less efficient than a 4×4 array/16-pixel geometry).^[267] Moreover, Ophus and co-workers include the effect from prespecimen phase plate,^[157] which suggests that PMIDI- and MIDI-STEM imaging modes outperform other techniques in terms of the pCTF over the whole spatial frequency due to their approximately linear phase transfer (Figure 14b). Pennycook et al.^[300] further compared the dose efficiency of ptychographic phase contrast imaging with conventional HRTEM (Figure 14c). They concluded that the former technique has better dose efficiency under partial coherent imaging conditions. The reason lies in the fact that the temporal incoherence and lens fluctuations in HRTEM will lead to defocus spread and further reduce the

image quality.^[300] STEM ptychography benefits from directly interpretable image, “double resolution” and reduced temporal incoherence effects arising from achromatic lines in the double disk overlap regions.^[300]

In practice, selecting the optimum EM technique and condition for imaging beam-sensitive materials is more complicated and requires the extensive consideration of the following issues: i) the dose-rate effects (i.e., linear, direct or inverse effects), which is important for selecting imaging modes (TEM, STEM, or UEM) and beam current density; ii) the dominant beam damage mechanism (i.e., knock-on, radiolysis or other secondary/tertiary processes), which determines the employed electron energy, imaging modes and specimen treatments; iii) the structure of the specimen (i.e., crystallinity or inter-particle structural equivalence), which is associated with the preimaging operations (e.g., zone-axis alignment) and structure determination strategies (e.g., SPT method); iv) the electron detector performance (i.e., sensitivity, resolution, dynamic range, and speed), which is closely related with the imaging modes, image acquisition strategies (e.g., direct imaging or diffractive imaging), and postacquisition data processing.

4. Materials Science Applications and Discoveries

4.1. The Emerging Need for Imaging Beam-Sensitive Materials

The significant advances in diverse fields of materials science over the past few years have largely extended the target materials to more hierarchical, lower-dimensional or less-stable systems, as pioneered by the discovery and synthesis of single atom catalysts,^[301] microporous materials (e.g., MOFs/COFs/zeolites),^[302–304] 2D materials^[305] and organic–inorganic hybrid materials.^[306] Because most of these materials feature either weak chemical bonds, ultrasmall dimensions or fragile porous network, they are highly vulnerable to electron beam irradiation and thus excluded for conventional EM imaging.^[34,35,37,128]

The explicit structure–property relationship of these materials spanning multiscales and multidimensions would be necessary to inspire new structural designs so as to adapt diverse materials science applications. Accordingly, there is undoubtedly an emerging need for involving the leading technologies and methodologies to image beam-sensitive materials.

4.2. Crystal Structure elucidation

Crystal structure elucidation is one of the most fundamental problems for all crystalline materials. Generally, crystallographic methods based on either X-ray, neutron or electron are used to determine the spatially averaged periodic structures of crystalline materials through diffraction, which basically focuses on solving the crystallographic “inversion problem.”^[307,308] To be specific, the crystal structure elucidation utilizes the recorded amplitudes of structure factors (i.e., how much matter is scattered) to determine the phases of structure factors (i.e., where the matter locates).^[309] However, traditional X-ray crystallographic methods have poor spatial resolution and practically very challenging to implement for polycrystalline samples due to severe reflection overlapping problem.^[310] Electron diffraction is able to probe individual nanocrystals with a much better spatial resolution, but often suffers from dynamical effects.^[311,312] On the other hand, electron microscopy enables the direct structural elucidation in real space and at atomic resolution, and allows both site-specific crystallographic (e.g., via lattice-averaging and motif-averaging techniques^[34,35,313]) and microscopic approaches for structural study. A significant restriction lies in its high electron dose (typically 10^3 – 10^4 e \AA^{-2} ^[314]) required for high-resolution imaging, which is actually far beyond the critical doses of most beam-sensitive materials.^[34,35]

Microporous materials, such as zeolites, COFs, and MOFs, usually exhibit excellent gas adsorption and separation, catalysis and ion exchange properties.^[315–318] However, most microporous materials are highly vulnerable to electron beam irradiation,^[34,35,128] which results in a large barrier for determining their atomic-scale structure–property relationships. A significant amount of microporous materials has their respective damage mechanisms dominated by radiolysis,^[128] an effective EM imaging strategy would thus be low-dose imaging. Actually, early developments associated with HRTEM imaging and structural elucidation of beam-sensitive microporous crystalline materials are pioneered by researchers such as Zou’s and Terasaki’s groups, including essential developments in low-dose HRTEM imaging techniques and associated digital image processing methods.^[319–322] On the other hand, Bubán et al. pioneered in probing for STEM imaging parameters that would satisfy the requirements for the imaging beam-sensitive materials.^[323] Up to now, the low-dose imaging of microporous materials like zeolites has been extended to the less dose-efficient Cs-corrected ADF-STEM imaging in several case studies.^[128,324] For example, the ETS-10 zeolite that belongs to the family of titanosilicates and consists of corner-sharing TiO_6 octahedra and SiO_4 tetrahedra can be imaged along the [110] direction by ADF-STEM as shown in **Figure 15a**, which matches well with the superimposed structural models and corresponding

simulations respectively (**Figure 15b–d**).^[324] By using the recently developed iDPC-STEM as a more dose-efficient EM technique, researchers are able to directly observe the atomic-resolution structural projection of ZSM-5 zeolite along the [010] direction (**Figure 15e–g**), where the projected microporous network composed of ten-ring channels surrounded by five and six rings and individual T sites can explicitly identified.^[269,270] iDPC-STEM allows the reconstruction of directly interpretable phase image that correlates the projected potentials and probes a wide range of different elements.^[268] Provided the important fundamental and industrial applications of zeolites,^[325,326] many challenging but significant structural features in zeolites, such as individual dopants or (in-channel) adsorbates, could be unraveled by the low-dose iDPC-STEM technique.^[327,328]

The DDC and associated low-dose HRTEM imaging methodology provide another strategy for resolving the crystal structures of beam-sensitive microporous materials. In contrast to the low-dose STEM strategy, the low-dose HRTEM strategy coupled with DDC would benefit for a wide range of materials with a direct or linear dose-rate effect and require a much lower cumulative dose to form a quality image. Hence, it is more suitable for imaging extremely beam-sensitive materials with very small critical doses, such as MOFs and COFs.^[29,34,35] As an example, Zhu et al. reported the atomic-resolution HRTEM imaging of a MOF crystal ZIF-8 under a total dose as low as 4.1 e \AA^{-2} , by using a noncorrected electron microscope equipped with a DDC operated in counting mode. As shown in the HRTEM image of ZIF-8 along [111] direction (**Figure 16a,b**), it is observed that the Zn atomic columns are arranged in a group of three while the organic linkers are arranged in edge-on and face-on configurations.^[35] Zhang et al. carried out an atomic-resolution EM study on the crystal structures of a UiO-66 MOF using a similar low-dose imaging strategy.^[34] Different types of projected Zr atomic columns within the Zr_6O_8 clusters are clearly identified while even the benzene rings in the organic linkers are unambiguously resolved with a face-on configuration (**Figure 16c,d**). Recently, Li et al. reported the direct imaging of MIL-101 MOF at atomic level and a total dose of ≈ 8 e \AA^{-2} by DDC. The highly ordered stacking of medium cages and connections of the surrounding supertetrahedrons can be directly observed from the triangular and pentagonal patterns, even though there are more than 5000 atoms in a single unit cell of MIL-101.^[137] Although many MOFs have readily resolvable structures by single-crystal crystallography or in a few cases by polycrystalline crystallography,^[329] DDC-HRTEM provides a general structure determination solution for MOFs via direct imaging in real-space, especially for those with insufficient crystal qualities for crystallography. Notably, freezing the specimen further increases the beam durability and critical dose for these materials, which could largely mitigate the low SNR issue in low-dose imaging as recently reported in a case study of ZIF-8 crystals.^[49]

Unlike MOFs, the structure determination for a wide range of COFs is more difficult because COFs are usually not well crystallized and suffer from severe overlapping and broadening issues of reflections by polycrystalline X-ray crystallography. The problem becomes more significant for low-dimensional COFs when reflection intensities are further modulated by preferred orientations.^[29] Peng et al. reveal through DDC-HRTEM

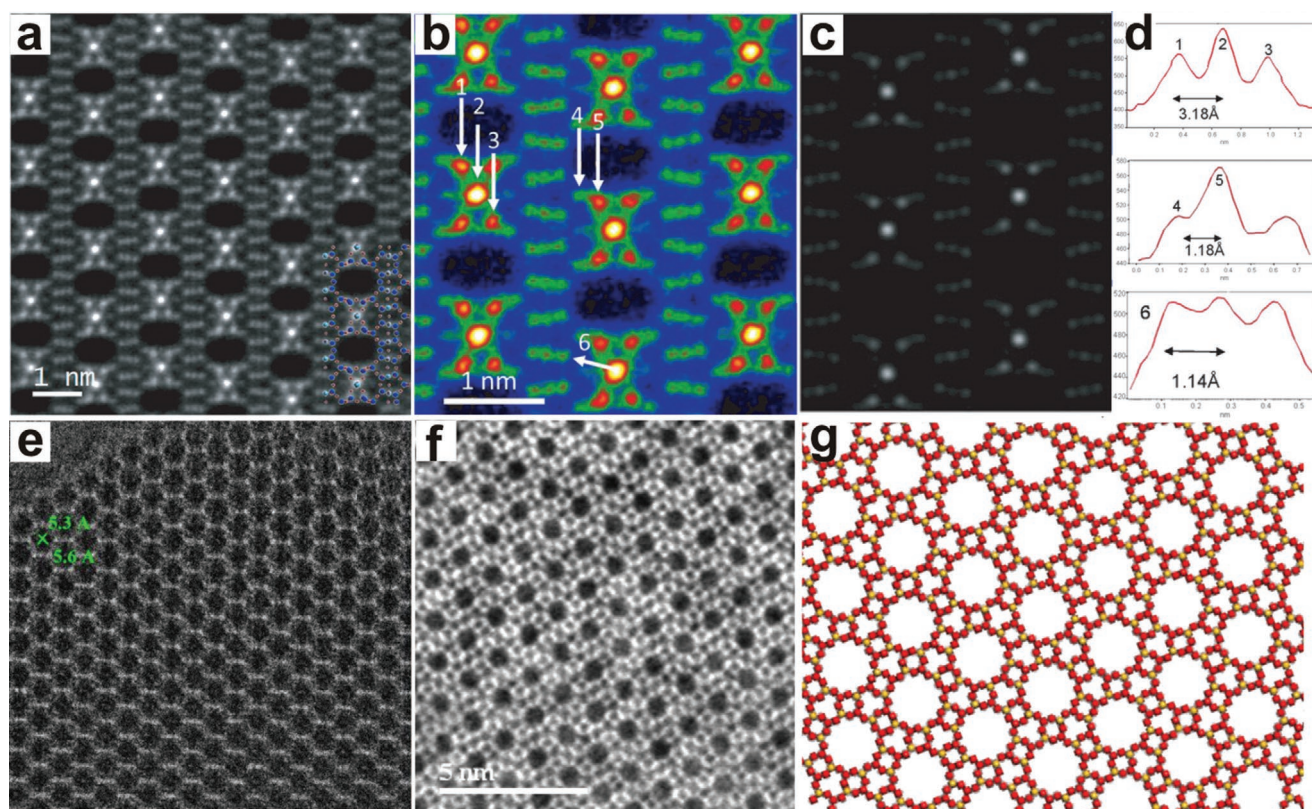


Figure 15. The low-dose STEM imaging of zeolites using single-pixel and segmented electron detectors. a) HAADF-STEM image, b) the thermal color map, and c) simulated image of EST-10 along the [110] direction. d) The line profiles of the region that marked in (b). Reproduced with permission.^[324] Copyright 2013, Wiley-VCH. e) ADF-STEM image acquired with a dose rate of less than $10 \text{ e}^- \text{Å}^{-2} \text{s}^{-1}$, f) iDPC-STEM image acquired with dose of $260 \text{ e}^- \text{Å}^{-2}$, and g) structural projection of Zeolite ZSM-5 along [010] direction. Adapted with permission.^[270] Copyright 2018, Cambridge University Press.

imaging the pore architecture and individual molecular building units for 2D TPA-COF nanosheets made of TAPA (tris(4-aminophenyl)amine) and TFPA (tris(4-formylphenyl)amine) molecules as precursors (Figure 16e–g).^[29] The ultrathin 2D COF nanosheets work as a highly sensitive and selective fluorescence sensing platform for DNA molecules (Figure 16h,i), where the imaging results provide a solid basis for the structure determination and structure–property relationship study.

2D materials, as another category of beam-sensitive materials, feature superior electronic, optical, magnetic and mechanical properties in contrast to their bulk counterpart, and thus have promising applications in many fields such as electronics, photonics, magnetic devices, sensing and catalysis.^[330–333] A straightforward way to elucidate their atomic structures is direct EM imaging, which is however nontrivial due to the fact that 2D materials are usually vulnerable to the irradiation of high-energy electron beam.^[45,172] Practical solutions for imaging 2D materials usually include low-kV imaging that eases knock-on damage,^[162] and low dose (rate) imaging that minimizes overall beam damages.^[57] Low-kV strategy is widely used in imaging various 2D materials,^[334,335] e.g., graphene, with electron energy well below its knock-on threshold energy. On the other hand, by combining the pixelated detector and defocused probe electron ptychography techniques, atomic resolution phase images of single layer MoS_2 have been successfully obtained under different electron doses as shown in Figure 17a–d.^[296]

Generally, electron ptychography outperform HAADF-STEM in terms of both SNR and contrast for “low-Z” elements by clearly resolving Mo and 2S atomic columns even with a lower cumulative dose. As another low dose-rate imaging strategy for crystal structure elucidation, Yu et al. have successfully resolved the atomic structure of ultrathin 2D CsPbBr_3 halide perovskites by combining aberration-corrected HRTEM with exit-wave reconstruction with low dose-rate in-line holography, without causing considerable electron beam damage (Figure 17e–g).^[37]

The chemical synthesis and structure elucidation of materials associated with energy conversion have attracted great attentions due to their wide applications associated with renewable and portable energy sources.^[336] As an example, the problem associated with the Li-containing electrode materials is very important for LIB as the leading energy conversion technology, where the Li-containing structures (e.g., Li dendrites) are usually very beam-sensitive and difficult to be directly imaged by TEM.^[19] This becomes even more challenging once the complicated structural dynamics during charging and discharging processes was considered, where Li dendrites are generally undesirable and their formation mechanisms need to be resolved.^[19] In principle, the Li dendrites could suffer from a combination of knock-on and radiolysis damage,^[337,338] of which the latter could be minimized by freezing the specimen. As a representative work, Li et al. successfully applied cryo-EM to reveal the atomic structure and growth directions of

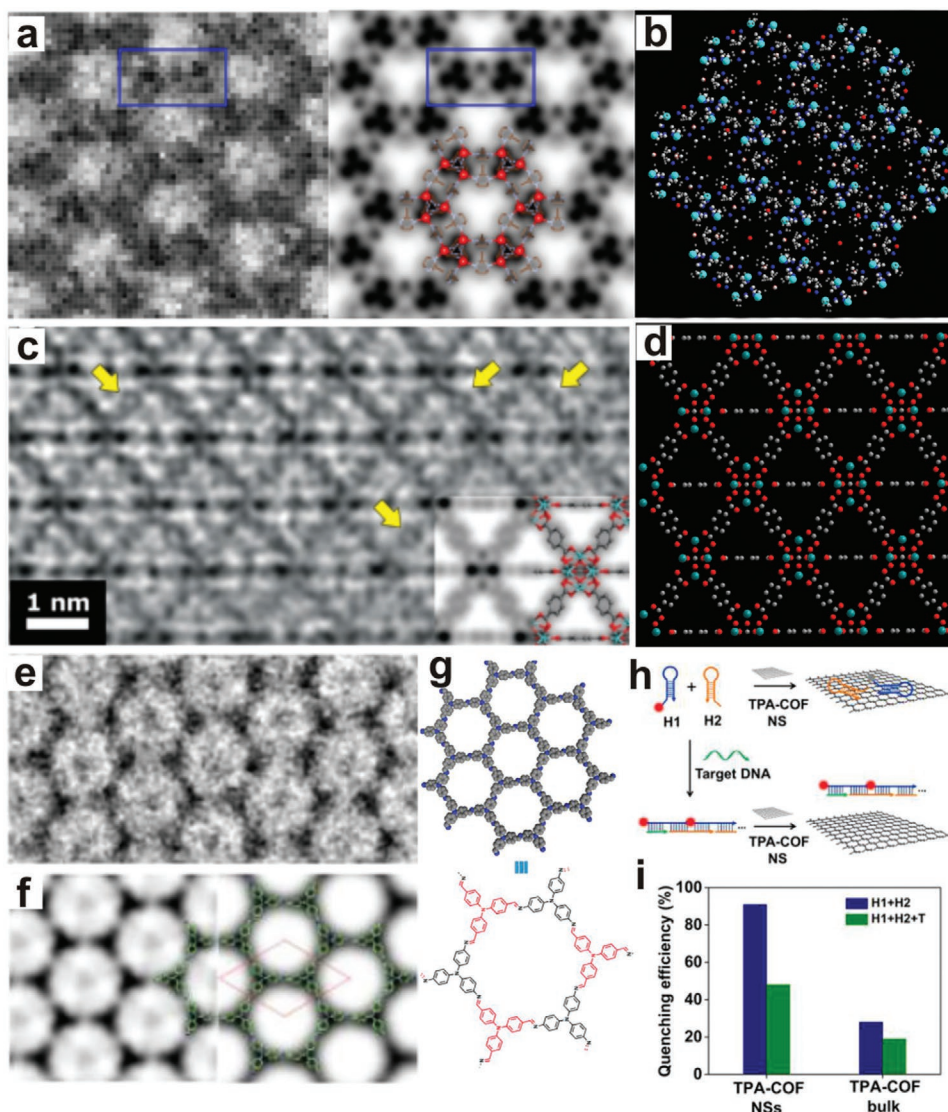


Figure 16. Low-dose HRTEM imaging of MOFs and COFs by DDC. a) The CTF-corrected and denoised, the symmetry-imposed and lattice-averaged images (model embedded) and b) structural projection of ZIF-8 crystals along [111] direction acquired with a dose of $4.1 \text{ e}^- \text{ \AA}^{-2}$. Reproduced with permission.^[35] Copyright 2017, Springer Nature. c) The CTF-corrected and denoised image of UiO-66 crystal (potential and model embedded) and d) structural model along [110] direction. Reproduced with permission.^[34] Copyright 2018, AAAS. e) The CTF-corrected and denoised and f) the symmetry-imposed and lattice-averaged images (model embedded) acquired with a dose of $20 \text{ e}^- \text{ \AA}^{-2} \text{ s}^{-1}$. g) the structural model for network and molecular building blocks. h) Schematic illustration of the TPA-COF nanosheets based fluorescence sensor for the DNA detection. i) The fluorescence quenching efficiency benchmark between TPA-COF nanosheets and bulk TPA-COF. Reproduced with permission.^[29] Copyright 2017, American Chemical Society.

as-formed Li dendrites.^[19] As shown in Figure 8a,b, the freshly prepared specimen was rapidly frozen by liquid nitrogen and then transferred to the cryo-EM holder. Then the atomic structures, growth directions and facets of Li dendrites along different directions can be directly observed with high resolution by using a Cs-corrected TEM (Figure 18). It is concluded that the Li metal dendrites in carbonate-based electrolytes tend to grow as single crystals with preferential growth directions along the [111], [110], and [211] axes,^[19] which provides an explicit understanding of the atomic-level failure mechanisms in high-energy batteries. The cryo-EM technique itself also provides a powerful tool for imaging similar Li-containing electrode systems toward the exploration of fundamental and mechanistic

aspects associated with electrochemical processes involved in LIBs. More recently, it is also proposed that integrating multi-channel STEM imaging (ptychography, HAADF and DPC) and spectroscopy (EDS and EELS) will provide a thorough and reliable solution to the native structure and chemistry of battery materials.^[339]

4.3. Surface Structure Elucidation

The surface termination structure of materials plays an important role in determining many physicochemical properties including gas adsorption/desorption, catalytic, electrical, and

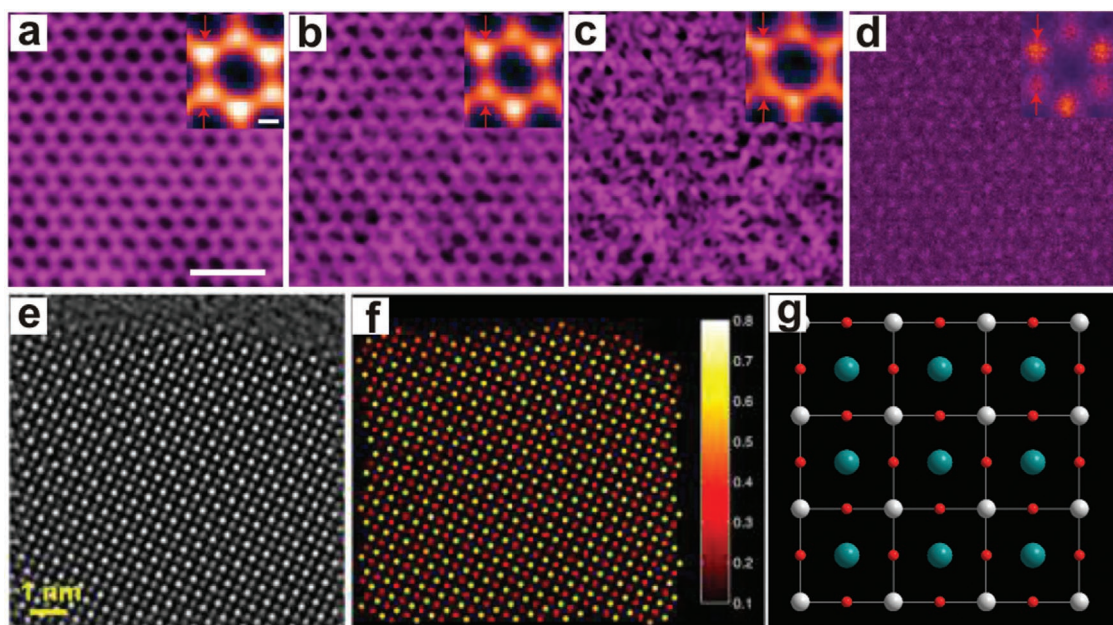


Figure 17. Low-dose imaging of 2D materials through electron phase retrieval techniques. a–c) Phase maps of ptychographic reconstructions from the same region under doses of 1.57×10^5 , 2.75×10^3 and $4.03 \times 10^2 \text{ e} \text{ \AA}^{-2}$; d) HAADF image of monolayer MoS_2 recorded with a dose of $3 \times 10^3 \text{ e} \text{ \AA}^{-2}$ (scale bars: 1 nm). All with their respective unit-cell averaged maps embedded as insets (scale bars: 1 Å). Reproduced with permission.^[296] Copyright 2019, Springer Nature. e) The reconstructed phase image of perovskite CsPbCs_3 nanosheet in the [001] projection obtained by reconstructing 80 low dose-rate AC-HRTEM images via exit-wave reconstruction with a dose rate of $100 \text{ e} \text{ \AA}^{-2} \text{ s}^{-1}$. f) Atomic-scale 2D phase mapping. g) The [001] atomic model of fcc CsPbCs_3 . Reproduced with permission.^[37] Copyright 2016, American Chemical Society.

optical properties.^[340–344] The atomic-level structure elucidation of diverse surface termination modes for materials actually bridges the gap between mechanistic and performance

studies, which is however difficult because conventional crystallographic methods cannot resolve local surface structures. Scanning tunneling microscopy (STM) offers a “top-view” of

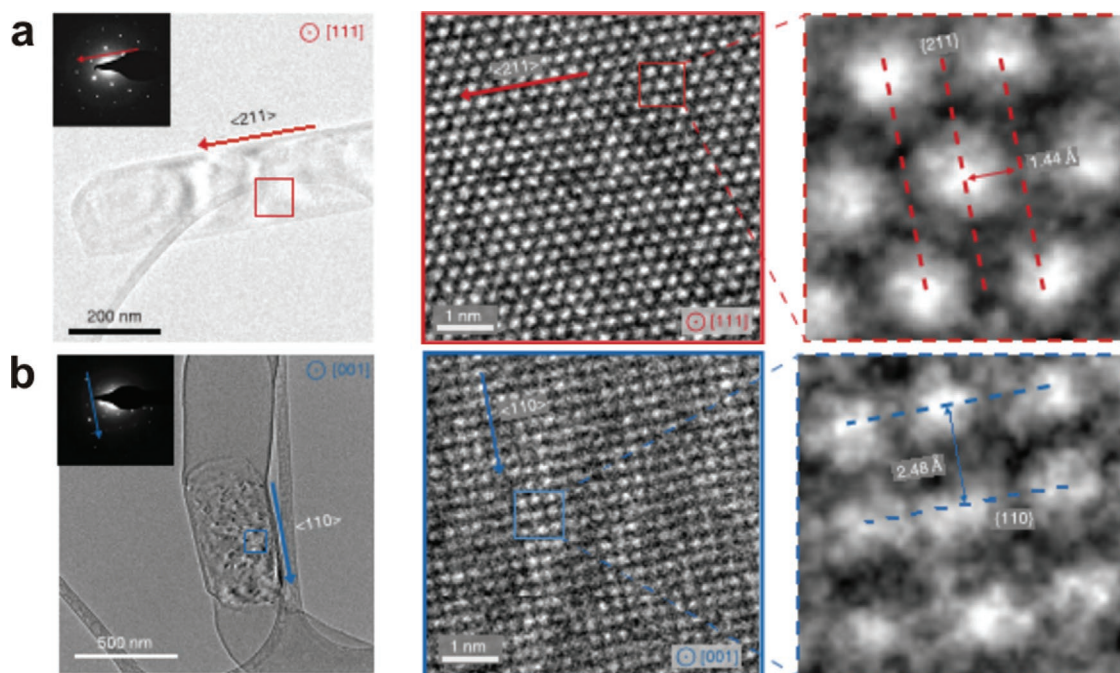


Figure 18. The crystal structure elucidation for lithium dendrites under cryogenic imaging conditions. Low-magnification TEM, electron diffraction and atomic-resolution HRTEM images (electron dose rate $\approx 1000 \text{ e} \text{ \AA}^{-2} \text{ s}^{-1}$ for $\approx 30 \text{ s}$) of lithium dendrites projected along a) [111] and b) [100] directions. Reproduced with permission.^[19] Copyright 2017, AAAS.

surface, but is largely restricted to clean and conductive surfaces.^[345] Undoubtedly, TEM is among one of the most efficient techniques that are able to characterize surface structures from multiple correlated “side-views” and at atomic resolution, toward a more robust surface structure elucidation and termination model construction.^[346] Nevertheless, surface structure elucidation for beam-sensitive materials is challenging and requires the involvement of the state-of-the-art dose-efficient EM imaging techniques.

As a representative study, the surface termination structures of ZIF-8(Zn) and UiO-66(Zr) MOFs as extremely beam sensitive materials can be directly imaged by using the low-dose DDC-HRTEM strategy under a typical cumulative dose below $\approx 10 \text{ e}^- \text{Å}^{-2}$.^[34,35] Specifically, the surface termination modes of ZIF-8(Zn) crystals with a rhombic dodecahedral shape that exposes the {110} facets are directly imaged upon the [111] projection, where “armchair”-type termination is identified (Figure 19a,b) and subject to further “arm-to-notch” adhesion with each other.^[35] Moreover, similar study was carried out on a UiO-66(Zr) crystal with a truncated octahedral shape.^[34] The {100} and {111} surface terminations of the truncated octahedral UiO-66(Zr) crystal can be simultaneously studied at atomic resolution along the [110] zone axis (Figure 19c). Surprisingly, the {111} surface mainly terminates with BDC linkers while the truncated {100} surface mainly exposes Zr clusters (Figure 19d,e). Recently, the synthesis-dependent {111} surface termination structures of octahedral shaped MIL-101 crystals have been reported.^[137] It has been found the MIL-101 synthesized with no additives or with HF exhibits the same open surface termination with 8 residual supertetrahedrons (Figure 19f–h). On the other hand, another complete surface termination mode with 10 residual supertetrahedrons can be observed when acetic acid is used as the additive. After heating at 150 °C under the vacuum, the completeness of surface cage decreases remarkably (Figure 19i–k). These low dose EM observations have strong implications for the unambiguous atomic-level understanding of facet-dependent catalytic properties on MOFs.

As a 2D material, the edge termination modes of graphene greatly affect their catalytic, photoluminescence and electronic properties.^[347–349] It has been reported the edge of graphene could terminate as zigzag, armchair and reconstructed 5–7 zigzag configurations with different electronic structures.^[347] The theoretical calculation shows the zigzag edge could exhibit an extra nonbonding π electron state, which accounts for the lower stability of nanosheet terminated with zigzag edges than that terminated with armchair edges.^[350,351] Besides, localized spins occurring in the zigzag edge might lead to the appearance of ferromagnetism.^[352] The investigation of the edge structures at atomic level by TEM would facilitate the better understanding of electronic features of graphene. The zigzag and armchair edges of graphene have been directly imaged at low-kV by Cs-corrected TEM.^[353] The conversion from the armchair to the zigzag edge may occur due to their different stabilities.^[151] He et al. found that the zig-zag edge dominates at relatively low temperature (below 400 °C) while the armchair and reconstructed 5–7 zigzag configurations dominates at high temperature (high than 600 °C) (Figure 20a,b).^[354] They also observed the zig-zag edges of graphene, which are produced by sputtering in vacuum, could exist without any

functionalization (Figure 20c).^[355] Further analysis on the C–C bond length distributions shows about 86% contraction at these edges relative to the bulk (Figure 20d).

4.4. Interfacial Structure Elucidation

Interfacial structures play important roles affecting many physicochemical properties of materials such as ferroelectricity, strain, catalytic activity and stability due to the combined geometric and electronic effects.^[356–359] For example, the metal/metal oxide interface has widely been reported to be catalytically significant and account for the strong metal support interactions.^[360,361] On the other hand, the metal/metal interface is important for the complicated atomic diffusion behaviors across the interface (e.g., the Kirkendall effect).^[362] The physical origin of these effects actually depends on the atomic-level interfacial structure, either coherent or incoherent, which could be directly figured out by EM imaging and moreover with dose-efficient techniques once the materials are beam-sensitive.^[35]

Many MOF crystals have very regular shapes and are widely observed to self-assemble and tile the space.^[363,364] Those MOF/MOF interfaces that appear to be seamless are interesting because they are closely related with gas adsorption and diffusion properties of the assembly.^[365] To unravel the very beam-sensitive MOF/MOF interfacial structures, the DDC-HRTEM strategy offers best opportunity because it has successfully resolved the periodic crystal structure of ZIF-8(Zn) crystals.^[35] For the interface between assembled ZIF-8(Zn) rhombic dodecahedral crystals, it is interesting to observe that the assembled ZIF-8(Zn) crystals form a coherent interface through the “arm-to-notch” adhesion between neighboring armchair terminated {110} surfaces (Figure 21a). The coherent interface creates interfacial cavities other than the intrinsic microporosity of ZIF-8(Zn) framework, which has been predicted to enhance the diffusivity of various molecules (i.e., H_2 , N_2 , CH_4 , and CO_2) based on the molecular dynamics simulations (Figure 21b).^[35]

For 2D materials, the interfacial structure could affect both the electronic and mechanical properties.^[366,367] Imaging the grain boundary of graphene not only help to build their structure–property relationships, but also work for the engineering the periodic grain boundaries with tunable electrical transport properties.^[367] Yazyev and Louie calculated the charge carrier transmission through grain boundaries in graphene based on the momentum conservation principle.^[368] The results shows the charge carrier transmission could have two distinct transport behavior, which depend on the types of grain boundaries, as shown in Figure 21d.^[368] As a practice, Huang et al. used Cs-corrected STEM to image the grain boundary of graphene under low-kV.^[369] The two grains shown in Figure 21c exhibit an intersection angle of 27° and the tilt boundary is composed of a series of pentagons, heptagons and distorted hexagons along a straight line. Additionally, the measured mechanical strength and electrical properties of these grain boundaries indicate well maintained electrical properties but degraded mechanical strength.^[369]

Another example for imaging beam-sensitive 2D materials is conducted on a 2D CsPbBr_3 inorganic perovskite as an excellent model structure for a wide range of photovoltaic, photocatalytic

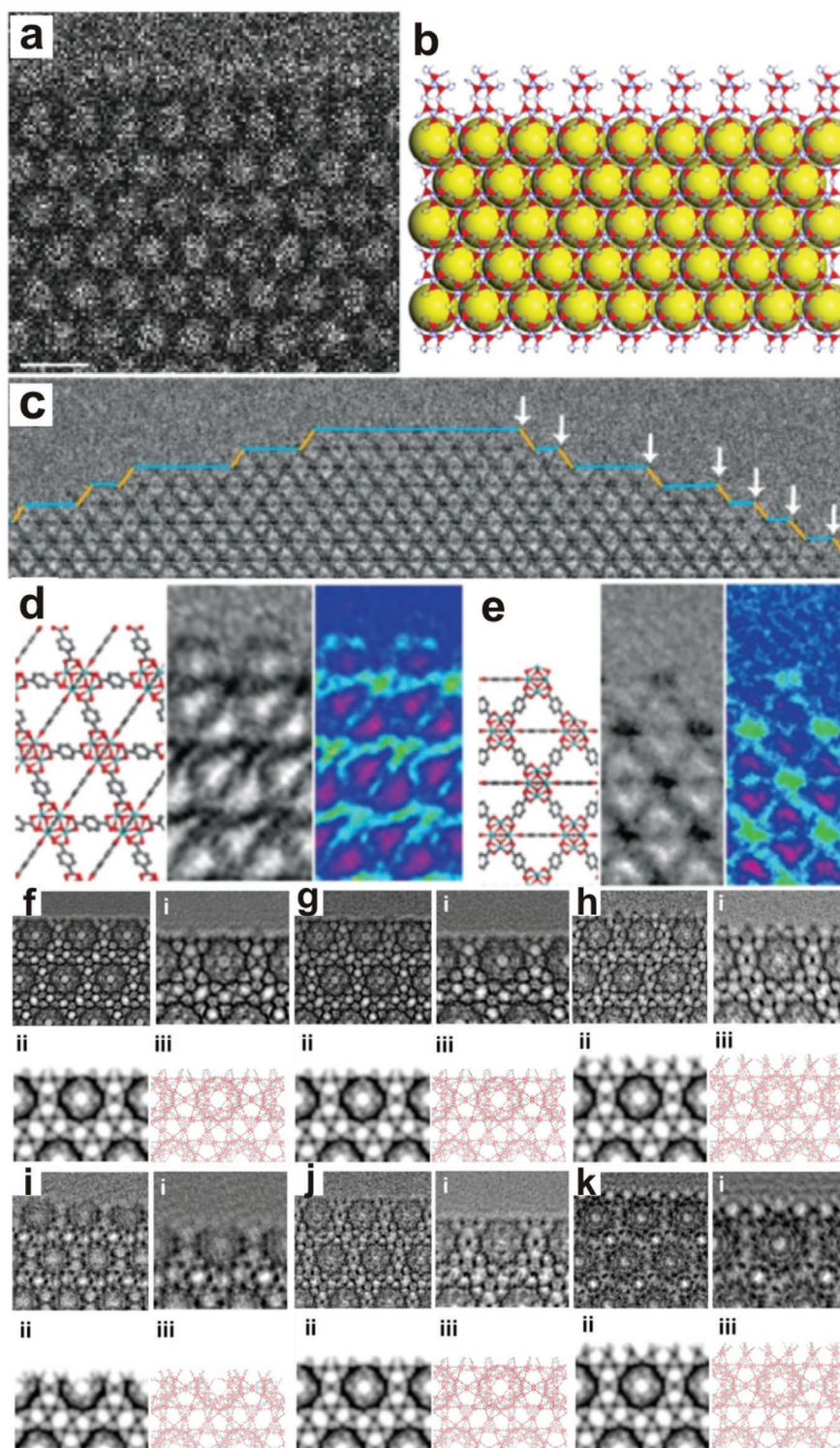


Figure 19. The low-dose HRTEM imaging of surface termination structures of MOFs by DDC. a,b) HRTEM image (obtained at a dose of $4.1 \text{ e} \text{ \AA}^{-2}$) and surface termination model of ZIF-8 rhombic dodecahedral crystals viewed along the $[111]$ direction; Reproduced with permission.^[35] Copyright 2017, Springer Nature. c–e) HRTEM image (obtained at a dose rate of $\approx 2.0 \text{ e} \text{ \AA}^{-2} \text{ s}^{-1}$ and a total dose of $12 \text{ e} \text{ \AA}^{-2}$) and structural models for two distinct types of surface termination modes in UiO-66 truncated octahedral crystals viewed along the $[110]$ direction. Reproduced with permission.^[34] Copyright 2018, AAAS. CTF-corrected HRTEM images (acquired with a total electron dose of $\approx 8 \text{ e} \text{ \AA}^{-2}$ and a total exposure of 6 s) of f,g,h) freshly synthesized MIL-101 samples and i,j,k) the vacuum-heated MIL-101 samples (at 150°C) prepared f,i) with HF; g,j) without additives, and h,k) with acetic acid. Here, i, ii and iii represent real-space averaging image, the simulated projected potential map, and the projected structural model, respectively. Reproduced with permission.^[137] Copyright 2019, American Chemical Society.

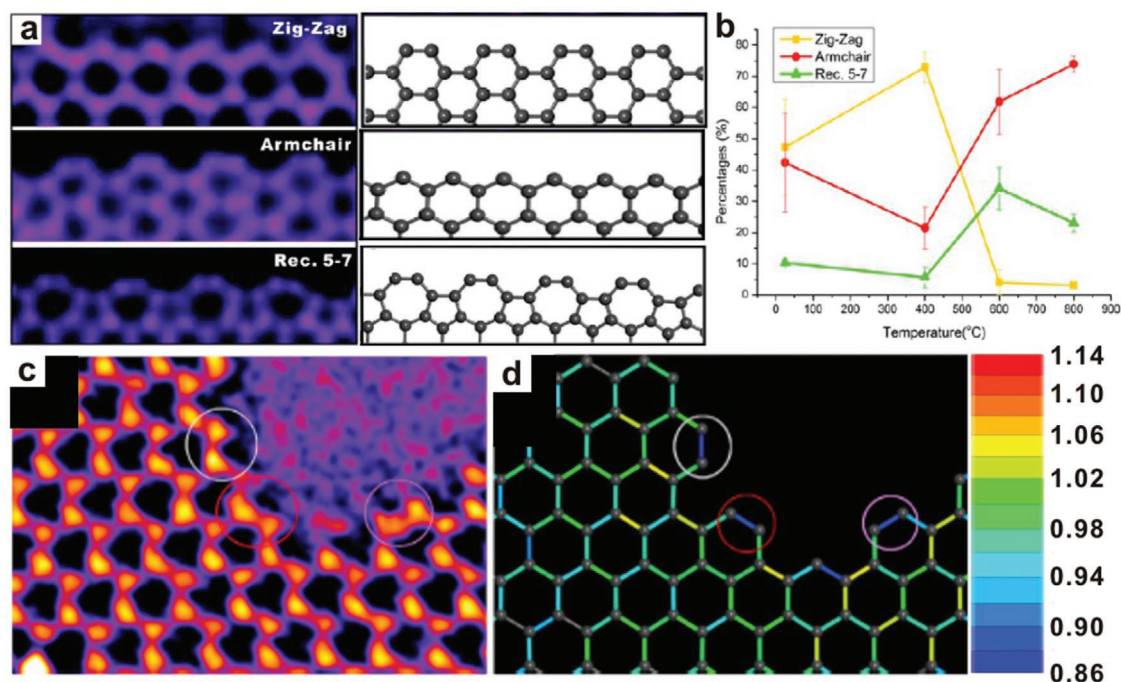


Figure 20. The surface termination structures for 2D materials. a) Low-kV aberration-corrected atomic-resolution STEM image of zig-zag, armchair and Rec.5-7 types of surface termination modes. b) Temperature-dependent percentages of three different edge configurations. Reproduced with permission.^[354] Copyright 2015, American Chemical Society. c) Low-kV aberration-corrected HRTEM image and d) measured bond length distribution represented in ratio values and color scales. Reproduced with permission.^[355] Copyright 2014, Springer Nature.

and photodetector applications.^[370–372] Many of its important physicochemical properties have been studied based on its perfect crystal structure models.^[373,374] By Cs-corrected STEM, Yu et al. observed the existence of domains with a Ruddlesden–Popper (RP)-type phase and related domain boundaries in 2D CsPbBr₃ nanosheets.^[375] Moreover, the domain boundaries between the RP phase and conventional perovskite phases have been clearly revealed at the atomic level as shown in Figure 21e–i.^[375]

The interface problem is also very important for energy materials, e.g., the solid electrolyte interface (SEI) problem in the field of Li-ion batteries.^[376,377] Electrolyte in Li-ion battery are easily decomposed during electrochemically driven process and form an SEI layer with Li metal.^[378] It is vital to elucidate the nanostructure of SEI for further improving the performance of Li-ion batteries. However, Li-containing electrode materials and organic liquid electrolytes are very sensitive to the electron beam irradiation, which severely restricts the direct TEM imaging of their interfacial structures.^[19] Cui's group observed the interface between Li and electrolyte by freezing the specimen via the Cryo-EM approach.^[19] In the SEI area between Li metal dendrite and carbonate-based electrolyte (i.e., ethylene carbonate diethyl carbonate (EC/EDC)), small grains as indexed by Li carbonate (Li₂CO₃, orange circles) and Li oxide (Li₂O, red circles) are observed (Figure 22a), which disperse throughout the amorphous film.^[19] In another SEI area between Li metal dendrite and carbonate-based electrolyte with (10 vol%) fluoroethylene carbonate (FEC), a multilayer structure containing an amorphous polymer matrix inner layer and Li oxide outer layer is observed (Figure 22b).^[19] They

further connected the interface structure with the operation temperature of Li ion batteries.^[379] A high operating temperature of 60 °C leads to larger Li particles and better crystallized SEI nanostructure than those at 20 °C. Such interfacial structure results in faster charge transport kinetics, enhanced Coulombic efficiency and better stability.^[379]

Energy storage is another important branch for the applications associated with energy materials. Hydrogen, as a prospective fuel with high volumetric density, could be produced by water reduction and widely used in energy conversions.^[380,381] However, the storage of hydrogen remains a challenge due to the fact that hydrogen cause embrittlement to metals.^[382] Revealing the location of hydrogen atoms in metals provides mechanistic insights into the hydrogen storage process and promotes new strategies toward the control of hydrogen embrittlement damage.^[383,384] However, imaging hydrogen atoms is among one of the most challenging tasks for electron microscopy because hydrogen is the lightest element, especially when the target material is beam-sensitive.^[264] As mentioned above, most of the elements could be imaged by iDPC-STEM that is also a dose-efficient imaging technique.^[268] Recently, atomic-resolution imaging of hydrogen have been realized at the interface between the hexagonal close-packed titanium and face-centered tetragonal titanium monohydride by using and Cs-corrected iDPC-STEM (Figure 22c–h).^[385] The ideal interface between γ -TiH and α -Ti could have three potential models of atomic arrangements (Types I–III; Figure 22e). Comparing the images that are obtained from HAADF, ABF, and iDPC, it is concluded that iDPC has superior performance than ABF and HAADF regarding the detection of light elements.^[385]

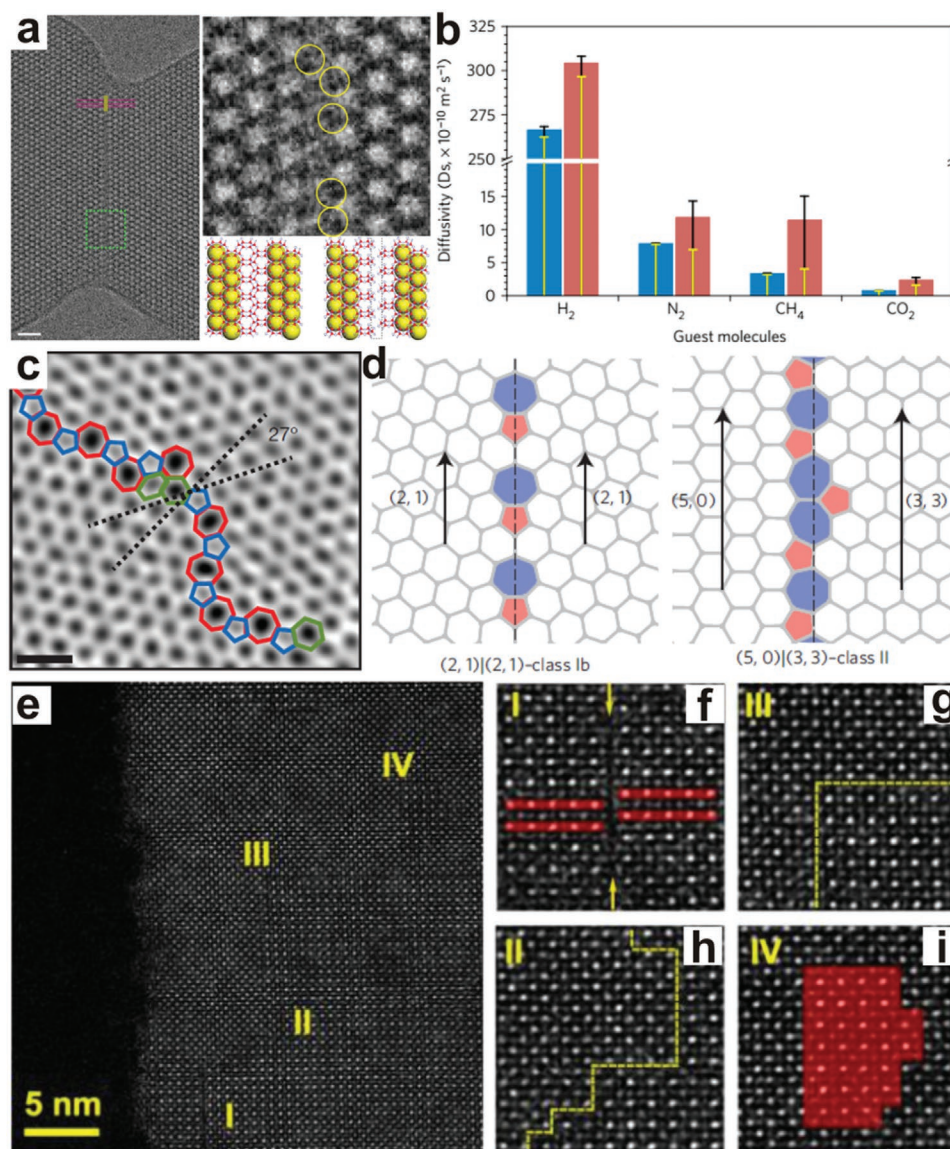


Figure 21. Imaging interfacial structures of 2D materials. a) The low-dose HRTEM image, CTF-corrected/denoised image and structural model of the coherent interface formed by two attached ZIF-8 crystals. b) Molecular dynamics simulated self-diffusivities of different guest molecules for bulk (blue) and interfacial structures (red) of the microporous ZIF-8 frameworks. Reproduced with permission.^[35] Copyright 2017, Springer Nature. c) Low-kV Cs-corrected STEM image of a high-angle tilt grain boundary of graphene. Reproduced with permission.^[369] Copyright 2011, Springer Nature. d) Typical grain boundary models of graphene with different charge transport properties. Reproduced with permission.^[368] Copyright 2010, Springer Nature. e) Cs-corrected STEM images for different types of domains and associated domain boundaries in 2D CsPbBr₃ nanosheets. f–i) Enlarged image of regions I, II, III, and IV in (e). Reproduced with permission.^[375] Copyright 2017, American Chemical Society.

According to the iDPC-STEM result, the interface follows the type I structural model.

4.5. Structural Elucidation of Defects and Partial Disorder

For crystalline materials, defects define any structural imperfections and irregularities with respect to a long-range ordered perfect structure.^[386] On the other hand, partial disorder also refers to the structural deviation from the perfectly ordered structure, but is more specifically defined by the microscopic coexistence of long-range structural order and disorder. These

highly localized structural features affect not only the physicochemical properties of materials, such as mechanical, optical, electrical and magnetic properties,^[387–389] but also their applications in electronic devices, catalysis, gas storage and separation.^[390–392] The characterizations of various defects and partial disorder is difficult, especially at nanoscopic or even atomic scale. EM imaging is widely used to probe such local structures, such as defects and partial disorder.^[135,393,394] Similar difficulty appears when the defective materials are beam sensitive, which can be tackled by diverse dose-efficient EM imaging techniques.

The defects belong to a type of most important local structures for the beam-sensitive MOFs, because they are closely

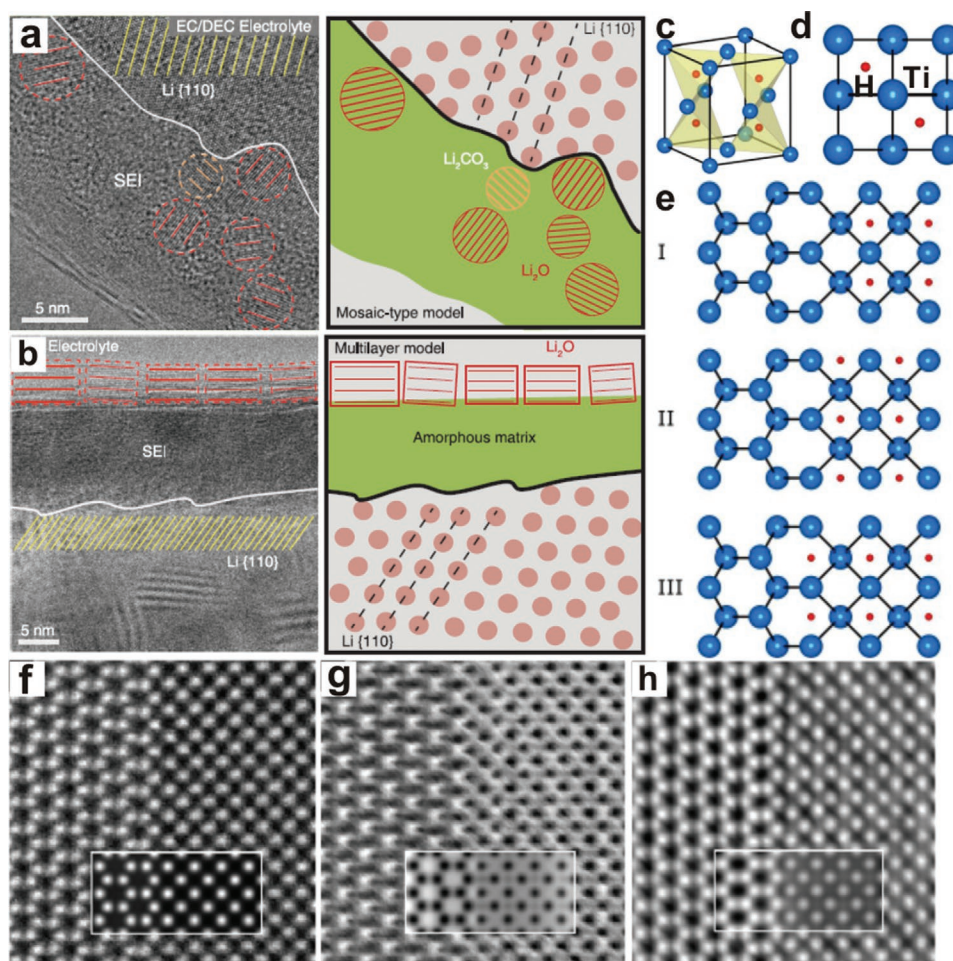


Figure 22. Imaging interfacial structures of energy materials. a) Cryogenic HRTEM image and corresponding scheme of the SEI region for lithium-ion battery between a) Li metal and EC/DEC and b) Li metal and FEC electrolyte. Reproduced with permission.^[19] Copyright 2017, AAAS. c–e) The γ -TiH unit-cell and possible γ -TiH/ α -Ti interface models. STEM images of γ -TiH/ α -Ti interface using f) HAADF, g) ABF, and h) iDPC modes with simulated images as insets. Reproduced with permission.^[385] Copyright 2018, Cornell University.

related with their catalytic and gas adsorption/diffusion properties.^[120,138,395] Most of those “indirect” characterization techniques, such as X-ray or electron diffraction, fails to figure out the intrinsic structures of defects in MOFs simply because most defects are nonperiodic.^[396] Taking the chemically induced defects in UiO-66 MOFs as an example, it has been a long way before any types of defects in UiO-66 MOFs can be clearly and directly elucidated.^[135] The exact structure of these defects is at first conceived to originate from disordered solvents in the framework,^[397] which was later excluded and proved to be “missing clusters” by combined diffuse scattering, electron microscopy, anomalous X-ray scattering and pair distribution function measurements.^[396] Recently, Han and co-workers directly observed the coexistence of ordered “missing linker” and “missing cluster” defects in the UiO-66 by combining low-dose DDC-HRTEM and ED technique.^[135] Comparing the perfect UiO-66 in **Figure 23a,b**, the defective UiO-66 shown in **Figure 23c–e** exhibit missing contrast of benzene rings at the crystallographic sites occupied by BDC linkers and thus indicative of the presence of ordered missing linker defects. Specifically, this conclusion is supported by images

taken along multiple projections: i) along the [110] direction, the triangle-shaped channels are merged together to become the rhombus-shaped channels because of the missing linkers (**Figure 23b,e**); ii) along the [001] direction, the contrasts of BDC linkers that are encompassed by four Zr_6O_8 clusters present in **Figure 23a** but not in **Figure 23c**. On the other hand, as shown in **Figure 23g,h**, there are two types of missing cluster defects observed: one with an REO net, in which Zr_6O_8 has eight-connected with surrounding clusters through BDC linkers; the other with an SCU net, in which one-third of the Zr_6O_8 clusters has eight-connected while the remaining two-third four-connected.^[135]

Various types of defects are also very important for 2D materials. By using DPC-STEM at 80 kV, the topological defects in graphene, including dopants, Stone–Wales (SW) defects and nanopores, have been revealed.^[398] The defects in graphene affect both the local atomic configuration and their chemical bonding state, which is especially difficult to be mapped at atomic resolution due to the weak signal of electronic fine structure.^[398] **Figure 24a–c** clearly shows the SW defects (5–7–7–5) structure and atomic electric fields.^[398] The four sets of SW

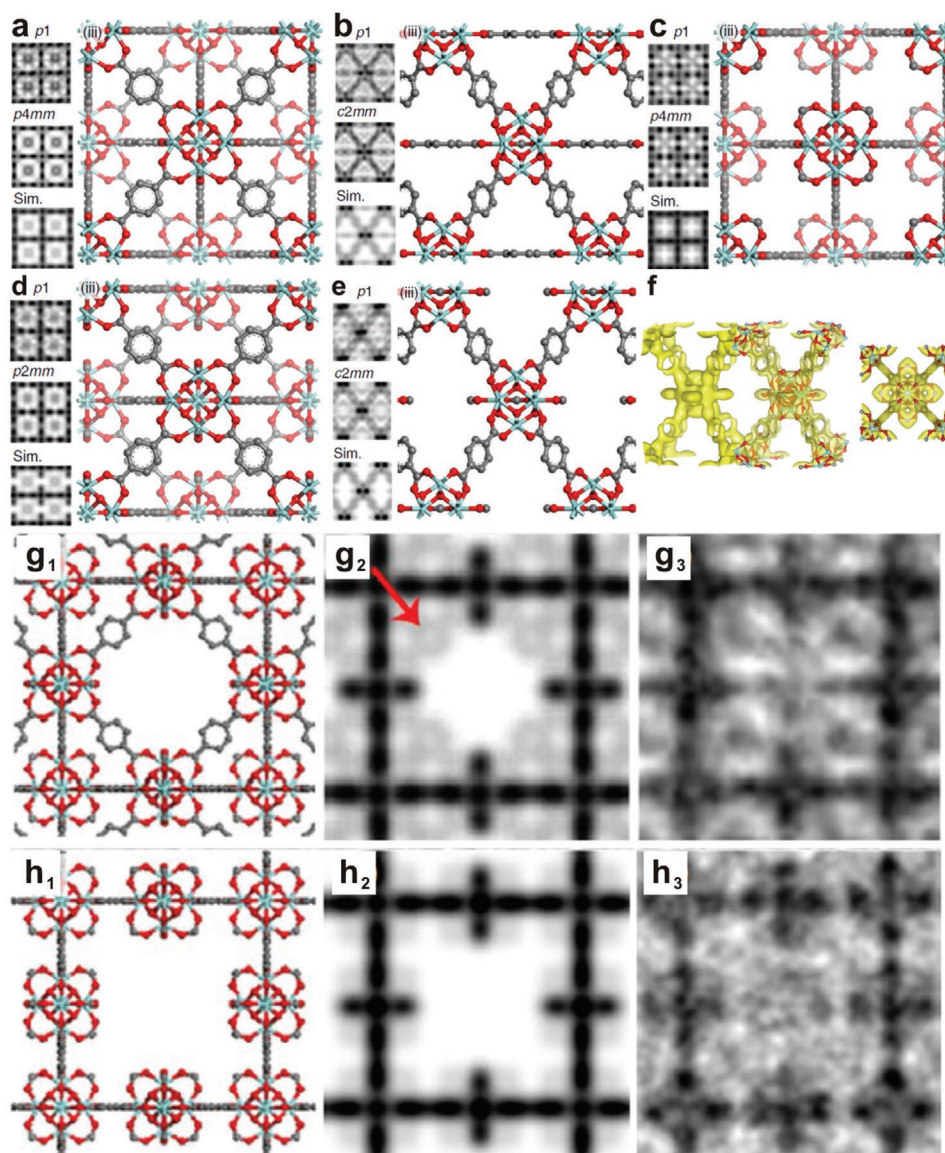


Figure 23. Low-dose HRTEM imaging of defects in MOFs using DDCs. The lattice averaged and/or symmetry-imposed image motifs and simulated potentials of a,b) perfect, c–f) missing ligands defects, and g,h) missing clusters defects for UiO-66 nanocrystals. Based on the perfect UiO-66 structure viewed along a) [001] and b) [110] directions, the structural model involving missing ligands defects can be observed along c) [001], d) [100], and e) [110] directions, which can be further visualized in 3D as shown in (f). g,h) From the [001] projection, the structural projection, potential map and averaged motif image indicates two different types of missing cluster topologies: g₁–g₃) REO and h₁–h₃) SCU. A dose rate of 0.01–0.03 e Å^{−2}s^{−1} was used for specimen searching, zone axis alignment, and prefocusing. Reproduced with permission.^[135] Copyright 2019, Springer Nature.

defects are connected by one six membered rings. Besides, the nanopores (Figure 24d–f), which show strong electric field, are also observed in the bilayer graphene.^[398] Electron ptychography as another dose-efficient diffractive imaging technique, could also be used to identify a point defect in 2D materials. A monolayer of MoS₂ is imaged by EMPAD pixelated detector, which could form a 4D-STEM dataset, at a primary beam energy of 80 keV to avoid the knock-on damage.^[294] From Figure 24g–i, the reconstructed phase image using full-field ptychography, a sulfur monovacancy could be clearly observed. Compared to the coherent bright-field image, incoherent ADF image and integrated center-of-mass (iCoM) image, the image obtained by the

ptychography shows higher information limit approaching the Abbe resolution of 0.39 Å.

Partial disorder is another very important local feature for both ferroelectric and ferromagnetic materials.^[399–401] For example, the presence of polar nanodomain arising from partial disorder in the relaxor-based ferroelectrics could contribute to the longitudinal piezoelectricity property of relaxor-PbTiO₃ crystals.^[400,401] Benefiting from the dose-efficient EM imaging techniques, such partial disorder features can be directly imaged on beam sensitive materials. For example, the partial disorder phenomenon of organic–inorganic hybrid perovskite has been explicitly observed by HRTEM imaging coupled with the

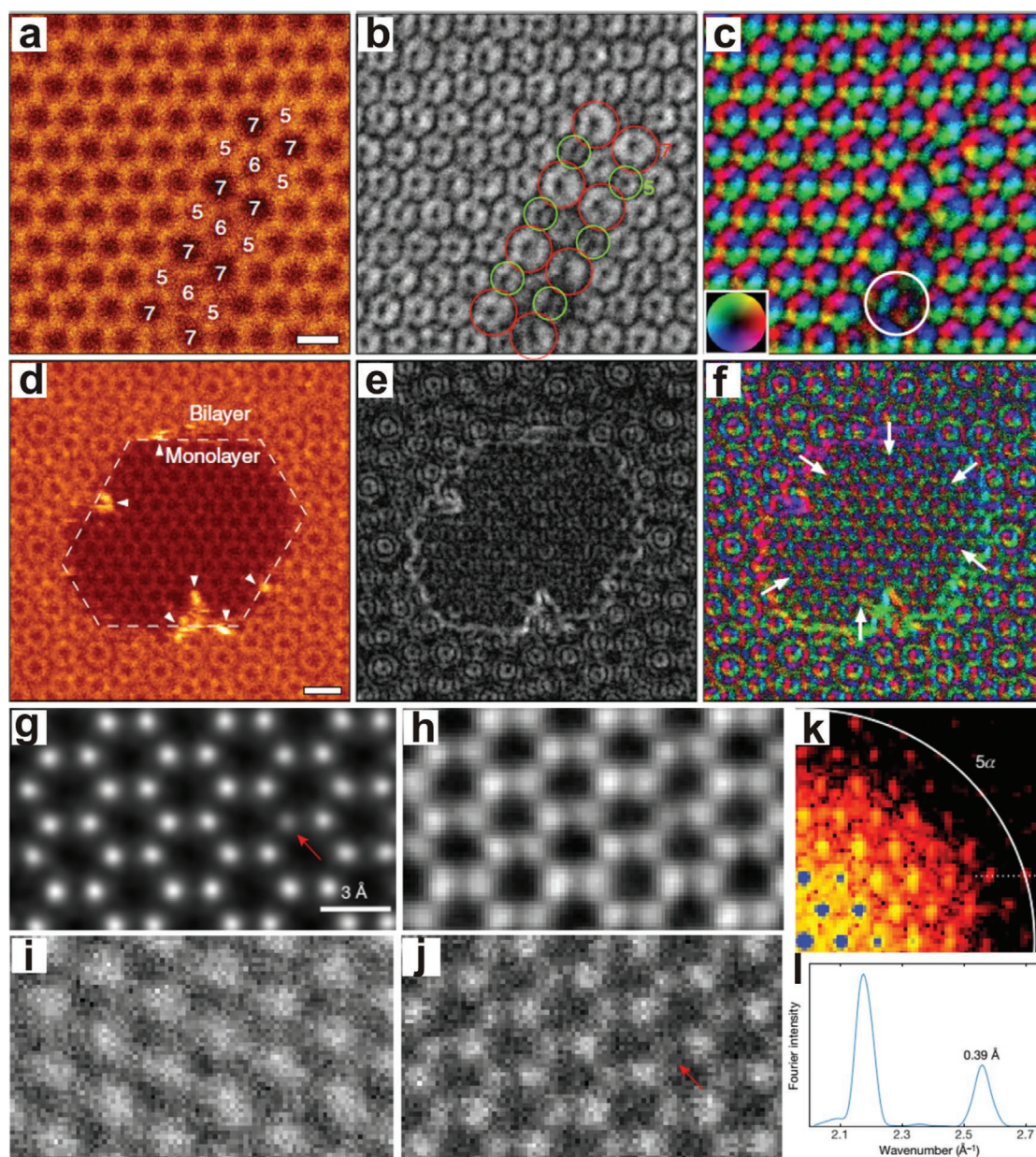


Figure 24. Imaging defects in 2D materials. a–f) From left to right, low-kV atomic-resolution ADF-STEM image, electric field strength maps and electric field vector maps derived from DPC-STEM of a–c) Stone–Wales defects and d–f) nanopore region in graphene. Reproduced with permission.^[398] Copyright 2018, Springer Nature. g–l) Imaging a point defect in MoS₂ by ptychography. g) The phase image constructed by ptychography, h) iCoM image, i) coherent bright-field image, and j) incoherent ADF image. k) Part of false-colored diffractogram intensities (on a logarithmic scale) of full-field ptychography. l) Line profile along the dotted horizontal white line in (k) across two diffraction spots. Reproduced with permission.^[294] Copyright 2018, Springer Nature.

DDC.^[35] From an HRTEM image of the CH₃NH₃PbBr₃ crystal as shown in **Figure 25**, two types of ordered and nanometer-sized domains with off-centered displaced CH₃NH₃ cations are unambiguously identified.^[35] The off-center displaced CH₃NH₃ cations have a “head-on” orientation in one type of nanodomain while a “side-on” orientation in another, which are associated with “out-of-plane” and “in-plane” electric dipoles. These observations may help to provide a solid atomic-level structural model for understanding many interesting physicochemical properties of organic–inorganic hybrid perovskites.

5. Summary and Outlook

In this work, inspired by the emerging need for imaging beam-sensitive materials, we systematically summarized the structural aspects against beam damages, based on the theories of beam damage mechanisms and quantitative beam damage measurements. After further reviewing the essential advances in dose-efficient EM imaging techniques and methods categorized according to the electron optics system, specimen stage system and electron detection system respectively, the

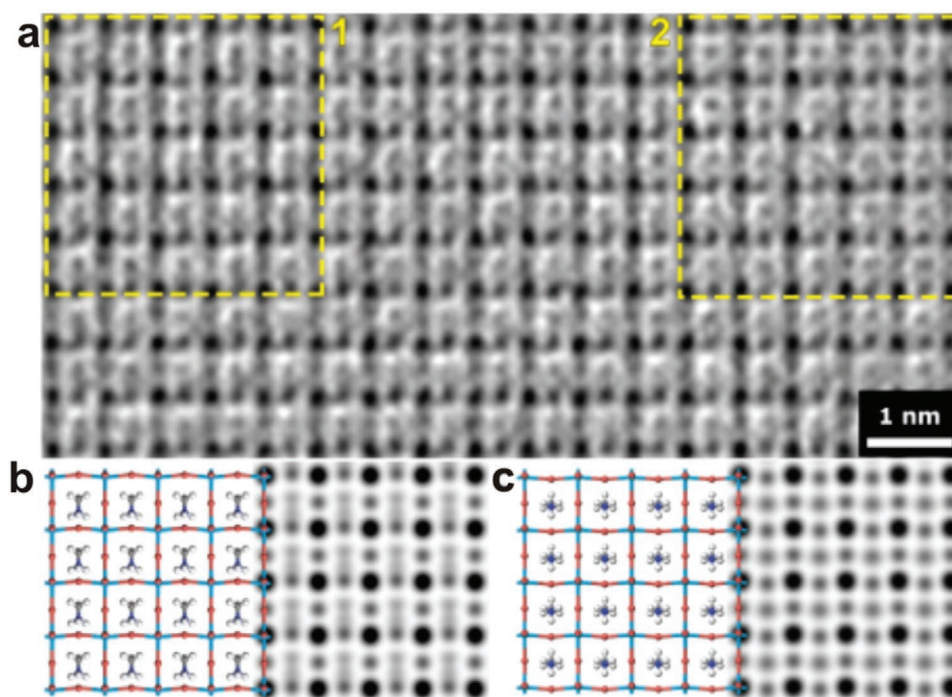


Figure 25. Low-dose imaging of partial disorder in organic–inorganic hybrid perovskite at a dose rate of $\approx 3.7 \text{ e } \text{\AA}^{-2} \text{ s}^{-1}$ and a total dose of $11 \text{ e } \text{\AA}^{-2}$. a) CTF-corrected denoised HRTEM image of $\text{CH}_3\text{NH}_3\text{PbBr}_3$. b,c) The structural model (left) and simulated potential map (right) of $\text{CH}_3\text{NH}_3\text{PbBr}_3$ with different CH_3NH_3 orientations of regions that shown in a, respectively. Reproduced with permission.^[34] Copyright 2018, AAAS.

associated cutting-edge materials science applications and discoveries were reviewed. Future trends for imaging beam-sensitive materials may include the combination of multiple dose-efficient imaging techniques, such as cryo-EM and DDC-HRTEM/iDPC-STEM, which could markedly enhance the critical dose of materials without compromising the image SNR and resolution. Moreover, the extensive utilization of ultrafast or pixelated electron detectors also brings the new opportunities for research fields associated with big data management, processing and analytics (i.e., data mining and data analysis).

Acknowledgements

Y.Z. acknowledges the financial support from the National Natural Science Foundation of China (Grant Nos. 21771161 and 51701181), the Zhejiang Provincial Natural Science Foundation of China (Grant No. LR18B030003), and Thousand Talents Program for Distinguished Young Scholars. C.Z. acknowledges the financial support from the National Natural Science Foundation of China (Grant No. 61871134), Shanghai Municipal Science and Technology Commission (Grant No. 18JC1410300), and Fudan University Scientific Research Foundation (IDH1512043). C.D. acknowledges the financial support from the National Science Foundation (Grant Nos. 1936882 and DMR-1920335) and is grateful for Fudan University Key Laboratory Visiting Fellowship (Grant No. GF2019_05). The authors thank Y. Yao from Beijing National Laboratory for Condensed Matter Physics for useful discussions.

Conflict of Interest

The authors declare no conflict of interest.

Keywords

beam-sensitive materials, electron microscopy, low dose, MOFs, 2D materials

Received: November 20, 2019

Revised: December 20, 2019

Published online: February 28, 2020

- [1] M. Haider, H. Rose, S. Uhlemann, B. Kabius, K. Urban, *J. Electron Microsc.* **1998**, 47, 395.
- [2] J. M. Rodenburg, in *Advances in Imaging and Electron Physics*, Vol. 150, Elsevier, Amsterdam **2008**, p. 87.
- [3] G. A. Botton, S. Lazar, C. Dwyer, *Ultramicroscopy* **2010**, 110, 926.
- [4] J. J. De Yoreo, N. A. J. M. Sommerdijk, *Nat. Rev. Mater.* **2016**, 1, 16035.
- [5] A. J. McKenna, J. K. Eliason, D. J. Flannigan, *Nano Lett.* **2017**, 17, 3952.
- [6] V. A. Lobastov, J. Weissenrieder, J. Tang, A. H. Zewail, *Nano Lett.* **2007**, 7, 2552.
- [7] C. Kisielowski, P. Specht, B. Freitag, E. R. Kieft, W. Verhoeven, J. F. M. van Rens, P. Mutsaers, J. Luiten, S. Rozeveld, J. Kang, A. J. McKenna, P. Nickias, D. F. Yancey, *Adv. Funct. Mater.* **2019**, 29, 1807818.
- [8] D. R. Cremons, D. A. Plemmons, D. J. Flannigan, *Nat. Commun.* **2016**, 7, 11230.
- [9] R. Imbihl, J. E. Demuth, *Surf. Sci.* **1986**, 173, 395.
- [10] R. Neudert, M. Knupfer, M. S. Golden, J. Fink, W. Stephan, K. Penc, N. Motoyama, H. Eisaki, S. Uchida, *Phys. Rev. Lett.* **1998**, 81, 657.
- [11] R. Fernandez-Leiro, S. H. Scheres, *Nature* **2016**, 537, 339.

- [12] J. Dubochet, *Angew. Chem., Int. Ed.* **2018**, 57, 10842.
- [13] J. Dubochet, E. Knapek, *PLoS Biol.* **2018**, 16, 2005550.
- [14] R. M. Glaeser, *Curr. Opin. Colloid Interface Sci.* **2018**, 34, 1.
- [15] J. G. Galaz-Montoya, S. J. Ludtke, *Biophys. Rep.* **2017**, 3, 17.
- [16] J. Frank, *Nat. Protoc.* **2017**, 12, 209.
- [17] A. Merk, A. Bartesaghi, S. Banerjee, V. Falconieri, P. Rao, M. I. Davis, R. Prangani, M. B. Boxer, L. A. Earl, J. L. S. Milne, S. Subramaniam, *Cell* **2016**, 165, 1698.
- [18] X. Wang, M. Zhang, J. Alvarado, S. Wang, M. Sina, B. Lu, J. Bouwer, W. Xu, J. Xiao, J. G. Zhang, J. Liu, Y. S. Meng, *Nano Lett.* **2017**, 17, 7606.
- [19] Y. Li, Y. Li, A. Pei, K. Yan, Y. Sun, C. L. Wu, L. M. Joubert, R. Chin, A. L. Koh, Y. Yu, J. Perrino, B. Butz, S. Chu, Y. Cui, *Science* **2017**, 358, 506.
- [20] A. Mayoral, T. Carey, P. A. Anderson, A. Lubk, I. Diaz, *Angew. Chem., Int. Ed.* **2011**, 50, 11230.
- [21] O. Ugurlu, J. Haus, A. A. Gunawan, M. G. Thomas, S. Maheshwari, M. Tsapatsis, K. A. Mkhoyan, *Phys. Rev. B* **2011**, 83, 113408.
- [22] Y. Ma, P. Oleynikov, O. Terasaki, *Nat. Mater.* **2017**, 16, 755.
- [23] L. Liu, U. Diaz, R. Arenal, G. Agostini, P. Concepcion, A. Corma, *Nat. Mater.* **2017**, 16, 132.
- [24] H. F. Greer, W. Zhou, *Crystallogr. Rev.* **2011**, 17, 163.
- [25] T. Susi, J. Kotakoski, R. Arenal, S. Kurasch, H. Jiang, V. Skakalova, O. Stephan, A. V. Krashennikov, E. I. Kauppinen, U. Kaiser, J. C. Meyer, *ACS Nano* **2012**, 6, 8837.
- [26] R. Zan, Q. M. Ramasse, R. Jalil, T. Georgiou, U. Bangert, K. S. Novoselov, *ACS Nano* **2013**, 7, 10167.
- [27] A. Garcia, A. M. Raya, M. M. Mariscal, R. Esparza, M. Herrera, S. I. Molina, G. Scavell, P. L. Galindo, M. Jose-Yacamán, A. Ponce, *Ultramicroscopy* **2014**, 146, 33.
- [28] D. N. Bunck, W. R. Dichtel, *J. Am. Chem. Soc.* **2013**, 135, 14952.
- [29] Y. Peng, Y. Huang, Y. Zhu, B. Chen, L. Wang, Z. Lai, Z. Zhang, M. Zhao, C. Tan, N. Yang, F. Shao, Y. Han, H. Zhang, *J. Am. Chem. Soc.* **2017**, 139, 8698.
- [30] R. R. Schroder, *Arch. Biochem. Biophys.* **2015**, 581, 25.
- [31] O. H. Kwon, V. Ortalan, A. H. Zewail, *Proc. Natl. Acad. Sci. USA* **2011**, 108, 6026.
- [32] J. P. Patterson, Y. Xu, M. A. Moradi, N. Sommerdijk, H. Friedrich, *Acc. Chem. Res.* **2017**, 50, 1495.
- [33] M. R. Libera, R. F. Egerton, *Polym. Rev.* **2010**, 50, 321.
- [34] D. Zhang, Y. Zhu, L. Liu, X. Ying, C. E. Hsiung, R. Sougrat, K. Li, Y. Han, *Science* **2018**, 359, 675.
- [35] Y. Zhu, J. Ciston, B. Zheng, X. Miao, C. Czarnik, Y. Pan, R. Sougrat, Z. Lai, C. E. Hsiung, K. Yao, I. Pinnau, M. Pan, Y. Han, *Nat. Mater.* **2017**, 16, 532.
- [36] O. I. Lebedev, F. Millange, C. Serre, G. Van Tendeloo, G. Ferey, *Chem. Mater.* **2005**, 17, 6525.
- [37] Y. Yu, D. Zhang, C. Kisiowski, L. Dou, N. Kornienko, Y. Bekenstein, A. B. Wong, A. P. Alivisatos, P. Yang, *Nano Lett.* **2016**, 16, 7530.
- [38] L. Dou, A. B. Wong, Y. Yu, M. Lai, N. Kornienko, S. W. Eaton, A. Fu, C. G. Bischak, J. Ma, T. Ding, N. S. Ginsberg, L. W. Wang, A. P. Alivisatos, P. Yang, *Science* **2015**, 349, 1518.
- [39] C. J. Doonan, D. J. Tranchemontagne, T. G. Glover, J. R. Hunt, O. M. Yaghi, *Nat. Chem.* **2010**, 2, 235.
- [40] P. J. Waller, F. Gandara, O. M. Yaghi, *Acc. Chem. Res.* **2015**, 48, 3053.
- [41] T. Drake, P. Ji, W. Lin, *Acc. Chem. Res.* **2018**, 51, 2129.
- [42] B. Qiu, M. Xing, J. Zhang, *Chem. Soc. Rev.* **2018**, 47, 2165.
- [43] A. Mei, X. Li, L. Liu, Z. Ku, T. Liu, Y. Rong, M. Xu, M. Hu, J. Chen, Y. Yang, M. Gratzel, H. Han, *Science* **2014**, 345, 295.
- [44] N. J. Jeon, J. H. Noh, W. S. Yang, Y. C. Kim, S. Ryu, J. Seo, S. I. Seok, *Nature* **2015**, 517, 476.
- [45] J. C. Meyer, F. Eder, S. Kurasch, V. Skakalova, J. Kotakoski, H. J. Park, S. Roth, A. Chuvilin, S. Eyhusen, G. Benner, A. V. Krashennikov, U. Kaiser, *Phys. Rev. Lett.* **2012**, 108, 196102.
- [46] L. J. Murray, M. Dinca, J. R. Long, *Chem. Soc. Rev.* **2009**, 38, 1294.
- [47] A. H. Chughtai, N. Ahmad, H. A. Younus, A. Laypkov, F. Verpoort, *Chem. Soc. Rev.* **2015**, 44, 6804.
- [48] I. Stassen, N. Burtch, A. Talin, P. Falcaro, M. Allendorf, R. Ameloot, *Chem. Soc. Rev.* **2017**, 46, 3185.
- [49] Y. Li, K. Wang, W. Zhou, Y. Li, R. Vila, W. Huang, H. Wang, G. Chen, G.-H. Wu, Y. Tsao, H. Wang, R. Sinclair, W. Chiu, Y. Cui, *Matter* **2019**, 1, 428.
- [50] D. Liu, Z. Shadike, R. Lin, K. Qian, H. Li, K. Li, S. Wang, Q. Yu, M. Liu, S. Ganapathy, X. Qin, Q. H. Yang, M. Wagemaker, F. Kang, X. Q. Yang, B. Li, *Adv. Mater.* **2019**, 31, 1806620.
- [51] J. C. H. Spence, *Struct. Dyn.* **2017**, 4, 044027.
- [52] D. B. Williams, C. B. Carter, *Transmission Electron Microscopy: A Textbook for Materials Science*, Springer US, Boston, MA **2009**.
- [53] W. Zhou, R. Apkarian, Z. L. Wang, D. Joy, in *Scanning Microscopy for Nanotechnology*, (Eds: W. Zhou, Z. L. Wang), Springer-Verlag, New York **2007**.
- [54] J. M. Zuo, J. C. H. Spence, *Advanced Transmission Electron Microscopy*, Springer-Verlag, New York **2017**.
- [55] B. Rafferty, P. D. Nellist, S. J. Pennycook, *J. Electron Microsc.* **2001**, 50, 227.
- [56] N. Jiang, *Rep. Prog. Phys.* **2016**, 79, 016501.
- [57] R. F. Egerton, *Micron* **2019**, 119, 72.
- [58] E. Napcha, *Microsc. Microanal.* **2001**, 9.
- [59] R. F. Egerton, P. Li, M. Malac, *Micron* **2004**, 35, 399.
- [60] H. Inui, H. Mori, T. Sakata, H. Fujita, *J. Non-Cryst. Solids* **1990**, 116, 1.
- [61] M. I. Buckett, J. Strane, D. E. Luzzi, J. P. Zhang, B. W. Wessels, L. D. Marks, *Ultramicroscopy* **1989**, 29, 217.
- [62] J. P. O'Neill, I. M. Ross, A. G. Cullis, T. Wang, P. J. Parbrook, *Appl. Phys. Lett.* **2003**, 83, 1965.
- [63] L. W. Hobbs, in *Fundamental electron and ion beam interactions with solids for microscopy, microanalysis and microlithography*, Vol. 4, (Eds: J. Schou, P. Kruit, D. E. Newbury), Scanning Microscopy International, Chicago, IL **1990**, p. 171.
- [64] M. N. Kabler, R. T. Williams, *Phys. Rev. B* **1978**, 18, 1948.
- [65] L. W. Hobbs, M. R. Pascucci, *J. Phys., Colloq.* **1980**, 41, C6.
- [66] C. P. Flynn, *Point Defects and Diffusion*, Oxford University Press, New York **1972**.
- [67] L. W. Hobbs, *Transmission Electron Microscopy of Extended Defects in Alkali Halide Crystals*, The Royal Society of Chemistry, London **1975**.
- [68] L. R. Parent, E. Bakalis, M. Proetto, Y. Li, C. Park, F. Zerbetto, N. C. Gianneschi, *Acc. Chem. Res.* **2017**, 51, 3.
- [69] R. F. Egerton, I. Rauf, *Ultramicroscopy* **1999**, 80, 247.
- [70] T. W. Chamberlain, J. Biskupek, S. T. Skowron, P. A. Bayliss, E. Bichoutskaia, U. Kaiser, A. N. Khlobystov, *Small* **2015**, 11, 622.
- [71] A. Mardyukov, E. Sanchez-Garcia, P. Rodziewicz, N. L. Doltsinis, W. Sander, *J. Phys. Chem. A* **2007**, 111, 10552.
- [72] M. Pan, P. A. Crozier, *Ultramicroscopy* **1993**, 48, 332.
- [73] B. J. Smith, L. R. Parent, A. C. Overholts, P. A. Beaucage, R. P. Bisbey, A. D. Chavez, N. Hwang, C. Park, A. M. Evans, N. C. Gianneschi, W. R. Dichtel, *ACS Cent. Sci.* **2017**, 3, 58.
- [74] P. Li, R. F. Egerton, *Ultramicroscopy* **2004**, 101, 161.
- [75] N. Jiang, J. C. H. Spence, *Ultramicroscopy* **2012**, 113, 77.
- [76] I. G. Salisbury, R. S. Timsit, S. D. Berger, C. J. Humphreys, *Appl. Phys. Lett.* **1984**, 45, 1289.
- [77] J. M. Macaulay, R. M. Allen, L. M. Brown, S. D. Berger, *Microelectron. Eng.* **1989**, 9, 557.
- [78] C. Bayreder, D. Georg, E. Moser, A. Berg, *Med. Phys.* **2006**, 33, 2506.
- [79] Z. Leijten, A. D. A. Keizer, G. de With, H. Friedrich, *J. Phys. Chem. C* **2017**, 121, 10552.
- [80] K. A. Mkhoyan, J. Silcox, A. Ellison, D. Ast, R. Dieckmann, *Phys. Rev. Lett.* **2006**, 96, 205506.
- [81] L. Jones, A. Varambha, R. Beanland, D. Kepaptsoglou, I. Griffiths, A. Ishizuka, F. Azough, R. Freer, K. Ishizuka, D. Cherns, Q. M. Ramasse, S. Lozano-Perez, P. D. Nellist, *Microscopy* **2018**, 67, i98.

- [82] T. Uchino, T. Sakka, Y. Ogata, M. Iwasaki, *J. Phys. Chem.* **1993**, 97, 9642.
- [83] D. J. Smith, M. R. McCartney, L. A. Bursill, *Ultramicroscopy* **1987**, 23, 299.
- [84] M. R. McCartney, D. J. Smith, *Surf. Sci.* **1989**, 221, 214.
- [85] H. J. Fan, L. D. Marks, *Ultramicroscopy* **1989**, 31, 357.
- [86] N. J. Long, A. K. Petford-Long, *Ultramicroscopy* **1986**, 20, 151.
- [87] K. J. Livi, B. Lafferty, M. Zhu, S. Zhang, A. C. Gaillot, D. L. Sparks, *Environ. Sci. Technol.* **2012**, 46, 970.
- [88] S. R. Singh, L. D. Marks, *Philos. Mag. Lett.* **1989**, 60, 31.
- [89] A. K. Petford, L. D. Marks, M. O'Keeffe, *Surf. Sci.* **1986**, 172, 496.
- [90] D. Wang, D. S. Su, R. Schlögl, *Z. Anorg. Allg. Chem.* **2004**, 630, 1007.
- [91] M. L. Knotek, P. J. Feibelman, *Phys. Rev. Lett.* **1978**, 40, 964.
- [92] Y. Kawahara, S. Naruko, A. Nakayama, M.-C. Wu, E. M. Woo, M. Tsuji, *J. Mater. Sci.* **2009**, 44, 4705.
- [93] R. F. Egerton, *Rep. Prog. Phys.* **2009**, 72, 016502.
- [94] R. Henderson, R. M. Glaeser, *Ultramicroscopy* **1985**, 16, 139.
- [95] L. Reimer, *Ultramicroscopy* **1984**, 14, 291.
- [96] J. E. Evans, D. B. Carlson, in *The Transmission Electron Microscope* (Ed: K. Maaz), IntechOpen, London **2012**, Ch. 5.
- [97] D. Typke, C. J. Gilpin, K. H. Downing, R. M. Glaeser, *Ultramicroscopy* **2007**, 107, 106.
- [98] R. M. Glaeser, G. McMullan, A. R. Faruqi, R. Henderson, *Ultramicroscopy* **2011**, 111, 90.
- [99] C. Guo, F. I. Allen, Y. Lee, T. P. Le, C. Song, J. Ciston, A. M. Minor, E. D. Gomez, *Adv. Funct. Mater.* **2015**, 25, 6071.
- [100] J. Bentley, S. R. Gilliss, C. B. Carter, J. F. Al-Sharab, F. Cosandey, I. M. Anderson, P. J. Kotula, *J. Phys.: Conf. Ser.* **2006**, 26, 69.
- [101] R. A. Carlton, C. E. Lyman, J. E. Roberts, *Scanning* **2004**, 26, 167.
- [102] R. F. Egerton, *Microsc., Microanal., Microstruct.* **1991**, 2, 203.
- [103] G. Bertoni, J. Verbeeck, *Ultramicroscopy* **2008**, 108, 782.
- [104] Y. Otsuka, Y. Shimizu, I. Tanaka, *J. Electron Microsc.* **2009**, 58, 29.
- [105] A. L. Koh, K. Bao, I. Khan, W. E. Smith, G. Kothleitner, P. Nordlander, S. A. Maier, D. W. McComb, *ACS Nano* **2009**, 3, 3015.
- [106] L. A. J. Garvie, P. R. Buseck, *J. Phys. Chem. Solids* **1999**, 60, 1943.
- [107] S. Turner, J. Verbeeck, F. Ramezanipour, J. E. Greedan, G. Van Tendeloo, G. A. Botton, *Chem. Mater.* **2012**, 24, 1904.
- [108] D. A. Muller, Y. Tzou, R. Raj, J. Silcox, *Nature* **1993**, 366, 725.
- [109] A.-L. Hamon, J. Verbeeck, D. Schryvers, J. Benedikt, R. M. C. M. v. d. Sanden, *J. Mater. Chem.* **2004**, 14, 2030.
- [110] D. T. Grubb, G. W. Groves, *Philos. Mag.* **1971**, 24, 815.
- [111] D. T. Grubb, *J. Mater. Sci.* **1974**, 9, 1715.
- [112] S. M. Salih, V. E. Cosslett, *J. Microsc.* **1975**, 105, 269.
- [113] D. L. Dorset, *J. Electron Microsc. Tech.* **1985**, 2, 89.
- [114] D. L. Dorset, F. Zemlin, *Ultramicroscopy* **1985**, 17, 229.
- [115] T. Ohno, *Ultramicroscopy* **1993**, 48, 359.
- [116] R. M. Glaeser, *Methods Enzymol.* **2016**, 579, 19.
- [117] V. H. Orth, E. W. Fischer, *Makromol. Chem.* **1965**, 88, 188.
- [118] M. S. Isaacson, in *Specimen Damage in the Electron Microscope*, Vol. 7, (Ed: M. A. Hayat), Van Nostrand Reinhold Co., New York **1977**.
- [119] H. C. Zhou, S. Kitagawa, *Chem. Soc. Rev.* **2014**, 43, 5415.
- [120] H. Wu, Y. S. Chua, V. Krungleviciute, M. Tyagi, P. Chen, T. Yildirim, W. Zhou, *J. Am. Chem. Soc.* **2013**, 135, 10525.
- [121] E. I. Solomon, S. I. Gorelsky, A. Dey, *J. Comput. Chem.* **2006**, 27, 1415.
- [122] L. Reimer, P. Gentsch, *Ultramicroscopy* **1975**, 1, 1.
- [123] M. Isaacson, D. Johnson, *Ultramicroscopy* **1975**, 1, 33.
- [124] Z. Dang, J. Shamsi, F. Palazon, M. Imran, Q. A. Akkerman, S. Park, G. Bertoni, M. Prato, R. Brescia, L. Manna, *ACS Nano* **2017**, 11, 2124.
- [125] Q. Hu, Z. Li, Z. Tan, H. Song, C. Ge, G. Niu, J. Han, J. Tang, *Adv. Opt. Mater.* **2018**, 6, 1700864.
- [126] I. Diaz, A. Mayoral, *Micron* **2011**, 42, 512.
- [127] A. Mayoral, T. Carey, P. A. Anderson, I. Diaz, *Microporous Mesoporous Mater.* **2013**, 166, 117.
- [128] A. Mayoral, P. A. Anderson, I. Diaz, *Micron* **2015**, 68, 146.
- [129] M. Pan, P. A. Crozier, *Ultramicroscopy* **1993**, 52, 487.
- [130] G. Xu, J. He, E. Andideh, J. Bielefeld, T. Scherban, Presented at *IEEE Int. Interc. Tech. Conf. Cohesive Strength Characterization of Brittle Low-k Films*, Burlingame, CA, USA June **2002**.
- [131] Z. Li, M. C. Johnson, M. Sun, E. T. Ryan, D. J. Earl, W. Maichen, J. I. Martin, S. Li, C. M. Lew, J. Wang, M. W. Deem, M. E. Davis, Y. Yan, *Angew. Chem., Int. Ed.* **2006**, 45, 6329.
- [132] J. Lin, X. F. Shu, J. X. Dong, *Mater. Lett.* **2005**, 59, 1595.
- [133] J. C. Tan, A. K. Cheetham, *Chem. Soc. Rev.* **2011**, 40, 1059.
- [134] J. C. Tan, T. D. Bennett, A. K. Cheetham, *Proc. Natl. Acad. Sci. USA* **2010**, 107, 9938.
- [135] L. Liu, Z. Chen, J. Wang, D. Zhang, Y. Zhu, S. Ling, K. W. Huang, Y. Belmabkhout, K. Adil, Y. Zhang, B. Slater, M. Eddaoudi, Y. Han, *Nat. Chem.* **2019**, 11, 622.
- [136] W. P. Mounfield, C. Han, S. H. Pang, U. Tumuluri, Y. Jiao, S. Bhattacharyya, M. R. Dutzer, S. Nair, Z. Wu, R. P. Lively, D. S. Sholl, K. S. Walton, *J. Phys. Chem. C* **2016**, 120, 27230.
- [137] X. Li, J. Wang, X. Liu, L. Liu, D. Cha, X. Zheng, A. A. Yousef, K. Song, Y. Zhu, D. Zhang, Y. Han, *J. Am. Chem. Soc.* **2019**, 141, 12021.
- [138] Z. Fang, B. Bueken, D. E. De Vos, R. A. Fischer, *Angew. Chem., Int. Ed.* **2015**, 54, 7234.
- [139] Y. Zhu, J. He, C. Shang, X. Miao, J. Huang, Z. Liu, H. Chen, Y. Han, *J. Am. Chem. Soc.* **2014**, 136, 12746.
- [140] J. H. Warner, F. Schaffel, G. Zhong, M. H. Rummeli, B. Buchner, J. Robertson, G. A. Briggs, *ACS Nano* **2009**, 3, 1557.
- [141] E. Roduner, *Chem. Soc. Rev.* **2006**, 35, 583.
- [142] Z. L. Wang, *J. Phys. Chem. B* **2000**, 104, 1153.
- [143] H. Kura, T. Ogawa, *J. Appl. Phys.* **2010**, 107, 074310.
- [144] L. M. Lacroix, R. Arenal, G. Viau, *J. Am. Chem. Soc.* **2014**, 136, 13075.
- [145] S. Xu, P. Li, Y. Lu, *Nano Res.* **2017**, 11, 625.
- [146] S. Vigonski, V. Jansson, S. Vlassov, B. Polyakov, E. Baibuz, S. Oras, A. Aabloo, F. Djurabekova, V. Zadin, *Nanotechnology* **2018**, 29, 015704.
- [147] X. Huang, S. Li, Y. Huang, S. Wu, X. Zhou, S. Li, C. L. Gan, F. Boey, C. A. Mirkin, H. Zhang, *Nat. Commun.* **2011**, 2, 292.
- [148] C. Su, M. Tripathi, Q.-B. Yan, Z. Wang, Z. Zhang, C. Hofer, H. Wang, L. Basile, G. Su, M. Dong, J. C. Meyer, J. Kotakoski, J. Kong, J.-C. Idrobo, T. Susi, J. Li, *Sci. Adv.* **2019**, 5, eaav2252.
- [149] J. Lee, W. Zhou, S. J. Pennycook, J. C. Idrobo, S. T. Pantelides, *Nat. Commun.* **2013**, 4, 1650.
- [150] J. C. Meyer, C. O. Girit, M. F. Crommie, A. Zettl, *Nature* **2008**, 454, 319.
- [151] C. O. Girit, J. C. Meyer, R. Erni, M. D. Rossell, C. Kisielowski, L. Yang, C. H. Park, M. F. Crommie, M. L. Cohen, S. G. Louie, A. Zettl, *Science* **2009**, 323, 1705.
- [152] J. Kotakoski, D. Santos-Cottin, A. V. Krashennnikov, *ACS Nano* **2012**, 6, 671.
- [153] G. A. Rance, D. H. Marsh, R. J. Nicholas, A. N. Khlobystov, *Chem. Phys. Lett.* **2010**, 493, 19.
- [154] R. F. Egerton, *Microsc. Res. Tech.* **2012**, 75, 1550.
- [155] A. Rose, in *Advances in Electronics and Electron Physics*, Vol. 1 (Ed: L. Marton), Academic Press, New York **1948**, p. 131.
- [156] A. E. Burgess, *J. Opt. Soc. Am. A* **1999**, 16, 633.
- [157] H. Yang, P. Ercius, P. D. Nellist, C. Ophus, *Ultramicroscopy* **2016**, 171, 117.
- [158] S. Morishita, M. Mukai, T. Sasaki, K. Suenaga, H. Sawada, *J. Phys.: Conf. Ser.* **2015**, 644, 012033.
- [159] A. Stevens, H. Yang, L. Carin, I. Arslan, N. D. Browning, *Microscopy* **2014**, 63, 41.
- [160] P. A. Crozier, *Ultramicroscopy* **2017**, 180, 104.

- [161] R. Egerton, *Microsc. Microanal.* **2013**, 19, 1212.
- [162] R. F. Egerton, *Ultramicroscopy* **2014**, 145, 85.
- [163] M. Hayashida, T. Kawasaki, Y. Kimura, Y. Takai, *Nucl. Instrum. Methods Phys. Res., Sect. B* **2006**, 248, 273.
- [164] B. Freitag, S. Kujawa, P. M. Mul, J. Ringnalda, P. C. Tiemeijer, *Ultramicroscopy* **2005**, 102, 209.
- [165] D. Van Dyck, H. Lichte, K. D. van der Mast, *Ultramicroscopy* **1996**, 64, 1.
- [166] M. Mukai, S. Morishita, A. Kimura, A. Ikeda, K. Somehara, H. Sawada, L. H. G. Tizei, Y.-C. Lin, K. Kimoto, K. Suenaga, *Microsc. Microanal.* **2015**, 21, 351.
- [167] S. Lazar, P. Tiemeijer, S. Henstra, T. Dennemans, J. Ringnalda, B. Freitag, *Microsc. Microanal.* **2016**, 22, 980.
- [168] S. Morishita, M. Mukai, K. Suenaga, H. Sawada, *Appl. Phys. Lett.* **2016**, 108, 013107.
- [169] S. Lopatin, B. Cheng, W. T. Liu, M. L. Tsai, J. H. He, A. Chuvilin, *Ultramicroscopy* **2018**, 184, 109.
- [170] J. N. C. Ricolleau, T. Oikawa, Y. Kohno, N. Braid, G. Wang, F. Hue, D. Alloyeau, *JEOL News* **2012**, 47, 2.
- [171] K. Kimoto, *Microscopy* **2014**, 63, 337.
- [172] U. Kaiser, J. Biskupek, J. C. Meyer, J. Leschner, L. Lechner, H. Rose, M. Stoger-Pollach, A. N. Khlobystov, P. Hartel, H. Muller, M. Haider, S. Eyhusen, G. Benner, *Ultramicroscopy* **2011**, 111, 1239.
- [173] P. C. Tiemeijer, M. Bischoff, B. Freitag, C. Kisielowski, *Ultramicroscopy* **2012**, 114, 72.
- [174] M. Linck, P. Hartel, S. Uhlemann, F. Kahl, H. Muller, J. Zach, M. Haider, M. Niessadt, M. Bischoff, J. Biskupek, Z. Lee, T. Lehnert, F. Bornert, H. Rose, U. Kaiser, *Phys. Rev. Lett.* **2016**, 117, 076101.
- [175] M. Haider, S. Uhlemann, J. Zach, *Ultramicroscopy* **2000**, 81, 163.
- [176] F. Hosokawa, H. Sawada, Y. Kondo, K. Takayanagi, K. Suenaga, *Microscopy* **2013**, 62, 23.
- [177] C. Ophus, T. Juffmann, S. A. Koppell, B. B. Klopfer, R. Glaeser, M. A. Kasevich, *Microsc. Microanal.* **2017**, 23, 1794.
- [178] C. S. C. Beenakker, *Phys. Today* **2003**, 5, 37.
- [179] V. Giovannetti, S. Lloyd, L. Maccone, *Nat. Photonics* **2011**, 5, 222.
- [180] T. Juffmann, S. A. Koppell, B. B. Klopfer, C. Ophus, R. M. Glaeser, M. A. Kasevich, *Sci. Rep.* **2017**, 7, 1699.
- [181] J. Hajdu, *Curr. Opin. Struct. Biol.* **2000**, 10, 569.
- [182] R. Neutze, R. Wouts, D. van der Spoel, E. Weckert, J. Hajdu, *Nature* **2000**, 406, 752.
- [183] K. J. Gaffney, H. N. Chapman, *Science* **2007**, 316, 1444.
- [184] J. Miao, T. Ishikawa, I. K. Robinson, M. M. Murnane, *Science* **2015**, 348, 530.
- [185] R. F. Egerton, *Adv. Struct. Chem. Imaging* **2015**, 1, 5.
- [186] J. C. Spence, H. N. Chapman, *Philos. Trans. R. Soc., B* **2014**, 369, 20130309.
- [187] C. Kisielowski, *J. Mater. Sci.* **2015**, 51, 635.
- [188] J. Wery, J. L. Mansot, *Microsc. Microanal. Microstruct.* **1993**, 4, 87.
- [189] A. Dashti, P. Schwander, R. Langlois, R. Fung, W. Li, A. Hosseinzadeh, H. Y. Liao, J. Pallesen, G. Sharma, V. A. Stupina, A. E. Simon, J. D. Dinman, J. Frank, A. Ourmazd, *Proc. Natl. Acad. Sci. USA* **2014**, 111, 17492.
- [190] S. Helveg, C. F. Kisielowski, J. R. Jinschek, P. Specht, G. Yuan, H. Frei, *Micron* **2015**, 68, 176.
- [191] C. Kisielowski, L.-W. Wang, P. Specht, H. A. Calderon, B. Barton, B. Jiang, J. H. Kang, R. Cieslinski, *Phys. Rev. B* **2013**, 88, 024305.
- [192] V. A. Lobastov, R. Srinivasan, A. H. Zewail, *Proc. Natl. Acad. Sci. USA* **2005**, 102, 7069.
- [193] D. A. Plemmons, P. K. Suri, D. J. Flannigan, *Chem. Mater.* **2015**, 27, 3178.
- [194] B. Barwick, H. S. Park, O. H. Kwon, J. S. Baskin, A. H. Zewail, *Science* **2008**, 322, 1227.
- [195] D. J. Flannigan, A. H. Zewail, *Nano Lett.* **2010**, 10, 1892.
- [196] O. F. Mohammed, D. S. Yang, S. K. Pal, A. H. Zewail, *J. Am. Chem. Soc.* **2011**, 133, 7708.
- [197] H. S. Park, J. S. Baskin, B. Barwick, O. H. Kwon, A. H. Zewail, *Ultramicroscopy* **2009**, 110, 7.
- [198] G. M. Vanacore, A. W. P. Fitzpatrick, A. H. Zewail, *Nano Today* **2016**, 11, 228.
- [199] E. J. VandenBussche, D. J. Flannigan, *Nano Lett.* **2019**, 19, 6687.
- [200] R. J. Warmack, R. S. Becker, V. E. Anderson, R. H. Ritchie, Y. T. Chu, J. Little, T. L. Ferrell, *Phys. Rev. B* **1984**, 29, 4375.
- [201] P. Rez, T. Aoki, K. March, D. Gur, O. L. Krivanek, N. Dellby, T. C. Lovejoy, S. G. Wolf, H. Cohen, *Nat. Commun.* **2016**, 7, 10945.
- [202] Q. Liu, K. March, P. A. Crozier, *Ultramicroscopy* **2017**, 178, 2.
- [203] A. Stevens, L. Luzi, H. Yang, L. Kovarik, B. L. Mehdi, A. Liyu, M. E. Gehm, N. D. Browning, *Appl. Phys. Lett.* **2018**, 112, 043104.
- [204] N. D. Browning, A. Stevens, L. Kovarik, A. Liyu, B. L. Mehdi, B. Stanfill, S. Reehl, L. Bramer, *Microsc. Microanal.* **2017**, 23, 82.
- [205] L. Donati, M. Nilchian, S. Trepout, C. Messaoudi, S. Marco, M. Unser, *Ultramicroscopy* **2017**, 179, 47.
- [206] S. Ganguli, H. Sompolsky, *Annu. Rev. Neurosci.* **2012**, 35, 485.
- [207] L. Kovarik, A. Stevens, A. Liyu, N. D. Browning, *Appl. Phys. Lett.* **2016**, 109, 164102.
- [208] A. Stevens, L. Kovarik, P. Abellan, X. Yuan, L. Carin, N. D. Browning, *Adv. Struct. Chem. Imaging* **2015**, 1, 10.
- [209] R. Henderson, *Acta Crystallogr.* **2017**, A70, C1024.
- [210] E. Nogales, *Proc. Natl. Acad. Sci. USA* **2018**, 115, 441.
- [211] Y. Wang, *Sci. China Mater.* **2017**, 61, 129.
- [212] Y. Talmon, *J. Microsc.* **1982**, 125, 227.
- [213] C. Wiktor, S. Turner, D. Zacher, R. A. Fischer, G. V. Tendeloo, *Microporous Mesoporous Mater.* **2012**, 162, 131.
- [214] X. Li, P. Mooney, S. Zheng, C. R. Booth, M. B. Braunfeld, S. Gubbens, D. A. Agard, Y. Cheng, *Nat. Methods* **2013**, 10, 584.
- [215] R. F. Egerton, R. McLeod, F. Wang, M. Malac, *Ultramicroscopy* **2010**, 110, 991.
- [216] G. Algara-Siller, S. Kurasch, M. Sedighi, O. Lehtinen, U. Kaiser, *Appl. Phys. Lett.* **2013**, 103, 203107.
- [217] L. A. Bursill, E. A. Lodge, J. M. Thomas, *Nature* **1980**, 286, 111.
- [218] L. A. Bursill, J. M. Thomas, K. J. Rao, *Nature* **1981**, 289, 157.
- [219] N. Nakamura, Y. Shimizu, T. Shinkawa, M. Nakata, B. Bammes, J. Zhang, W. Chiu, *J. Electron Microsc.* **2010**, 59, 299.
- [220] A. A. Sousa, A. A. Azari, G. Zhang, R. D. Leapman, *J. Struct. Biol.* **2011**, 174, 107.
- [221] M. C. Scott, C. C. Chen, M. Mecklenburg, C. Zhu, R. Xu, P. Ercius, U. Dahmen, B. C. Regan, J. Miao, *Nature* **2012**, 483, 444.
- [222] J. M. Thomas, R. Leary, P. A. Midgley, D. J. Holland, *J. Colloid Interface Sci.* **2013**, 392, 7.
- [223] M. D. Guay, W. Czaja, M. A. Aronova, R. D. Leapman, *Sci. Rep.* **2016**, 6, 27614.
- [224] R. Leary, Z. Saghi, P. A. Midgley, D. J. Holland, *Ultramicroscopy* **2013**, 131, 70.
- [225] B. Goris, S. Bals, W. Van den Broek, E. Carbo-Argibay, S. Gomez-Grana, L. M. Liz-Marzan, G. Van Tendeloo, *Nat. Mater.* **2012**, 11, 930.
- [226] B. Goris, W. Van den Broek, K. J. Batenburg, H. Heidari Mezerji, S. Bals, *Ultramicroscopy* **2012**, 113, 120.
- [227] Z. Saghi, G. Divitini, B. Winter, R. Leary, E. Spiecker, C. Ducati, P. A. Midgley, *Ultramicroscopy* **2016**, 160, 230.
- [228] Z. Saghi, D. J. Holland, R. Leary, A. Falqui, G. Bertoni, A. J. Sederman, L. F. Gladden, P. A. Midgley, *Nano Lett.* **2011**, 11, 4666.
- [229] S. Bals, K. J. Batenburg, D. D. Liang, O. Lebedev, G. Van Tendeloo, A. Aerts, J. A. Martens, C. E. A. Kirschhock, *J. Am. Chem. Soc.* **2009**, 131, 4769.
- [230] S. Bals, S. Van Aert, G. Van Tendeloo, *Curr. Opin. Solid State Mater. Sci.* **2013**, 17, 107.

- [231] K. J. Batenburg, S. Bals, J. Sijbers, C. Kubel, P. A. Midgley, J. C. Hernandez, U. Kaiser, E. R. Encina, E. A. Coronado, G. Van Tendeloo, *Ultramicroscopy* **2009**, 109, 730.
- [232] X. Zhuge, H. Jinnai, R. E. Dunin-Borkowski, V. Migunov, S. Bals, P. Cool, A. J. Bons, K. J. Batenburg, *Ultramicroscopy* **2017**, 175, 87.
- [233] S. Van Aert, K. J. Batenburg, M. D. Rossell, R. Erni, G. Van Tendeloo, *Nature* **2011**, 470, 374.
- [234] T. A. M. Bharat, C. J. Russo, J. Lowe, L. A. Passmore, S. H. W. Scheres, *Structure* **2015**, 23, 1743.
- [235] J. L. Milne, S. Subramaniam, *Nat. Rev. Microbiol.* **2009**, 7, 666.
- [236] M. F. Schmid, *Adv. Protein Chem. Struct. Biol.* **2011**, 82, 37.
- [237] A. Bartesaghi, F. Lecumberry, G. Sapiro, S. Subramaniam, *Structure* **2012**, 20, 2003.
- [238] M. Azubel, J. Koivisto, S. Malola, D. Bushnell, G. L. Hura, A. L. Koh, H. Tsunoyama, T. Tsukuda, M. Pettersson, H. Hakkinen, R. D. Kornberg, *Science* **2014**, 345, 909.
- [239] F. R. Chen, D. Van Dyck, C. Kisielowski, *Nat. Commun.* **2016**, 7, 10603.
- [240] C. Kisielowski, C. J. D. Hetherington, Y. C. Wang, R. Kilaas, M. A. O'Keefe, A. Thust, *Ultramicroscopy* **2001**, 89, 243.
- [241] L.-G. Chen, J. Warner, A. I. Kirkland, F.-R. Chen, D. Van Dyck, *Sci. Rep.* **2017**, 7, 10839.
- [242] D. Van Dyck, J. R. Jinschek, F. R. Chen, *Nature* **2012**, 486, 243.
- [243] C. Kisielowski, *Adv. Mater.* **2015**, 27, 5838.
- [244] C. Booth, P. Mooney, *Microsc. Microanal.* **2013**, 27, 13.
- [245] A. R. Faruqi, R. Henderson, *Curr. Opin. Struct. Biol.* **2007**, 17, 549.
- [246] G. McMullan, A. R. Faruqi, R. Henderson, *Methods Enzymol.* **2016**, 579, 1.
- [247] B. E. Bammes, R. H. Rochat, J. Jakana, D. H. Chen, W. Chiu, *J. Struct. Biol.* **2012**, 177, 589.
- [248] X. M. Li, P. Mooney, S. Zheng, C. R. Booth, M. B. Braunfeld, S. Gubbens, D. A. Agard, Y. F. Cheng, *Nat. Methods* **2013**, 10, 584.
- [249] J. N. Chapman, F. Glas, P. T. E. Roberts, Presented at *Inst. Phys. Conf. Ser. Two CCD-based Detector Systems for use in Electron Microscopy and Related Techniques*, Cambridge, UK, September **1981**.
- [250] J. C. H. Spence, J. M. Zuo, *Rev. Sci. Instrum.* **1988**, 59, 2102.
- [251] R. Ramachandra, J. C. Bouwer, M. R. Mackey, E. Bushong, S. T. Peltier, N. H. Xuong, M. H. Ellisman, *Microsc. Microanal.* **2014**, 20, 706.
- [252] A. HajiRassouliha, A. J. Taberner, M. P. Nash, P. M. F. Nielsen, *Comput. Vision Image Understanding* **2018**, 170, 28.
- [253] M. Liao, E. Cao, D. Julius, Y. Cheng, *Nature* **2013**, 504, 107.
- [254] D. M. Haiber, P. A. Crozier, *Microsc. Microanal.* **2017**, 23, 1808.
- [255] E. L. Lawrence, S. L. Y. Chang, P. A. Crozier, *Microsc. Microanal.* **2017**, 23, 1994.
- [256] T. G. Sharp, S. L. Y. Chang, *Microsc. Microanal.* **2017**, 23, 2152.
- [257] N. Shibata, S. D. Findlay, T. Matsumoto, Y. Kohno, T. Seki, G. Sanchez-Santolino, Y. Ikuhara, *Acc. Chem. Res.* **2017**, 50, 1502.
- [258] F. F. Krause, M. Schowalter, T. Grieb, K. Muller-Caspary, T. Mehrtens, A. Rosenauer, *Ultramicroscopy* **2016**, 161, 146.
- [259] P. D. Nellist, S. J. Pennycook, in *Advances in Imaging and Electron Physics*, Vol. 113, (Ed: P. W. Hawkes), Elsevier, Amsterdam **2000**, p. 147.
- [260] E. Oveisi, M. C. Spadaro, E. Rotunno, V. Grillo, C. Hébert, *Ultramicroscopy* **2019**, 200, 139.
- [261] P. Rez, *Microsc. Microanal.* **2001**, 7, 356.
- [262] R. Ishikawa, E. Okunishi, H. Sawada, Y. Kondo, F. Hosokawa, E. Abe, *Nat. Mater.* **2011**, 10, 278.
- [263] Y. Oshima, H. Sawada, F. Hosokawa, E. Okunishi, T. Kaneyama, Y. Kondo, S. Niitaka, H. Takagi, Y. Tanishiro, K. Takayanagi, *J. Electron Microsc.* **2010**, 59, 457.
- [264] S. D. Findlay, T. Saito, N. Shibata, Y. Sato, J. Matsuda, K. Asano, E. Akiba, T. Hirayama, Y. Ikuhara, *Appl. Phys. Express* **2010**, 3, 116603.
- [265] N. Shibata, T. Seki, G. Sanchez-Santolino, S. D. Findlay, Y. Kohno, T. Matsumoto, R. Ishikawa, Y. Ikuhara, *Nat. Commun.* **2017**, 8, 15631.
- [266] N. Shibata, Y. Kohno, S. D. Findlay, H. Sawada, Y. Kondo, Y. Ikuhara, *J. Electron Microsc.* **2010**, 59, 473.
- [267] H. Yang, T. J. Pennycook, P. D. Nellist, *Ultramicroscopy* **2015**, 151, 232.
- [268] E. G. T. Bosch, I. Lazic, S. Lazar, *Microsc. Microanal.* **2016**, 22, 306.
- [269] A. Carlsson, I. Alexandrou, E. Yücelen, E. G. T. Bosch, I. Lazić, *Microsc. Microanal.* **2018**, 24, 122.
- [270] Y. C. Wang, M. Kulzick, A. Carlsson, *Microsc. Microanal.* **2018**, 24, 1996.
- [271] H. Nahor, Y. Kauffmann, S. Lazar, D. Shilo, W. D. Kaplan, *Acta Mater.* **2018**, 154, 71.
- [272] P. Wang, F. Zhang, S. Gao, M. Zhang, A. I. Kirkland, *Sci. Rep.* **2017**, 7, 2857.
- [273] C. Ophus, P. Ercius, M. Huijben, J. Ciston, *Appl. Phys. Lett.* **2017**, 110, 063102.
- [274] K. Muller, F. F. Krause, A. Beche, M. Schowalter, V. Galioit, S. Löffler, J. Verbeeck, J. Zweck, P. Schattschneider, A. Rosenauer, *Nat. Commun.* **2014**, 5, 5653.
- [275] R. dos Reis, C. Ophus, J. Ciston, P. Ercius, U. Dahmen, *Microsc. Microanal.* **2015**, 21, 1097.
- [276] V. B. Ozdol, C. Gammer, X. G. Jin, P. Ercius, C. Ophus, J. Ciston, A. M. Minor, *Appl. Phys. Lett.* **2015**, 106, 253107.
- [277] C. Gammer, J. Kacher, C. Czarnik, O. L. Warren, J. Ciston, A. M. Minor, *Appl. Phys. Lett.* **2016**, 109, 081906.
- [278] T. C. Pekin, C. Gammer, J. Ciston, A. M. Minor, C. Ophus, *Ultramicroscopy* **2017**, 176, 170.
- [279] C. Ophus, P. Ercius, M. Sarahan, C. Czarnik, J. Ciston, *Microsc. Microanal.* **2014**, 20, 62.
- [280] T. Hamaoka, A. Hashimoto, K. Mitsuishi, M. Takeguchi, *e-J. Surf. Sci. Nanotechnol.* **2018**, 16, 247.
- [281] H. Yang, R. N. Rutte, L. Jones, M. Simson, R. Sagawa, H. Ryll, M. Huth, T. J. Pennycook, M. L. Green, H. Soltau, Y. Kondo, B. G. Davis, P. D. Nellist, *Nat. Commun.* **2016**, 7, 12532.
- [282] P. Thibault, M. Dierolf, O. Bunk, A. Menzel, F. Pfeiffer, *Ultramicroscopy* **2009**, 109, 338.
- [283] A. M. Maiden, J. M. Rodenburg, *Ultramicroscopy* **2009**, 109, 1256.
- [284] P. Thibault, M. Dierolf, A. Menzel, O. Bunk, C. David, F. Pfeiffer, *Science* **2008**, 321, 379.
- [285] J. R. Fienup, *Appl. Opt.* **1982**, 21, 2758.
- [286] T. J. Pennycook, A. R. Lupini, H. Yang, M. F. Murfitt, L. Jones, P. D. Nellist, *Ultramicroscopy* **2015**, 151, 160.
- [287] S. Gao, P. Wang, F. Zhang, G. T. Martinez, P. D. Nellist, X. Pan, A. I. Kirkland, *Nat. Commun.* **2017**, 8, 163.
- [288] H. Yang, I. MacLaren, L. Jones, G. T. Martinez, M. Simson, M. Huth, H. Ryll, H. Soltau, R. Sagawa, Y. Kondo, C. Ophus, P. Ercius, L. Jin, A. Kovacs, P. D. Nellist, *Ultramicroscopy* **2017**, 180, 173.
- [289] J. G. Lozano, G. T. Martinez, L. Jin, P. D. Nellist, P. G. Bruce, *Nano Lett.* **2018**, 18, 6850.
- [290] M. W. Tate, P. Purohit, D. Chamberlain, K. X. Nguyen, R. Hovden, C. S. Chang, P. Deb, E. Turgut, J. T. Heron, D. G. Schlom, D. C. Ralph, G. D. Fuchs, K. S. Shanks, H. T. Philipp, D. A. Muller, S. M. Gruner, *Microsc. Microanal.* **2016**, 22, 237.
- [291] H. Yang, L. Jones, H. Ryll, M. Simson, H. Soltau, Y. Kondo, R. Sagawa, H. Banba, I. MacLaren, P. D. Nellist, *J. Phys.: Conf. Ser.* **2015**, 644, 012032.
- [292] J. Song, B. Song, L. Zou, C. Allen, H. Sawada, F. Zhang, X. Pan, A. I. Kirkland, P. Wang, *Microsc. Microanal.* **2018**, 24, 224.
- [293] R. Sagawa, H. Hashiguchi, T. Isabell, R. Ritz, M. Simson, M. Huth, H. Soltau, G. T. Martinez, P. D. Nellist, Y. Kondo, *Microsc. Microanal.* **2018**, 24, 198.
- [294] Y. Jiang, Z. Chen, Y. Han, P. Deb, H. Gao, S. Xie, P. Purohit, M. W. Tate, J. Park, S. M. Gruner, V. Elser, D. A. Muller, *Nature* **2018**, 559, 343.

- [295] C. S. Allen, J. Song, M. Danaie, P. Wang, A. I. Kirkland, *Microsc. Microanal.* **2018**, *24*, 186.
- [296] J. Song, C. S. Allen, S. Gao, C. Huang, H. Sawada, X. Pan, J. Warner, P. Wang, A. I. Kirkland, *Sci. Rep.* **2019**, *9*, 3919.
- [297] B. Song, Z. Ding, C. S. Allen, H. Sawada, F. Zhang, X. Pan, J. Warner, A. I. Kirkland, P. Wang, *Phys. Rev. Lett.* **2018**, *121*, 146101.
- [298] C. Ophus, J. Ciston, J. Pierce, T. R. Harvey, J. Chess, B. J. McMorran, C. Czarnecki, H. H. Rose, P. Ercius, *Nat. Commun.* **2016**, *7*, 10719.
- [299] T. Seki, Y. Ikuhara, N. Shibata, *Ultramicroscopy* **2018**, *193*, 118.
- [300] T. J. Pennycook, G. T. Martinez, P. D. Nellist, J. C. Meyer, *Ultramicroscopy* **2019**, *196*, 131.
- [301] X. F. Yang, A. Wang, B. Qiao, J. Li, J. Liu, T. Zhang, *Acc. Chem. Res.* **2013**, *46*, 1740.
- [302] O. M. Yaghi, M. O'Keeffe, N. W. Ockwig, H. K. Chae, M. Eddaoudi, J. Kim, *Nature* **2003**, *423*, 705.
- [303] A. P. Cote, A. I. Benin, N. W. Ockwig, M. O'Keeffe, A. J. Matzger, O. M. Yaghi, *Science* **2005**, *310*, 1166.
- [304] G. T. Kokotailo, S. L. Lawton, D. H. Olson, W. M. Meier, *Nature* **1978**, *272*, 437.
- [305] K. S. Novoselov, D. Jiang, F. Schedin, T. J. Booth, V. V. Khotkevich, S. V. Morozov, A. K. Geim, *Proc. Natl. Acad. Sci. USA* **2005**, *102*, 10451.
- [306] C. R. Kagan, *Science* **1999**, *286*, 945.
- [307] L. J. Allen, H. Leeb, A. E. Spargo, *Acta Crystallogr. A* **1999**, *55*, 105.
- [308] S. W. Wilkins, J. N. Varghese, M. S. Lehmann, *Acta Crystallogr. A* **1983**, *39*, 594.
- [309] P. N. Nakashima, A. F. Moodie, J. Etheridge, *Acta Crystallogr. A* **2007**, *63*, 387.
- [310] M. A. Estermann, L. B. McCusker, C. Baerlocher, *J. Appl. Crystallogr.* **1992**, *25*, 539.
- [311] P. A. Buffat, *Philos. Trans. R. Soc., A* **2003**, *361*, 291.
- [312] R. Uyeda, *Acta Crystallogr., Sect. A: Cryst. Phys., Diffraction, Theor. Gen. Crystallogr.* **1968**, *24*, 175.
- [313] J. Hadermann, *J. Appl. Crystallogr.* **2014**, *47*, 816.
- [314] J. P. Zhang, Y. Y. Wang, R. Ai, C. E. Platt, Y. Zhang, D. L. Shi, D. C. Hinks, L. D. Marks, *Phys. C* **1994**, *219*, 191.
- [315] S. Y. Ding, J. Gao, Q. Wang, Y. Zhang, W. G. Song, C. Y. Su, W. Wang, *J. Am. Chem. Soc.* **2011**, *133*, 19816.
- [316] L. L. Li, X. Q. Feng, R. P. Han, S. Q. Zang, G. Yang, *J. Hazard. Mater.* **2017**, *321*, 622.
- [317] K. Na, K. M. Choi, O. M. Yaghi, G. A. Somorjai, *Nano Lett.* **2014**, *14*, 5979.
- [318] H. Furukawa, K. E. Cordova, M. O'Keeffe, O. M. Yaghi, *Science* **2013**, *341*, 1230444.
- [319] M. Moliner, T. Willhammar, W. Wan, J. Gonzalez, F. Rey, J. L. Jorda, X. Zou, A. Corma, *J. Am. Chem. Soc.* **2012**, *134*, 6473.
- [320] T. Willhammar, A. W. Burton, Y. Yun, J. Sun, M. Afeworki, K. G. Strohmaier, H. Vroman, X. Zou, *J. Am. Chem. Soc.* **2014**, *136*, 13570.
- [321] D. Xu, Y. Ma, Z. Jing, L. Han, B. Singh, J. Feng, X. Shen, F. Cao, P. Oleynikov, H. Sun, O. Terasaki, S. Che, *Nat. Commun.* **2014**, *5*, 4262.
- [322] J. Ruan, P. Wu, B. Slater, Z. Zhao, L. Wu, O. Terasaki, *Chem. Mater.* **2009**, *21*, 2904.
- [323] J. P. Buban, Q. Ramasse, B. Gipson, N. D. Browning, H. Stahlberg, *J. Electron Microsc.* **2010**, *59*, 103.
- [324] A. Mayoral, J. Coronas, C. Casado, C. Tellez, I. Díaz, *ChemCatChem* **2013**, *5*, 2595.
- [325] N. Kosinov, F. J. A. G. Coumans, E. A. Uslamin, A. S. G. Wijkema, B. Mezari, E. J. M. Hensen, *ACS Catal.* **2016**, *7*, 520.
- [326] J. Gao, Y. Zheng, J. M. Jehng, Y. Tang, I. E. Wachs, S. G. Podkolzin, *Science* **2015**, *348*, 686.
- [327] B. Shen, X. Chen, D. Cai, H. Xiong, X. Liu, C. Meng, Y. Han, F. Wei, *Adv. Mater.* **2019**, *32*, 1906103.
- [328] L. Liu, N. Wang, C. Zhu, X. Liu, Y. Zhu, P. Guo, L. Alfili, X. Dong, D. Zhang, Y. Han, *Angew. Chem., Int. Ed.* **2020**, *132*, 829.
- [329] F. Gandara, T. D. Bennett, *IUCrJ* **2014**, *1*, 563.
- [330] A. Gupta, T. Sakthivel, S. Seal, *Prog. Mater. Sci.* **2015**, *73*, 44.
- [331] P. Avouris, *Nano Lett.* **2010**, *10*, 4285.
- [332] J. Zhu, E. Ha, G. Zhao, Y. Zhou, D. Huang, G. Yue, L. Hu, N. Sun, Y. Wang, L. Y. S. Lee, C. Xu, K.-Y. Wong, D. Astruc, P. Zhao, *Coord. Chem. Rev.* **2017**, *352*, 306.
- [333] H. Wang, H. Yuan, S. Sae Hong, Y. Li, Y. Cui, *Chem. Soc. Rev.* **2015**, *44*, 2664.
- [334] S. Kurasch, J. Kotakoski, O. Lehtinen, V. Skákalová, J. Smet, C. E. Krill, A. V. Krashennnikov, U. Kaiser, *Nano Lett.* **2012**, *12*, 3168.
- [335] Y. C. Lin, P. Y. Teng, C. H. Yeh, M. Koshino, P. W. Chiu, K. Suenaga, *Nano Lett.* **2015**, *15*, 7408.
- [336] Z. Fan, L. Zhang, D. Baumann, L. Mei, Y. Yao, X. Duan, Y. Shi, J. Huang, Y. Huang, X. Duan, *Adv. Mater.* **2019**, *31*, 1900608.
- [337] C.-M. Wang, *J. Mater. Res.* **2014**, *30*, 326.
- [338] S. Hwang, D. Su, in *Encyclopedia of Inorganic and Bioinorganic Chemistry*, (Ed: R. A. Scott), John Wiley & Sons, Ltd., USA **2020**.
- [339] C. Zhang, Y. Feng, Z. Han, S. Gao, M. Wang, P. Wang, *Adv. Mater.* **2019**, 1903747.
- [340] H. Conrad, G. Ertl, E. E. Latta, *Surf. Sci.* **1974**, *41*, 435.
- [341] M. Bowker, *ACS Nano* **2007**, *1*, 253.
- [342] Z. Y. Zhou, N. Tian, J. T. Li, I. Broadwell, S. G. Sun, *Chem. Soc. Rev.* **2011**, *40*, 4167.
- [343] L. Zhang, W. Niu, G. Xu, *Nano Today* **2012**, *7*, 586.
- [344] Y. Niimi, T. Matsui, H. Kambara, K. Tagami, M. Tsukada, H. Fukuyama, *Phys. Rev. B* **2006**, *73*.
- [345] G. L. Hornyak, S. Peschel, T. Sawitowski, G. Schmid, *Micron* **1998**, *29*, 183.
- [346] B. Li, Z. Zhang, Y. Li, K. Yao, Y. Zhu, Z. Deng, F. Yang, X. Zhou, G. Li, H. Wu, N. Nijem, Y. J. Chabal, Z. Lai, Y. Han, Z. Shi, S. Feng, J. Li, *Angew. Chem., Int. Ed.* **2012**, *51*, 1412.
- [347] Y. W. Son, M. L. Cohen, S. G. Louie, *Nature* **2006**, *444*, 347.
- [348] I. Y. Jeon, H. J. Choi, M. Choi, J. M. Seo, S. M. Jung, M. J. Kim, S. Zhang, L. Zhang, Z. Xia, L. Dai, N. Park, J. B. Baek, *Sci. Rep.* **2013**, *3*, 1810.
- [349] M. Hassan, E. Haque, K. R. Reddy, A. I. Minett, J. Chen, V. G. Gomes, *Nanoscale* **2014**, *6*, 11988.
- [350] S. E. Stein, R. L. Brown, *J. Am. Chem. Soc.* **1987**, *109*, 3721.
- [351] K. Nakada, M. Fujita, G. Dresselhaus, M. S. Dresselhaus, *Phys. Rev. B: Condens. Matter Mater. Phys.* **1996**, *54*, 17954.
- [352] T. Enoki, K. Takai, *Solid State Commun.* **2009**, *149*, 1144.
- [353] Z. Liu, K. Suenaga, P. J. Harris, S. Iijima, *Phys. Rev. Lett.* **2009**, *102*, 015501.
- [354] K. He, A. W. Robertson, Y. Fan, C. S. Allen, Y. C. Lin, K. Suenaga, A. I. Kirkland, J. H. Warner, *ACS Nano* **2015**, *9*, 4786.
- [355] K. He, G.-D. Lee, A. W. Robertson, E. Yoon, J. H. Warner, *Nat. Commun.* **2014**, *5*, 3040.
- [356] C. G. Duan, R. F. Sabirianov, W. N. Mei, S. S. Jaswal, E. Y. Tsymlal, *Nano Lett.* **2006**, *6*, 483.
- [357] G. Chen, Y. Zhao, G. Fu, P. N. Duchesne, L. Gu, Y. Zheng, X. Weng, M. Chen, P. Zhang, C. W. Pao, J. F. Lee, N. Zheng, *Science* **2014**, *344*, 495.
- [358] C. W. Bark, D. A. Felker, Y. Wang, Y. Zhang, H. W. Jang, C. M. Folkman, J. W. Park, S. H. Baek, H. Zhou, D. D. Fong, X. Q. Pan, E. Y. Tsymlal, M. S. Rzechowski, C. B. Eom, *Proc. Natl. Acad. Sci. USA* **2011**, *108*, 4720.
- [359] L. Abad, V. Laukhin, S. Valencia, A. Gaup, W. Gudat, L. Balcells, B. Martínez, *Adv. Funct. Mater.* **2007**, *17*, 3918.
- [360] S. J. Tauster, S. C. Fung, R. T. Baker, J. A. Horsley, *Science* **1981**, *211*, 1121.
- [361] J. C. Matsubu, S. Zhang, L. DeRita, N. S. Marinkovic, J. G. Chen, G. W. Graham, X. Pan, P. Christopher, *Nat. Chem.* **2017**, *9*, 120.

- [362] J. S. Cho, Y. C. Kang, *Small* **2015**, *11*, 4673.
- [363] N. Yanai, M. Sindoro, J. Yan, S. Granick, *J. Am. Chem. Soc.* **2012**, *135*, 34.
- [364] C. Avci, Y. Liu, J. A. Pariente, A. Blanco, C. Lopez, I. Imaz, D. Maspoch, *Small* **2019**, *15*, 1902520.
- [365] M. S. Denny Jr., J. C. Moreton, L. Benz, S. M. Cohen, *Nat. Rev. Mater.* **2016**, *1*, 16078.
- [366] P. Kim, *Nat. Mater.* **2010**, *9*, 792.
- [367] A. W. Tsen, L. Brown, M. P. Levendorf, F. Ghahari, P. Y. Huang, R. W. Havener, C. S. Ruiz-Vargas, D. A. Muller, P. Kim, J. Park, *Science* **2012**, *336*, 1143.
- [368] O. V. Yazyev, S. G. Louie, *Nat. Mater.* **2010**, *9*, 806.
- [369] P. Y. Huang, C. S. Ruiz-Vargas, A. M. van der Zande, W. S. Whitney, M. P. Levendorf, J. W. Kevek, S. Garg, J. S. Alden, C. J. Hustedt, Y. Zhu, J. Park, P. L. McEuen, D. A. Muller, *Nature* **2011**, *469*, 389.
- [370] Y. F. Xu, M. Z. Yang, B. X. Chen, X. D. Wang, H. Y. Chen, D. B. Kuang, C. Y. Su, *J. Am. Chem. Soc.* **2017**, *139*, 5660.
- [371] Y. Lee, J. Kwon, E. Hwang, C. H. Ra, W. J. Yoo, J. H. Ahn, J. H. Park, J. H. Cho, *Adv. Mater.* **2015**, *27*, 41.
- [372] J. Chen, J.-Y. Seo, N.-G. Park, *Adv. Energy Mater.* **2018**, *8*, 1702714.
- [373] L. N. Quan, R. Quintero-Bermudez, O. Voznyy, G. Walters, A. Jain, J. Z. Fan, X. Zheng, Z. Yang, E. H. Sargent, *Adv. Mater.* **2017**, *29*, 1605945.
- [374] P. Cottingham, R. L. Brutchey, *Chem. Mater.* **2016**, *28*, 7574.
- [375] Y. Yu, D. Zhang, P. Yang, *Nano Lett.* **2017**, *17*, 5489.
- [376] J. B. Goodenough, K. S. Park, *J. Am. Chem. Soc.* **2013**, *135*, 1167.
- [377] M. Gauthier, T. J. Carney, A. Grimaud, L. Giordano, N. Pour, H. H. Chang, D. P. Fenning, S. F. Lux, O. Paschos, C. Bauer, F. Maglia, S. Lupart, P. Lamp, Y. Shao-Horn, *J. Phys. Chem. Lett.* **2015**, *6*, 4653.
- [378] E. Quartarone, P. Mustarelli, *Chem. Soc. Rev.* **2011**, *40*, 2525.
- [379] J. Wang, W. Huang, A. Pei, Y. Li, F. Shi, X. Yu, Y. Cui, *Nat. Energy* **2019**, *4*, 664.
- [380] S. Sharma, S. K. Ghoshal, *Renewable Sustainable Energy Rev.* **2015**, *43*, 1151.
- [381] J. A. Turner, *Science* **2004**, *305*, 972.
- [382] S. Orimo, Y. Nakamori, J. R. Eliseo, A. Zuttel, C. M. Jensen, *Chem. Rev.* **2007**, *107*, 4111.
- [383] S. K. Konda, A. Chen, *Mater. Today* **2016**, *19*, 100.
- [384] Y. S. Chen, D. Haley, S. S. A. Gerstl, A. J. London, F. Sweeney, R. A. Wepf, W. M. Rainforth, P. A. J. Bagot, M. P. Moody, *Science* **2017**, *355*, 1196.
- [385] J. M. Sytze de Graaf, C. Mitterbauer, S. Lazar, B. J. Kooi, arXiv:1812.09118, **2018**.
- [386] F. Banhart, J. Kotakoski, A. V. Krashennnikov, *ACS Nano* **2011**, *5*, 26.
- [387] G. Cheng, T. H. Chang, Q. Qin, H. Huang, Y. Zhu, *Nano Lett.* **2014**, *14*, 754.
- [388] S. Dutta, S. Chattopadhyay, A. Sarkar, M. Chakrabarti, D. Sanyal, D. Jana, *Prog. Mater. Sci.* **2009**, *54*, 89.
- [389] B. Panigrahy, M. Aslam, D. S. Misra, M. Ghosh, D. Bahadur, *Adv. Funct. Mater.* **2010**, *20*, 1161.
- [390] O. Kozachuk, I. Luz, F. X. Llabres i Xamena, H. Noei, M. Kauer, H. B. Albada, E. D. Bloch, B. Marler, Y. Wang, M. Muhler, R. A. Fischer, *Angew. Chem., Int. Ed.* **2014**, *53*, 7058.
- [391] N. J. Lawrence, J. R. Brewer, L. Wang, T. S. Wu, J. Wells-Kingsbury, M. M. Ihrig, G. Wang, Y. L. Soo, W. N. Mei, C. L. Cheung, *Nano Lett.* **2011**, *11*, 2666.
- [392] S. Gadipelli, Z. X. Guo, *Prog. Mater. Sci.* **2015**, *69*, 1.
- [393] Y. Yu, F. Cui, J. Sun, P. Yang, *Nano Lett.* **2016**, *16*, 3078.
- [394] J. A. Vargas, V. Petkov, E. S. A. Nouh, R. K. Ramamoorthy, L. M. Lacroix, R. Poteau, G. Viau, P. Lecante, R. Arenal, *ACS Nano* **2018**, *12*, 9521.
- [395] P. Ghosh, Y. J. Colon, R. Q. Snurr, *Chem. Commun.* **2014**, *50*, 11329.
- [396] M. J. Cliffe, W. Wan, X. Zou, P. A. Chater, A. K. Kleppe, M. G. Tucker, H. Wilhelm, N. P. Funnell, F. X. Coudert, A. L. Goodwin, *Nat. Commun.* **2014**, *5*, 4176.
- [397] S. Jakobsen, D. Gianolio, D. S. Wragg, M. H. Nilsen, H. Emerich, S. Bordiga, C. Lamberti, U. Olsbye, M. Tilset, K. P. Lillerud, *Phys. Rev. B* **2012**, *86*, 125429.
- [398] R. Ishikawa, S. D. Findlay, T. Seki, G. Sanchez-Santolino, Y. Kohn, Y. Ikuhara, N. Shibata, *Nat. Commun.* **2018**, *9*, 3878.
- [399] R. Bali, S. Wintz, F. Meutzner, R. Hubner, R. Boucher, A. A. Unal, S. Valencia, A. Neudert, K. Potzger, J. Bauch, F. Kronast, S. Facsko, J. Lindner, J. Fassbender, *Nano Lett.* **2014**, *14*, 435.
- [400] N. Balke, I. Bdikin, S. V. Kalinin, A. L. Kholkin, *J. Am. Ceram. Soc.* **2009**, *92*, 1629.
- [401] F. Li, S. Zhang, Z. Xu, L.-Q. Chen, *Adv. Funct. Mater.* **2017**, *27*, 1700310.